Probing the Origins of Variable Gamma-Ray Emission in Relativistic Astrophysical Jets

Ph.D. Thesis

By

Sushmita Agarwal

Department of Astronomy, Astrophysics and Space Engineering

Indian Institute of Technology Indore
Simrol, Indore, Madhya Pradesh - 453552, India

Probing the Origins of Variable Gamma-Ray Emission in Relativistic Astrophysical Jets

A THESIS

Submitted in partial fulfillment of the requirements for the award of the degree

of

DOCTOR OF PHILOSOPHY

by

Sushmita Agarwal

Department of Astronomy, Astrophysics and Space Engineering

Indian Institute of Technology Indore
Simrol, Indore, Madhya Pradesh - 453552, India

INDIAN INSTITUTE OF TECHNOLOGY INDORE

I hereby certify that the work which is being presented in the thesis entitled "*Probing the Origins of Variable Gamma-Ray Emission in Relativistic Astrophysical Jets*" in the partial fulfillment of the requirements for the award of the degree of **DOCTOR OF PHILOSOPHY** and submitted in the **DEPARTMENT OF Astronomy, Astrophysics and Space Engineering, Indian Institute of Technology Indore**, is an authentic record of my own work carried out during the time period from Jan 2020 to Jan 2025 under the supervision of Dr. Amit Shukla, Associate professor, at IIT Indore.

The matter presented in this thesis has not been submitted by me for the award of any other degree of this or any other institute.

6/05/2025

signature of the student with date
(NAME OF THE PhD STUDENT)

This is to certify that the above statement made by the candidate is correct to the best of my/our knowledge.

5.5.25

Signature of Thesis Supervisor with date
(NAME OF THESIS SUPERVISOR)

Ms. Sushmita Agarwal has successfully given his/her Ph.D. Oral Examination held on **5/05/2025**.

5.5.25

Signature of Thesis Supervisor with date
(NAME OF THESIS SUPERVISOR)

Dedicated

to

my personal cheerleaders

"Somewhere, something incredible is waiting to be known"

- *Sharon Begley* in an interview article with Carl Sagan

Acknowledgements

I would like to begin by expressing my deepest gratitude to my parents, whose unwavering belief in me has been my greatest strength. From a very young age, they encouraged me to stay curious, ask questions, and embrace learning with an open heart. Their constant support has laid the foundation for everything I have achieved. I also would like to express my gratitude to God for giving me resilience to keep moving forwards, and the spirit to stay curious through it all. I also want to thank my siblings, who made life a little easier with their humor, constant encouragement, and understanding—especially during the times I couldn't be in touch for days. Their presence has been a quiet source of strength.

My heartfelt thanks go to my supervisor, Dr. Amit Shukla, for creating a thoughtful and engaging research environment throughout my PhD journey. His mentorship, guidance, and openness to discussions have been invaluable. I am sincerely grateful for the many ways he supported and encouraged me, both academically and personally.

I am truly thankful to my collaborators—Prof. Karl Mannheim, whose insightful comments and discussions greatly enriched our work, and Dr. Bhargav Vaidya, my PSPC member and collaborator, for his steady support and thoughtful guidance throughout my PhD. I also extend my thanks to my PSPC members, Dr. Abhirup Dutta and Dr. Ankhi Roy, for their helpful suggestions and critical feedback that helped shape the direction of this research.

I am sincerely grateful to Dr. Biswajit Banerjee for his enthusiasm, thoughtful discussions, and for always being available for meetings and guidance throughout my

PhD. I am equally thankful to him and Prof. Marica Branchesi for making my research visit to the Gran Sasso Science Institute not only possible but also deeply enriching and comfortable. Their hospitality and support made a lasting impression on me.

Over the years, I have come to truly value the presence of friends outside the research sphere. The otherwise isolating experience of the COVID lockdown in the hostel was brightened by my roommates, Saumya and Rashmi, whose refreshing perspectives and conversations brought joy and laughter to our days. Charu—thank you for trusting me and for being the kind of friend with whom I could talk for hours without a second thought about looming deadlines. Your understanding, insight, and ability to truly see me have helped me grow in many ways. I'm also thankful to friends like Shilpi, who have been a steady moral support throughout this journey.

My time at IIT Indore began during the pandemic, and I was fortunate to find warmth and positivity in the company of Swarna, whose presence always brought light to any conversation. I am grateful to Gourab for adding humor and resilience to the PhD experience and for being a shoulder to lean on when things got overwhelming. Prateek, the 2 AM conversationalist in the lab—thank you for the much-needed late-night diversions. Anshuman, thank you for being a consistent and reliable presence in the department, even through our many friendly debates.

A special thanks goes to Indu, whose guidance as a senior and encouragement as a friend nudged me toward a healthier and more balanced lifestyle. I'm grateful to my collaborator and friend Sriya, for making early discussions on AGN jets approachable and enjoyable. My heartfelt thanks to my seniors—Unnati, for your generous help with proposal writing even at odd hours; Parul, for bringing light-heartedness into serious days; and Akriti, for being a friendly presence throughout. I also thank Sarvesh for his companionship in many thought-provoking (and sometimes controversial) discussions, and for being a solid moral support.

This journey would be incomplete without the constant support of my ever-encouraging labmates – who over time became trusted friends. Shraddha, thank you for being like a sister to me, always present with quiet strength and unwavering support. To Chandan, for being ever-helpful with scientific discussions and technical support whenever needed. I have deeply appreciated the collaborative spirit that grew within our lab - fueled by our shared discussions, evolving perspectives, and the sense of community we built together.

A heartfelt thanks to Pranjali, for being a truly honest and loyal friend through every phase of this journey. Hari, thank you for being a steady and encouraging presence. Pawan, I'm grateful for your warmth, support, and wonderful hospitality during my time at GSSI. Shruti, thank you for being someone I could always count on. I also extend my thanks to labmates Ayush, Aman, and Daisy, whose contributions to our discussions made learning more enriching and engaging.

To my dear friend and tireless cheerleader, Alvera—thank you for the many hours of encouragement, care, and laughter that made even the most stressful deadlines easier to bear. Lekhraj, thank you again for being ever-ready to help in countless ways. And to Sirsho, thank you for the stimulating conversations that often sparked new interests and ideas—your curiosity and energy were always contagious.

Some support comes quietly, without fanfare, but its presence is no less meaningful. It is deeply comforting to know such people exist in the background—offering strength without asking for recognition. I would like to thank Arghyadeep, Nikita, Harshita, Jithu, Aditya, GK, Majid, Aishrilla, Deepthi, Hemapriya, Harsha, Samit, Bhuvanesh, Anoop, Saumya, Rashmi, and Biki for being part of this silent yet strong backbone. Your presence has mattered more than words can express.

As I bring this chapter to a close, I carry with me not just the knowledge gained, but the relationships, moments, and quiet acts of kindness that shaped this journey. Every word of encouragement, every thoughtful conversation, and every silent support has left an imprint on this thesis and on me. To everyone who walked beside me—whether for a short while or all the way through—thank you for being part of this story. This accomplishment is as much yours as it is mine.

Abstract

Active galactic nuclei (AGNs) are luminous objects at the centers of galaxies powered by material accreting onto supermassive black holes (10^6–10^8 $M_\odot$). Unlike normal galaxies dominated by stellar emission, AGNs emit across the electromagnetic spectrum, from radio to tera-electronvolt (TeV). energies. A fraction of AGNs host powerful relativistic jets, whose orientation determines their classification in the unified AGN scheme. Blazars, a sub-class of AGNs with jets aligned closely to the observer's line of sight, exhibit relativistically boosted emission, resulting in enhanced flux, intensity, and shortened variability timescales. This alignment makes blazars ideal probes for studying high-energy gamma-ray emission, particle acceleration, and processes near supermassive black holes.

Blazars exhibit extreme variability, particularly in the high-energy gamma-ray band, where rapid changes in emission provide crucial insights into the size and nature of the emission region. Observed fast variability, often shorter than light-crossing timescales, suggests an extremely compact emission origin—smaller than the central black hole—or the presence of an exceptionally large Doppler factor. These observations, combined with observed GeV to TeV detections, impose stringent constraints on particle acceleration models and highlight a significant gap in understanding the dominant energy dissipation sites in blazar jets.

This thesis aims to localize the site of gamma-ray dissipation in blazars relative to the central engine by analyzing temporal and spectral variability across diverse flux states. Leveraging over a decade of Fermi-LAT data, complemented by Swift observations across optical, ultraviolet, and X-ray bands, the study employs broadband monitoring to investigate the variability in relativistic jets during both flaring and quiescent epochs. By examining the spectral evolution during flaring events and exploring the influence of the local jet environment, this research addresses the ori-

gin of flaring emissions and the role of the external environment, offering valuable insights into particle acceleration processes and identifying prominent gamma-ray emission sites.

This thesis focuses on advancing our understanding of γ-ray production in blazar jets by analyzing three key aspects: spectral evolution during flares, absorption features in γ-ray spectra, and variability studies in gravitationally lensed blazars.

The spectral evolution of the archetypical blazar BL Lacertae during an extended strong flaring episode (2020–2021) provided a rare opportunity to probe particle acceleration models. Observations revealed rapid sub-hour variability and a synchrotron hump extending into the X-ray regime, with associated γ-ray spectral shifts. These findings challenge standard shock acceleration models, requiring unrealistically high Doppler factors (>100). Alternatively, jet-in-jet models, involving magnetic reconnection and plasmoids, offer a plausible explanation for the rapid variability and spectral shifts, suggesting a reconnection region near the edge of the broad-line region with a magnetic field of ~ 0.6 G.

To further investigate the gamma-ray production site, we studied the spectral imprints of the local jet environment on the high-energy gamma-ray spectrum, using it as a probe to enhance our understanding. In this context, we identified an intrinsic absorption feature in the γ-ray spectrum at energies >10 GeV during high-flux states in the flat-spectrum radio quasar PKS 1424−418. This feature, attributed to photon–photon pair production with low-ionization BLR photons, provides crucial constraints on the γ-ray dissipation zone, placing it at the outer edge of the BLR (∼0.02 pc). The absence of this feature in low-flux states indicates a transition of the γ-ray emission zone to regions outside the BLR during fainter states, consistent with moving very long baseline interferometry (VLBI) radio knots. These findings align with variability timescales and highlight the role of external Compton scattering with BLR photons during powerful dissipation events.

While temporal variability is commonly used to identify the emission site, its application to high-redshift blazars is challenging due to the limited sensitivity of current telescopes. Gravitationally lensed blazars offer unique insights into the spatial and temporal characteristics of γ-ray production zones in high-redshift sources. Using 15 years of Fermi-LAT data for PKS 1830-211, this work investigated the origin of flaring γ-ray emissions across varying flux states. Time delays between lensed signals, analyzed using machine learning and traditional methods, revealed consistent delays ($\sim$20 days) for flaring epochs, shorter than previously estimated radio delays. This suggests that γ-ray emission originates closer to the central engine, contrasting with the more distant radio emission zones. The observed linear relationship between lag and magnification further supports the localization of the γ-ray emission zone within the radio core.

By combining spectral, temporal, and spatial analyses, this thesis provides a unified framework for understanding γ-ray production in blazar jets. The findings bridge gaps in particle acceleration models, γ-ray emission zone localization, and variability mechanisms, offering valuable insights into the physics of relativistic jets and their interplay with the AGN environment.

List of Publications

1. *Flaring activity from magnetic reconnection in BL Lacertae*, **Sushmita Agarwal**, Biswajit Banerjee, Amit Shukla, Jayashree Roy, Sriyasriti Acharya, Bhargav Vaidya, Varsha R Chitnis, Sarah M Wagner, Karl Mannheim, Marica Branchesi, 2023, Monthly Notices of the Royal Astronomical Society: Letters, 521, 1, Pages L53–L58, DOI: 10.1093/mnrasl/slad023

2. *Imprint of "Local Opacity" Effect in Gamma-Ray Spectrum of Blazar Jet*, **Sushmita Agarwal**, Amit Shukla, Karl Mannheim, Bhargav Vaidya, Biswajit Banerjee, 2024, ApJL, 968, L1, DOI: 10.3847/2041-8213/ad4994

3. *Constraining $\gamma-$ray dissipation site in gravitationally lensed quasar $-$ PKS 1830$-$211*, **Sushmita Agarwal**, Amit Shukla, Pranjali Sharma, Monthly Notices of the Royal Astronomical Society, Volume 537, Issue 1, February 2025, Pages 332–342, DOI: 10.1093/mnras/staf021

N.B: All the above entries are parts of my thesis.

Table of Contents

List of Figures

List of Tables

Chapter 1

Introduction to γ-ray astronomy

Gamma-rays are produced in the most extreme environments of the universe and are excellent probes to tracing origin of high energy particles of astrophysical origin, such as supernovae, neutron stars, black holes, and relativistic jets. Although particle accelerators on Earth, such as those at Stanford Linear Accelerator Center (SLAC), Fermilab, and the Large Hadron Collider (LHC), can probe the origin of high energy particles in laboratories, the energies achieved by these state-of-the-art facilities are significantly lower than those observed in natural astrophysical accelerators.

The detection of gamma-rays was theorized long before their actual detection by Philip Morrison [Morrison, 1957, 1958] linking their identification to a number of different processes in universe. Detection of gamma-rays became feasible in the 1960s with the advent of balloons and spacecraft, as Earth's atmosphere absorbs most gamma-rays. Later, first detection of gamma-ray in orbit, on the Explorer 11 satellite in early 1960s [Kraushaar & Clark, 1962]. Consequently, another gamma-ray space borne satellite OSO 3 was launched in 1967 identifying significant gamma ray emission from galactic center [Kraushaar et al., 1972]. Major advances in the field of gamma-ray astronomy is made by SAS-2 (1972) [Fichtel et al., 1975] and Cos-B (1975–1982) [Bignami et al., 1975], which mapped the gamma-ray sky and identified point sources.

NASA's Compton Gamma Ray Observatory (CGRO), launched in 1991, marked a major advancement in gamma-ray astronomy with its advanced instruments, particularly the onboard instrument Energetic Gamma Ray Experiment Telescope (EGRET) [Hartman et al., 1996]. EGRET was highly sensitive to photons up to 30 GeV, significantly improving spatial and temporal resolution compared to its predecessors [Casandjian & Grenier, 2008; Hartman et al., 1992, 1996, 1999].

In the past decade, the understanding of the high-energy universe has been further revolutionized by highly sensitive space-based observatories such as NASA's Fermi Gamma-ray Space Telescope, launched in 2008. Fermi is capable of detecting photons in the energy range of 30 MeV to 300 GeV, providing unprecedented insights into gamma-ray sources. Ground-based Cherenkov telescopes, such as HESS, MAGIC, and VERITAS, have complemented these observations, extending coverage to even higher energy ranges and enhancing the study of extreme astrophysical phenomena. The wealth of data from these instruments and the improved identification of gamma-ray sources have advanced fundamental questions, including the origins of cosmic rays, the nature of dark matter, and tests of Einstein's special theory of relativity. Additionally, these developments have enabled the exploration of extreme environments, such as the regions near black holes, shedding light on the mechanisms governing the most energetic processes in the universe.

1.1 Cosmic rays

Cosmic rays were first identified as a highly penetrating radiation of extraterrestrial origin in 1912, when Victor Hess measured atmospheric ionization during a balloon ascent to 5300 meters [Hess, 2018]. His observations revealed that ionization rates increased significantly with altitude, establishing the cosmic origin of these high-energy particles [Millikan, 1925]. Composed primarily of protons (∼90%), with the remainder consisting of helium nuclei and heavier elements, cosmic rays span an energy spectrum from GeV to at least 10^{20} eV. The cosmic ray spectrum follows a steep power-law distribution, $dN/dE \sim E^{-s}$, spanning a vast energy range and punctuated by distinct features linked to acceleration mechanisms, propagation effects, and cosmic origins. Some of the key features of cosmic ray spectrum as identified in Figure 1.1 are as below:

1. **Low-Energy Cosmic Rays**: Energies below a few GeV are strongly influenced by solar modulation, which affects their intensity and spectra due to interactions with the solar wind and magnetic fields.

2. **Galactic Cosmic Rays (GCRs)**: Dominant at intermediate energies (up to 10^{15} eV), these cosmic rays originate from sources within the Milky Way, through diffusive shock acceleration in the strong shock fronts of supernova remnants [Blasi, 2013; Hörandel, 2003] and pulsars.

3. **Knee Region (10^{15} eV)**: A noticeable change in the spectral slope marks the knee, which is thought to indicate the energy limit of galactic acceleration mechanisms or the inability of the galaxy's magnetic field to contain higher-energy particles [Matthiae, 2019].

4. **Extragalactic Cosmic Rays**: At energies above the knee, extragalactic sources, such as active galactic nuclei (AGN) and gamma-ray bursts (GRBs), may become dominant contributors.

5. **Ankle Region (10^{18} eV)**: A spectral flattening at this energy signifies a transition from predominantly galactic to extragalactic cosmic ray populations,

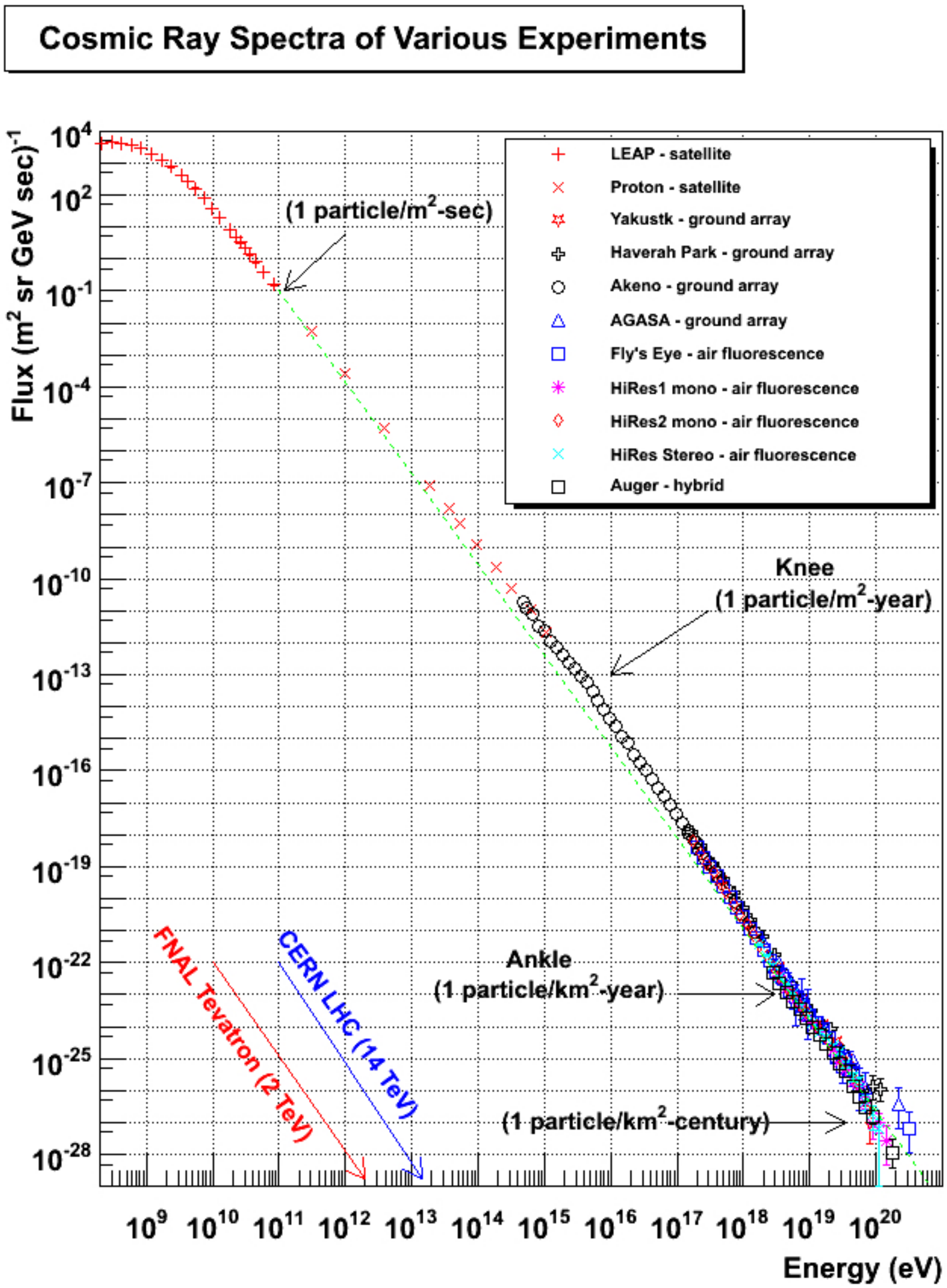

Figure 1.1: The energy spectrum for primary cosmic rays, obtained from 1.1

though the precise origin remains uncertain [Kampert & Tinyakov, 2014; Linsley, 1963].

6. **Ultra-High-Energy Cosmic Rays (UHECRs)**: With energies exceeding 10^{19} eV, these rare cosmic rays likely originate from the most extreme astrophysical environments. Their flux decreases steeply due to energy losses via interactions with the cosmic microwave background, a phenomenon known as the Greisen–Zatsepin–Kuzmin (GZK) cutoff [Greisen, 1966; Zatsepin & Kuz'min, 1966].

To uncover the origins of cosmic rays, various methods have been employed since their discovery. Potential acceleration sites have been identified, and neutral particles, which are unaffected by magnetic fields, can trace their sources. While neutrons decay quickly and neutrinos interact weakly, photons are easier to detect, making them ideal messengers for exploring the distant universe (Fig. 1.2). In 2007, the Pierre Auger Observatory demonstrated a correlation between the arrival directions of cosmic rays with energies above 6×10^{19} eV and the positions of AGN [Abraham et al., 2007]. This established AGNs as potential acceleration sites for high-energy cosmic ray production and high-energy photons as potential messengers of associated sources.

1.2 Gamma-ray sky as a probe for Cosmic messengers

Determining the origin of high-energy cosmic rays is challenging, as these particles, primarily charged protons and heavier ions, are deflected by galactic and intergalactic magnetic fields, obscuring their source of cosmic origin. However, interactions of cosmic rays with nearby matter produce secondary particles such as pions. Neutral pions decay into gamma-rays, while charged pions decay into neutrinos. Since these secondary particles are electrically neutral, they are unaffected by magnetic fields

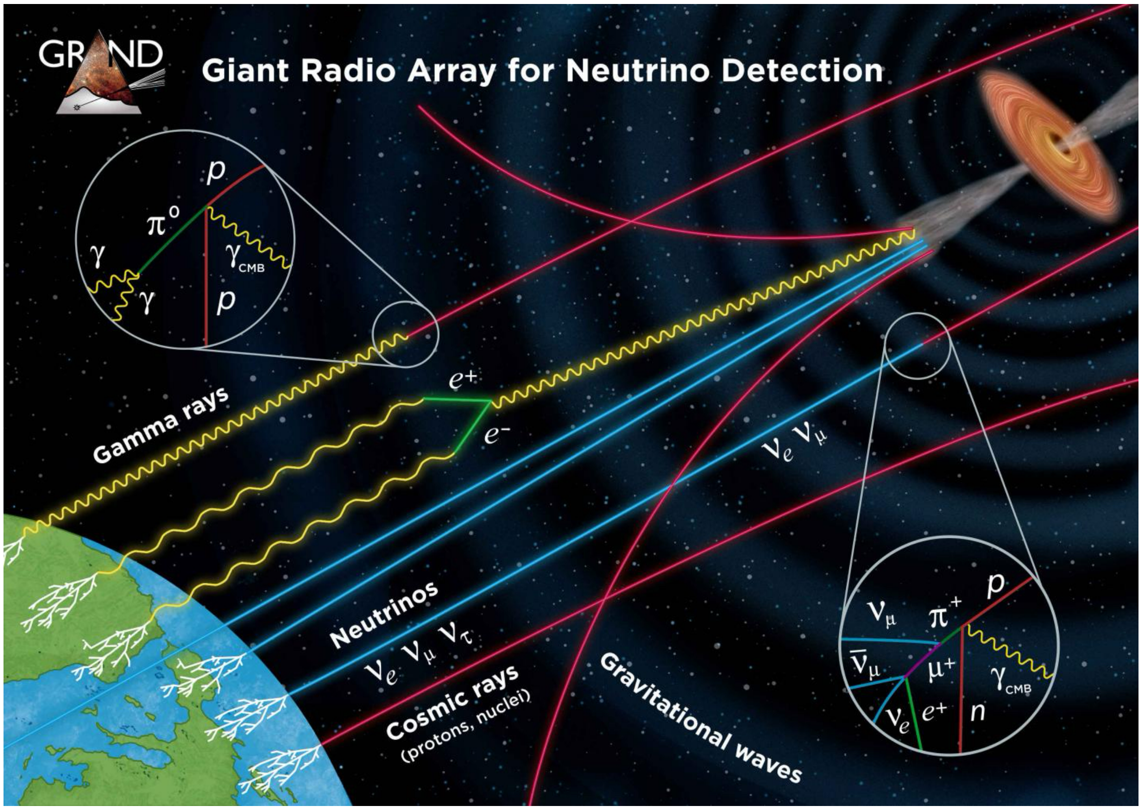

Figure 1.2: Creation and propagation of ultra-high energy particles in the universe [Álvarez-Muñiz et al., 2019].

and can retain information about their sources when detected on Earth (Fig. 1.2). High-energy gamma-rays and very-high-energy gamma-rays are particularly effective messengers for identifying cosmic ray acceleration sites. Analyzing their spatial and energy distributions may provide critical insights into the sources of cosmic rays and their interactions.

The emergence of multi-messenger astronomy, which combines observations of neutrinos, gravitational waves, cosmic rays, and electromagnetic signals, has significantly advanced our understanding of the high-energy universe over the past decade. Gravitational-wave detections from events such as neutron star mergers and stellar-mass black hole collisions, along with their electromagnetic counterparts, have provided valuable information about phenomena like gamma-ray bursts and fast radio bursts. These observations are essential for unraveling the connection between relativistic jets and high-energy particle acceleration.

The study of high-energy gamma rays from cosmic accelerators such as supernova remnants, pulsars, magnetars, and AGNs offers a unique perspective on extreme astrophysical phenomena and non-thermal particle acceleration. Recent advancements in multi-wavelength and simultaneous observational capabilities have greatly improved our understanding of the underlying mechanisms driving gamma-ray production.

Gamma rays are emitted by both Galactic and extragalactic sources. Locally produced gamma rays (within the Milky Way) provide information about their immediate environments, including interactions with nearby gas and dust. In contrast, gamma-rays from distant extragalactic sources, particularly those at redshifts $z > 1$, are significantly attenuated at energies above 100 GeV due to interactions with the extragalactic background light (EBL). This attenuation, while posing observational challenges, also offers a probe of the intergalactic medium and the conditions around these distant sources.

The following sections present details on key known gamma-ray emitters, highlighting their emission and production mechanisms.

1.2.1 Pulsars and Pulsars Wind Nebulae (Galactic)

Pulsars are highly magnetized, rapidly rotating neutron stars that convert rotational energy into particle energy, emitting periodic beams of electromagnetic radiation. These stars, with masses of $1.4 - 2M_{\odot}$ and radii around $10^6, \mathrm{cm}$ [Takata, 2016], produce gamma-ray emission from their magnetospheres, confined within the light cylinder. While most pulsars emit in the radio band, about 10% produce pulsed gamma-rays [Smith et al., 2023].

Gamma-ray production involves processes such as curvature radiation, synchrotron radiation, and inverse Compton scattering. Pulsar winds interact with the surrounding medium, forming shocks that accelerate particles and contribute to non-thermal broadband emission. Despite extensive research, the exact mechanisms behind multi-wavelength emissions remain debated, even for well-known pulsars like the Crab and Vela [Melrose & Rafat, 2017]. Key models, including the polar cap [Arons, 1981; Usov & Melrose, 1995] and outer gap [Cheng et al., 1986; Hirotani & Shibata, 1999], propose that curvature radiation from high-energy electrons sustains gamma-ray emission through pair production cascades [Aharonian & Bogovalov, 2003].

1.2.2 Supernova Shells (Galactic)

Supernovae are widely considered the primary sources of galactic cosmic rays, particularly those up to the knee region ($\sim 10^{15}$ eV) [Drury et al., 1994]. Charged cosmic rays are thought to be accelerated at supernova shock fronts through diffusive shock acceleration [Blandford & Eichler, 1987; Malkov & Drury, 2001]. However, the galactic magnetic field deflects these particles, making it challenging to directly trace their origins.

While direct detection of the origin of cosmic rays remains unfeasible, gamma-ray and optical observations provide indirect evidence for high-energy protons originating from supernovae [Ackermann et al., 2013; Giuliani et al., 2011; Nikolić et al., 2013]. Some studies suggest that additional sources, such as white dwarfs, may contribute to cosmic ray acceleration or that cosmic rays gain energy from multiple objects during their journey through the galaxy [Adriani et al., 2011; McKee, 2013].

1.2.3 Microquasar and X-ray Binaries

X-ray binaries consist of a donor star and a compact object, either a neutron star or a black hole, with accretion disks forming as infalling matter spirals toward the compact accretor. Thermal X-ray emission arises from the disk, heated to 10^7–10^8 K by repeated collisions.

Microquasars, a subclass of X-ray binaries with relativistic jets, resemble scaled-down AGNs but feature stellar-mass black holes [Fender, 2001]. Recent detections of very high-energy (VHE) γ-rays from microquasars by LHAASO suggest a hadronic origin, indicating particle acceleration up to 1 PeV and a potential contribution to galactic cosmic rays near the knee region [LHAASO Collaboration, 2024].

Particle acceleration in microquasars occurs at key sites, including termination shocks where jets interact with the ambient medium [Middleton et al., 2021], disk-driven sub-relativistic winds expanding into the surrounding environment [Li et al., 2020], and shear layers at the jet boundary [Rieger & Duffy, 2004]. Internal mechanisms such as magnetic reconnection and shocks within the jet also contribute to TeV-scale emission [Bosch-Ramon & Khangulyan, 2009].

1.2.4 Fermi bubble (Galactic)

Fermi Bubbles, discovered in gamma-ray observations by the Fermi Telescope, are two large, bi-conical structures extending $\sim$10 kpc above and below the galactic center [Su et al., 2010]. Similar features were previously observed in X-rays by the ROSAT All-Sky Survey [Snowden et al., 1997] and as microwave excesses by WMAP [Finkbeiner, 2004], with further confirmation from IRAS and Midcourse Space Experiment data [Law, 2010].

The origin of the Fermi bubbles is debated, with proposed mechanisms including jet-driven outflows [Guo & Mathews, 2012; Yang et al., 2012], spherical winds [Zubovas et al., 2011], accretion-driven shocks from the Galactic black hole [Cheng et al., 2011], and supernova-driven winds [Crocker & Aharonian, 2011]. High-ionization signatures in the Magellanic stream suggest past AGN activity [Bland-Hawthorn et al., 2013]. Studies reveal that gamma-ray emission from the bubbles likely arises from hadronic interactions of cosmic-ray protons with diffuse gas [Crocker & Aharonian, 2011] or inverse Compton scattering by high-energy electrons [Mertsch & Sarkar, 2011; Su et al., 2010].

1.3 Active Galactic Nuclei

Active Galactic Nuclei rank among the most energetic phenomena in the universe, with luminosities ranging from $10^{44} - 10^{50}\,\mathrm{erg\,s^{-1}}$ —far surpassing the output of stellar populations in normal galaxies. This extraordinary emission arises from a compact accretion region ($<< 1\,pc$) surrounding a supermassive black hole (SMBH; $\gtrsim 10^6\,M_\odot$) at the center of the galaxy, where accretion on SMBH converts part of its gravitational energy into radiation. This results in extremely luminous emission, surpassing the thermal emission from stars in the galaxy, making them visible up to extremely large redshifts (currently $z = 7.642$ Wang et al. [2021]). The dominant non-thermal emission in AGNs spans the entire electromagnetic spectrum, covering over 20 orders of magnitude in frequency. This broad emission makes AGNs detectable across all spectral bands. A subset of such active galaxies ($\sim$ 10%; Padovani et al. [2015]) hosts powerful relativistic jets, extending their emission up to γ-ray energies. The multi-wavelength emission of AGNs arises from distinct components, each contributing uniquely across the energy spectrum. Observations at different wavelengths reveal these individual components and their characteristics. These dominating emission signatures and their associated AGN components are highlighted in Figure 1.4 and described below:

1. **Radio Emission**: Originates from the AGN core, jets, and lobes. The spectrum is typically associated with synchrotron spectrum.

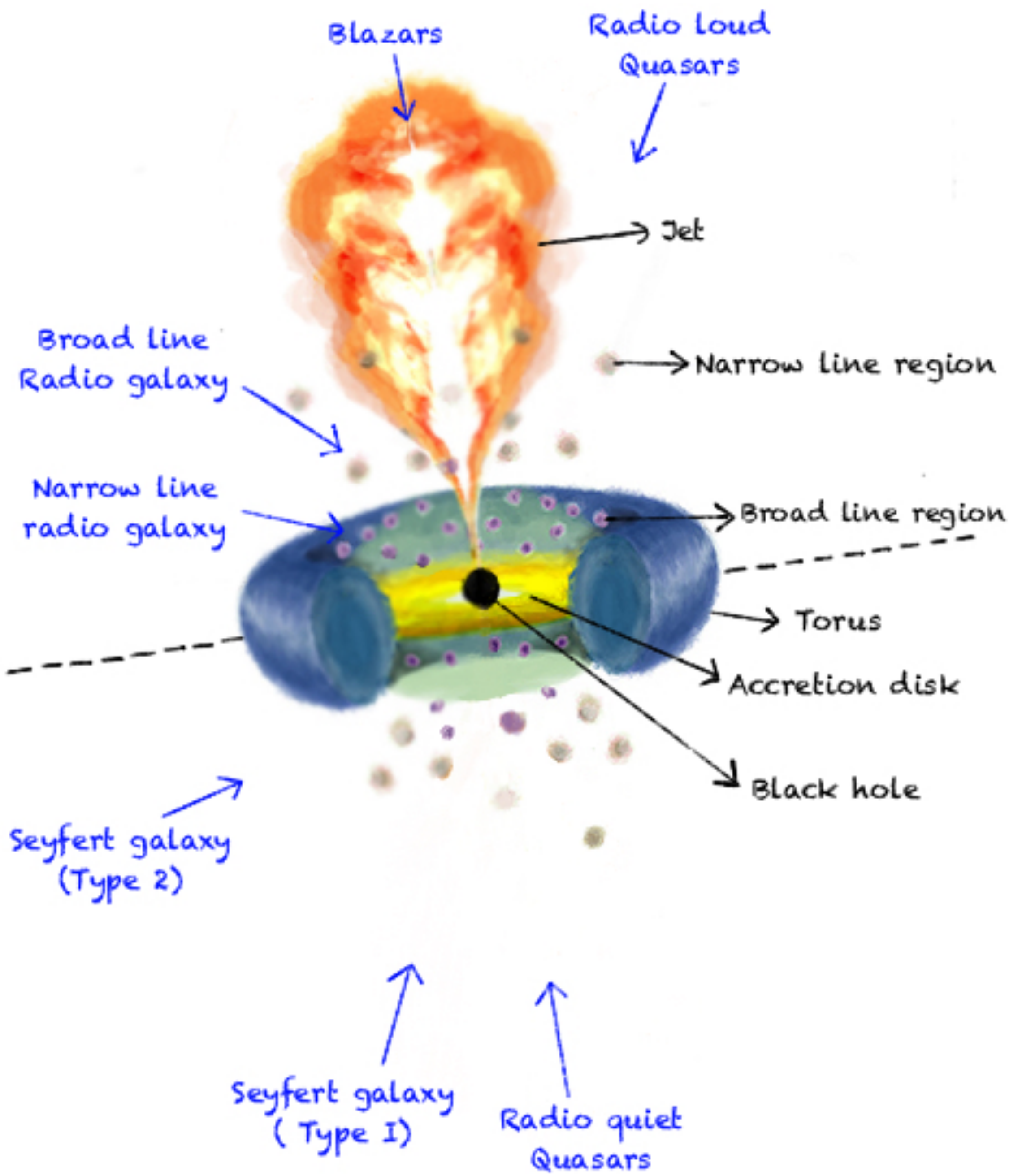

Figure 1.3: Components of AGN and the unification of the AGNs using the unification model by Urry & Padovani [1995] Image credit: Adapted from Berton et al. [2017]

2. **Thermal Infrared**: Emission from the dusty torus, located a few parsecs from the SMBH.

3. **Optical/Ultraviolet Broad Emission Lines**: High-velocity (1000 to 10000 kms^{-1}) lines from dense clouds ($n_e = 10^9\,\mathrm{cm}^{-3}$) within ∼1 parsec of the SMBH [Peterson, 2006].

4. **Optical Narrow Emission Lines**: Low-velocity ($30 - 1000\,\mathrm{km\,s}^{-1}$; Ruiz et al. [2005]) lines from extended low-density gas ($n_e = 10^3\,\mathrm{cm}^{-3}$; Peterson [2006]) at distances of 100–300 pc.

5. **Optical/Ultraviolet/Soft X-rays**: Thermal emission from the accretion disk as matter falls onto the supermassive black hole (SMBH).

6. **Hard X-rays (E > 1 KeV)**:
   Continumm: Emission from thermal Comptonization in the accretion disk corona [Liu & Mineshige, 2002] and non-thermal jet emission indicated as a power-law spectrum.
   Line emission X-ray line emission occurs when heavy elements are illuminated by X-ray continuum, causing fluorescence, such as the Fe-K line centered at 6.4 keV.

7. **Gamma Rays**: Predominantly non-thermal emission from relativistic jets.

The different components resulting in broadband emission are represented in the Figure 1.3. A comprehensive understanding of AGNs requires simultaneous, multi-wavelength observations across the electromagnetic spectrum.

The current classification of AGNs, based on observational studies, has led to a diverse array of categories, often described as a complex and confusing "AGN zoo" [Padovani et al., 2017]. Over time, these categories have been understood to arise from differences in key physical parameters of similar objects, including their orientation with respect to the observer [Antonucci, 1993; Urry & Padovani, 1995], the presence or absence of relativistic jets [Padovani, 2024], accretion rates [Heckman & Best, 2014], and the characteristics of the host galaxy and the geometry of its environment.

A widely accepted unification model by Urry & Padovani [1995] suggests that all AGNs host a central SMBH accreting matter from a surrounding disk. This accretion process powers AGN luminosity through the gravitational energy of the infalling material. Additionally, if the black hole is spinning, electromagnetic energy is extracted from the black hole itself [Blandford & Znajek, 1977]. The accretion disk also converts gravitational potential energy and emits radiation across different wavelengths depending on temperature gradients: the hotter inner regions emit ultraviolet (UV) radiation, while the cooler outer regions radiate in the optical. Hard X-rays originate from a hot plasma "corona" near the black hole, while dusty clouds in 'Torus', surrounding the disk emit thermal infrared radiation.

The fast-moving molecular clouds within the black hole's gravitational potential reprocess radiation from the accretion disk, producing broad optical and ultraviolet emission lines, while slower-moving clouds farther out generate narrow emission lines. Collimated relativistic jets, which are most prominent in radio-loud AGNs, pierce through the medium and are visible as beamed plasma outflows emitting non-thermal synchrotron radiation. Additionally, in some AGN jets, high-energy emission is also observed, probably from inverse Compton (IC) scattering or hadronic processes, depending on the composition of the jet.

The axisymmetric structure of AGNs causes their observed appearance to vary significantly with viewing angle, as shown in Figure 1.3. The orientation with respect to the observer determines which components dominate the observed emission, underpinning the classification of AGNs into distinct types while highlighting their shared underlying structure.

Approximately $\sim 80 - 85\%$ of active galaxies are radio-faint and classified as radio-quiet AGNs, while the remaining fraction, termed radio-loud AGNs, exhibit a radio (5 GHz) to B-band optical flux ratio exceeding 10 ($F_5/F_B \gtrsim 10$). These two classes differ significantly in their jet properties: radio-quiet AGNs host weak and slow jets, while radio-loud AGNs produce strong, relativistic jets that contribute substantially to their total nonthermal emission [Kharb et al., 2024].

The observed properties of AGNs are strongly influenced by their orientation relative to the observer. When viewed edge-on, the thick dusty torus obscures the broad-line region, making the narrow emission lines more prominent. In this configuration, radio-loud AGNs are classified as narrow-line radio galaxies (NLRGs), characterized by distinct jet emission, whereas radio-quiet AGNs are identified as Seyfert 2 galaxies. As the line of sight shifts closer to the longitudinal axis of the torus, the broad-line region becomes visible, leading to prominent optical broad emission lines. In this orientation, radio-loud AGNs are termed broad-line radio galaxies (BLRGs), while radio-quiet AGNs are referred to as Seyfert 1 galaxies.

When the observer's line of sight is aligned face-on along the polar axis of the system, jet emission dominates the spectrum. For some radio-loud AGNs, this orientation results in broadband emission up to GeV and TeV energies due to relativistic effects. In BL Lacertae (BL Lacs) objects, this alignment produces jet-dominated emission that often lacks strong spectral lines. Flat-spectrum radio quasars (FSRQs), another subset, exhibit broad-line region features. Both BL Lacs and FSRQs, collectively known as blazars, are characterized by jet-boosted emission, making them key systems for studying variable gamma-ray production in AGNs.

1.4 Blazars

The term "blazar," a combination of BL Lac and FSRQ (quasi-stellar objects), was first introduced by Ed Spiegel during a dinner talk at the Pittsburgh Conference on BL Lac Objects, approximately 45 years ago [Blandford et al., 1978]. Historically referred to as optically violently variable quasars, blazars are now recognized as radio-loud AGNs with jets aligned within 5° of the observer's line of sight [Urry & Padovani, 1995]. This specific jet orientation causes the resulting emission to outshine that of the accretion disk, producing highly beamed and Doppler-boosted radiation.

Blazars exhibit extreme luminosities and variability across the electromagnetic spectrum, from radio to gamma rays, with high polarization and flux variability timescales ranging from years to minutes. The extremely rapid variability observed in such sources suggests compact emission regions smaller than the black hole's light-crossing time, pointing to complex particle acceleration mechanisms (discussed further in §1.4.3). Additionally, blazars are prominent TeV $\gamma-$ray emitters, with their emission spanning from radio to TeV energies. Out of the 89 known extragalactic VHE AGN, 83 are blazars, emphasizing their dominance in this energy regime. Two additional sources, IC 310 and PKS 0625-35, display mixed features of radio galaxies and BL Lacs [Rulten, 2022] (see also TeVCat, http://tevcat.uchicago.edu/).

1.4.1 Relativistic effect

Blazars, with their relativistic jets closely aligned to our line of sight, exhibit significant relativistic effects that profoundly influence their observed properties. For a source moving with velocity $v = \beta c$ towards the observer, the observed flux undergoes Doppler boosting. This causes time intervals in the observer's frame (t) to appear shorter than those in the source's rest frame (t'), as the source "catches up" to its emitted light [Urry & Padovani, 1995]:

$$t = \frac{t'}{\delta}. \tag{1.1}$$

The Doppler factor δ, which governs these effects, is given by:

$$\delta = [\Gamma(1 - \beta \cos\theta)]^{-1}. \tag{1.2}$$

where Γ is the Lorentz factor and θ is the angle between the velocity vector and the observer's line of sight. For blazars, typical Doppler and Lorentz factors are on the order of 10-30, as derived from multiple SED modeling [Buson et al., 2014; Sahakyan & Giommi, 2022].

Doppler boosting amplifies the observed flux and luminosity, making blazars appear exceptionally bright and energetic. The intensity in the observer's frame $I_\nu(\nu)$ is related to the rest-frame intensity $I'_{\nu'}(\nu')$ as:

$$I_\nu(\nu) = \delta^3 I'_{\nu'}(\nu'). \tag{1.3}$$

For isotropic emission in the rest frame and a power-law spectrum, $F'_{\nu'} \propto (\nu')^{-\alpha}$, the flux density transforms as:

$$F_\nu(\nu) = \delta^{3+\alpha} F'_{\nu'}(\nu'). \tag{1.4}$$

In blazars, the relativistic alignment leads to Doppler factors of ~ 10, significantly boosting the observed flux and luminosity. Additionally, it shortens observed variability timescales, allowing rapid changes in flux to be detectable on timescales much shorter than in the rest frame. These relativistic effects are key to understanding the extreme brightness, rapid variability, and broad spectral energy distributions (SEDs) characteristic of blazars.

1.4.2 Spectral energy distribution of Blazars

Over the past decade, simultaneous multi-wavelength campaigns have provided a comprehensive broadband view of blazars, revealing their extended non-thermal emission from radio to TeV gamma-ray energies. As jet emission dominates over the accretion disk, the observed SED offers insights into the radiation mechanisms within the blazar jet. The broadband SED exhibits two distinct humps: the first, spanning from radio to soft X-rays, is attributed to non-thermal synchrotron emission from population of charged particles (electrons/positions) in a magnetic field. This is further supported by the detection of polarized emission in blazars. The second peak, extending from hard X-rays to gamma-rays (GeV to TeV), is thought to arise from either the upscattering of low-energy photons via the inverse Compton process—through synchrotron self-Compton within the jet or external Compton scattering with photons outside the jet—or from hadronic processes. However, the exact origin of this second peak remains uncertain and is a key unresolved question in the field. This is discussed in details in §1.4.2.1 and §1.4.2.2

FSRQs exhibit a low-energy peak in the infrared and a high-energy peak at MeV energies, with the second peak being significantly more luminous than the first, reflecting their high Compton dominance [Ghisellini et al., 2017]. In contrast, BL Lac objects show a range of peak variability in the location of their low-energy peak, with both synchrotron and high-energy peaks displaying comparable luminosity. The position of the low-energy peak further classifies BL Lacs into distinct subclasses:

- Low frequency peaked Bl lac (LBL; $\nu \leq 10^{14}$ Hz)
- Intermediate frequency peaked Bl lac (IBL; $10^{14} \leq \nu \leq 10^{15}$ Hz)
- High frequency peaked Bl lac (HBL; $\nu \geq 10^{15}$ Hz)

The subsequent SEDs for the LBL and HBL classes are shown in Figure 1.4. As seen, the HBL class shows a higher likelihood of VHE detection. A subset of BL Lac objects has exhibited class transitions during different flux states (flaring or quiescent states), marked by significant shifts in the SED peak from HBL to LBL and vice versa [Giommi & Padovani, 2021]. The flux-dependent nature of these transitions remains poorly understood. Such phenomena, observed in sources like BL Lac, are explored in subsequent chapters.

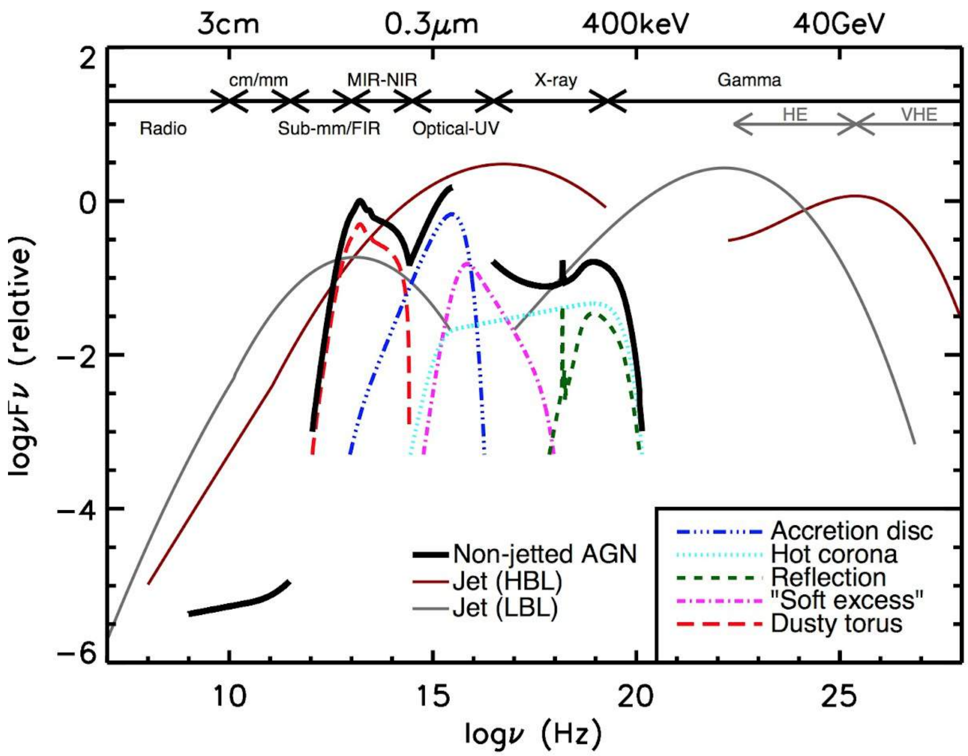

Figure 1.4: Broadband SED of Blazar jet highlighting different Image credit: [Padovani, 2024] adapted from a figure by [Harrison, 2014]

The underlying physics governing SEDs and their peak transitions, particularly the origin of the second hump and the mechanisms driving high-energy emission, remains uncertain. Current models suggest that jet composition plays a pivotal role in these processes.

1.4.2.1 Leptonic emission

Leptonic emission explains the high-energy blazar emission, assuming that the bulk radiation is produced by relativistic electrons (or positrons) within the jet. In leptonic models, high-energy emission arises from inverse-Compton scattering, where the same electrons or positrons responsible for the low-energy synchrotron component upscatter low-energy synchrotron photons. High-energy gamma-ray emission is considered to result from the upscattering of low-energy optical or X-ray seed photons in the leptonic scenario. If these seed photons originate from synchrotron emission by the same relativistic particles, the process is termed synchrotron-self-Compton (SSC) [Bloom & Marscher, 1996]. Alternatively, if the photons are external to the relativistic jet, it is referred to as external inverse-Compton (EIC).

EIC modeling typically involves external photon fields such as thermal emission from the SMBH accretion disk [Dermer & Schlickeiser, 1993; Dermer et al., 1992], emission lines from the broad-line region (BLR) [Finke, 2016; Sikora et al., 1994], or thermal infrared radiation from the dusty torus [Błażejowski et al., 2000; Kataoka et al., 1999] or CMB [Böttcher et al., 2008; Meyer et al., 2015; Sanchez et al., 2015; Yan et al., 2012; Zacharias & Wagner, 2016]. While these radiation fields facilitate high-energy γ-ray production, they also increase opacity, causing γ-rays to be absorbed and undetectable. However, this opacity can be utilized to further investigate γ-ray production sites by analyzing the imprint of soft photons on the high-energy γ-ray spectrum. Such signatures of local jet environment have been explored to uncover the origin of gamma-rays in blazar jets and is discussed further in Chapter 4. Since these photon fields are directly observed in FSRQs, the EIC scenario is often successfully applied to their modeling. In contrast, the SSC model is more effective for explaining the high-energy emission in HBLs [Cerruti, 2020].

1.4.2.2 Hadronic emission

Hadronic models propose that high-energy emission in blazars arises from relativistic protons and other hadrons in the jet, presenting an alternative to leptonic models. In these frameworks, the second hump in the SED is attributed to proton-synchrotron radiation, where gamma-rays are produced as relativistic protons spiral in strong magnetic fields (B$\sim 10-100$,G) [Petropoulou & Mastichiadis, 2012; Reimer, 2012]. Additionally, high-energy protons interacting with low-energy photons via the p-γ

process generate pions (π_o, π_+, π_-), which decay into gamma-rays and neutrinos, the latter being a distinct signature of hadronic processes [Becker et al., 2011].

Hadronic models are particularly compelling as they offer a mechanism for accelerating cosmic rays to ultra-high energies ($\sim 10^{20}, \mathrm{eV}$) and can account for features such as orphan TeV flares, which are challenging to explain with leptonic scenarios. However, distinguishing between leptonic and hadronic models remains difficult, as both can reproduce the observed SEDs of blazars [Böttcher et al., 2013]. A significant drawback of hadronic models is their reliance on extreme physical parameters, such as high magnetic fields, energy budgets, and plasma densities, to support particle acceleration and explain rapid gamma-ray variability.

Recent observations offer strong evidence for hadronic activity. In 2017, a high-energy neutrino ($E \sim 290\,\mathrm{TeV}, > 3\sigma$) was detected in correlation with the blazar TXS 0506+056 [IceCube Collaboration et al., 2018a], while IceCube later identified a stronger neutrino signal ($> 4.2\sigma$) from the Seyfert galaxy NGC 1068 [IceCube Collaboration et al., 2022]. More such associations have been drawn in two blazars: PKS 1502+106 [Taboada & Stein, 2019] and PKS 1424−41 [Kadler et al., 2016], and three radio galaxies: NGC 3079, NGC 4151, CGCG 420−015 [Abbasi et al., 2024; Goswami, 2023; Neronov et al., 2024]. Possible neutrino emission can also be associated with the two blazars: PKS 1424+240 (3.7σ) and GB6 J1542+6129 (2.2σ) [IceCube Collaboration et al., 2022].

High-energy neutrino production in these environments is often accompanied by gamma rays. However, in regions near the central black hole, abundant infrared-optical and X-ray photons facilitate pair production, reprocessing gamma rays into hard X-rays (≤ 1 MeV) [Kun et al., 2024]. This explains the reduced γ-ray flux relative to neutrinos in sources like Seyfert galaxies.

1.4.3 Particle acceleration models

While leptonic and hadronic emission point to broadband radiation mechanisms in the blazar jet, the understanding of particle acceleration remains an open question. The current understanding, supported by theoretical models and simulations, suggests that jets start off with the majority of their energy locked in magnetic fields [Komissarov et al., 2009; Lyubarsky, 2009; Tchekhovskoy et al., 2009]. These magnetic fields drive the flow outward, potentially accelerating it to relativistic speeds. However, observations indicate that by the time the jets reach their emission regions, the energy densities of the magnetic fields and the radiating particles are roughly in equilibrium [Celotti & Ghisellini, 2008; Ghisellini et al., 2014; Readhead, 1994]. This transition, from a magnetically dominated state to one where energy is more evenly distributed among particles, remains a major open question.

The uncertainty surrounding the source of jet power leads to several distinct scenarios for the dissipative mechanisms driving jet emission [Matthews et al., 2020]. Here, we briefly discuss two well-known energy dissipation mechanisms, further explored in the thesis, as a way to understand the origin of jet power and the underlying particle acceleration mechanism.

1.4.3.1 Shock

Shocks are a well-established mechanism for particle acceleration, effectively energizing particles to extremely high energies over short timescales and driving the non-thermal emission observed in blazars [Wang, 2002]. These shocks can be classified as internal, caused by collisions between faster and slower regions within the jet, or external, resulting from interactions with the surrounding medium. Emission from various shock components along the jet combines to produce the observed broadband spectrum.

If particle acceleration is dominated by diffusive shock acceleration, particles gain energy by repeatedly crossing the shock front, resulting in a power-law energy distribution [Baring et al., 2016]. Subsequently, these accelerated particles emit synchrotron radiation at low energies and inverse Compton radiation at high energies, forming the characteristic double-humped spectral energy distribution of blazars. Shocks also account for variability, polarization, and other observational features of blazars.

Shocks are effective in explaining correlated multi-wavelength variability. However, fast variability, requiring emission regions smaller than the jet cross-section, poses challenges for this scenario. For a black hole of mass $M_{BH} = 10^9\,\mathrm{M}_\odot$, the Schwarzschild radius ($r_g = 2GM/c^2$) corresponds to a light crossing timescale of $t_g = 160(M_{BH}/10^9 M_\odot)$ minutes. Variability on timescales shorter than this implies either sub-horizon scale emission regions [Aleksić et al., 2014] or regions with extremely high Doppler factors [Begelman et al., 2008; Giannios et al., 2009; Narayan & Piran, 2012a].

Such compact emission regions face significant opacity constraints for high-energy emission [Begelman et al., 2008; Finke et al., 2008], making fast variability difficult to reconcile with the standard shock-in-jet model, highlighting the need for alternative explanations.

1.4.3.2 Magnetic reconnection

Magnetic reconnection provides a compelling mechanism for converting magnetic energy into radiation, particularly near the base of blazar jets [Sironi et al., 2015]. A likely scenario for reconnection in jets involves oppositely directed magnetic field lines breaking and reconnecting within plasma, releasing magnetic energy that is rapidly converted into plasma heating, bulk kinetic energy, and non-thermal particle acceleration. In blazar jets, reconnection typically takes place in regions with complex magnetic fields or turbulence, close to the central engine.

According to Giannios [2013], a single magnetic reconnection event can produce a chain of plasmoids—compact, magnetized structures with varying sizes and relativistic speeds in the jet's co-moving frame. These plasmoids grow by merging with neighboring plasmoids or accreting plasma through secondary current sheets. As the emitting region moves with a co-moving Lorentz factor (Γ_{co}) of a few, the effective jet Lorentz factor (Γ_j) decreases.

The Doppler factor, $\delta \sim \Gamma_{co}\Gamma_j$, can exceed 40 for typical Γ_j values, enabling short-timescale variability (minutes) without requiring extremely high jet Lorentz factors ($\Gamma >> 10$). When aligned with the observer, plasmoids with high Doppler factors are strong candidates for producing rapid, short-duration γ-ray flares observed in blazars. This makes magnetic reconnection a viable explanation for the ultra-rapid variability in blazars, including sub-hour timescales.

1.4.4 Origin of variable flaring emission - multi-wavelength variability

The variable emission in blazars is closely linked to the timescales of particle acceleration and cooling processes. Variability across varying timescales and wavelengths is intrinsic to the light curve and is often found to be correlated, hinting at co-spatial emission within the jet.

Advances in gamma-ray observatories, such as the Large Area Telescope onboard Fermi and VHE instruments like the High-Altitude Water Cherenkov (HAWC) and First G-APD Cherenkov Telescope (FACT) observatories, have revolutionized high-energy sky monitoring by enabling continuous, long-term, and simultaneous observations coordinated with low-energy emission. VHE facilities like Imaging Atmospheric Cherenkov Telescopes (IACTs), including HESS, MAGIC, and VERITAS, have further expanded observational capabilities, allowing the detection of minute-scale variability and providing additional constraints on jet parameters and particle acceleration mechanisms.

Blazar variability refers to significant flux changes relative to mean levels and is characterized by distinct periods of activity. Long-term multi-wavelength light curves reveal flux enhancements marked by a rise and subsequent decay, commonly referred to as 'flaring' epochs. These active phases are interspersed with periods of no significant variability, termed 'quiescent' states. Such variability is a hallmark of blazar light curves, reflecting the complex dynamics of relativistic jets.

Key variability features observed in long-term blazar monitoring are discussed in the following sections.

1.4.4.1 Short term variability

Sub-horizon variability ($t_{var} \leq 2GM/c^3$) indicates an emission region smaller than the black hole size, suggesting either a compact region near the central engine or a high Doppler factor, implying larger variability in the jet frame. Such variability in light curves is quantified using the flux doubling or halving timescale:

$$t_{var} = (t_2 - t_1)\frac{\ln 2}{\ln(F_2/F_1)} \tag{1.5}$$

Fast variability is predominantly observed in high-energy gamma-ray light curves but remains rare. Out of over ∼3130 known blazars [Ballet et al., 2023], only seven have shown significant rapid variability: three BL Lacs (Mrk 501 [Albert et al., 2007], PKS 2155-304 [Aharonian et al., 2007], BL Lac [Arlen et al., 2012; MAGIC Collaboration et al., 2019]), three FSRQs (PKS 1222+21 [Aleksić et al., 2011a], 3C 279 [Ackermann et al., 2016; Shukla & Mannheim, 2020a], CTA 102 [Shukla et al., 2018]), and one radio galaxy (IC 310 [Aleksić et al., 2014]). Most detections are associated with VHE flares, except for two cases—3C 279 [Ackermann et al., 2016] and CTA 102 [Shukla et al., 2018]—where rapid variability was identified in GeV energies using Fermi-LAT. These rare events provide critical insights into extreme particle acceleration processes.

The origin of fast variability is attributed to processes like stochastic particle acceleration, internal shock formation, or mini-jets within jets triggered by magnetic reconnection due to turbulence or kink instabilities [Aleksić et al., 2014; Banasiński et al., 2016]. Certain physical scenario, like jet-star interaction [Giannios et al., 2009], can additionally contribute to the observed variability [Böttcher, 2019]. Despite decades of data, the exact mechanisms and emission region locations remain debated and poorly understood.

1.4.4.2 Long term variability

In addition to short-term variability, blazar light curves exhibit long-term flux evolution over timescales of days, months, and years, particularly prominent at lower frequencies, such as radio and optical wavelengths. This long-term variability can often be explained by the shock-in-jet model, first proposed by [Marscher & Gear, 1985] and later refined by [Boettcher & Dermer, 2010]. In this scenario, variability constrains the emission region size as $R_{\rm emm} = c\, t_{\rm var}\, \delta/(1+z)$, and its location relative to the central engine as $R_{\rm diss} = 2c\Gamma^2 t_{\rm var}$, where Γ is the bulk Lorentz factor. Larger variability timescales suggest emission occurring farther down the jet.

Long-term flux evolution may also result from the coinciding rise and fall of flux from multiple emission regions, producing broader variability patterns. Improved time resolution, as expected with the upcoming Cherenkov Telescope Array (CTA), will enhance the ability to discern contributions from multiple emission zones. Blazar long-term light curves exhibit pink-to-red noise behavior in their power spectral density [Goyal et al., 2022], reflecting intrinsic long-term memory in high-energy emissions.

Some blazars, including PKS 2155-304 (1.7 years), Mkn 501 (0.9 years), BL Lac (1.8 years), PG 1553+113 (2.2 years), PKS 0426-380 (3.4 years), PKS 0537-441 (0.8 years in high state), and PKS 0310-243 (2.1 years), have shown indications of year-long high-energy periodicity [Rieger, 2019]. While often attributed to supermassive black hole binaries, such periodicity lacks significant confirmation due to limited data spans.

Variability patterns in blazar light curves provide insights into the jet geometry and emission regions. However, for high-redshift blazars, gamma-ray detection is often limited by EBL absorption. Gravitationally lensed quasars offer a unique opportunity to study jet dynamics by magnifying high-energy emission and revealing delayed flares in high-redshift blazars. These delays serve as critical probes of gamma-ray dissipation sites, enabling constraints on jet emission mechanisms. Chapter 5 explores this using advanced time-domain analysis techniques.

Time-domain studies of blazar light curves reveal hidden patterns, trends, and periodicities, offering valuable insights into the long-term evolution of flux and jet dynamics. This thesis explores flux evolution in blazar jets to investigate the origins of high-energy gamma-ray flares.

1.5 Layout of the Thesis

This thesis presents a multi-wavelength study of bright blazars known for prominent gamma-ray and X-ray flares. The research focuses on short- and long-term flaring emissions to constrain and understand the energy dissipation sites within blazar jets. As discussed in Section 1.4.3, the study investigates radiation and particle acceleration mechanisms to characterize the "blazar zone", the region of dominant emission, and to identify the baseline emission regions responsible for long-term flux evolution in high-energy light curves.

Key questions addressed in this thesis include:

1. The origin of high-energy cosmic rays and the role of blazars as potential cosmic accelerators.

2. The jet composition: electron-dominated, proton-dominated, or a mix of both.
3. The location and structure of dominant emission regions in blazars.
4. The origin of rapid variability in blazars across multiple timescales.
5. The role of the external jet environment in gamma-ray production and particle acceleration.
6. The dominant acceleration mechanisms sustaining particle energy over large jet distances.

The analysis utilizes $\sim$15–16 years of gamma-ray data from Fermi-LAT, supplemented with X-ray and optical observations from facilities such as Swift, to study blazar emissions. Additionally, the thesis examines GeV gamma-ray emission from extended regions of the sky associated with gravitational wave or IceCube neutrino association to explore blazars as potential neutrino factories and considers other cosmic-ray accelerators, including gamma-ray bursts.

This thesis utilizes 15–16 years of gamma-ray data from Fermi-LAT, along with X-ray and optical observations from Swift, to investigate blazar emissions. Additionally, the thesis examines GeV gamma-ray emission from extended sky regions associated with gravitational wave events or IceCube neutrino detections, exploring blazars as potential neutrino factories and considering other cosmic ray accelerators, such as gamma-ray bursts.

The contents of the thesis are laid out as follows:

Chapter 1: Introduces the field of gamma-ray astronomy and highlights the current open questions. It provides an overview of gamma-ray emission sources, with a detailed discussion on blazars as key candidates for variable gamma-ray studies.

Chapter 2: Describes the multiwavelength instruments and methodologies utilized in this work, focusing on techniques to investigate variable gamma-ray emission.

Chapter 3: Presents a multiwavelength analysis of BL Lac objects, emphasizing their spectral transition behavior and the associated particle acceleration mechanisms.

Chapter 4: Examines the origin of flaring and quiescent activity in high-energy gamma-ray bands through dedicated observational studies.

Chapter 5: Investigates the flaring behavior of the high-redshift lensed blazar PKS 1830-211 using advanced time-series analysis techniques.

Chapter 6: Details the development of a novel tool designed to explore GeV gamma-ray emission across extended sky regions.

Chapter 7: Concludes the thesis with a summary of findings and a discussion on potential avenues for future research in gamma-ray astronomy.

Chapter 2

Multi-wavelength data reduction and adopted methodologies

This thesis investigates the flaring activity of GeV blazars and to uncover the processes driving their variable emissions across diverse timescales. Blazars, known for their powerful relativistic jets and broadband emissions dominated by non-thermal processes, require multi-wavelength observations to form a comprehensive understanding of their behavior. To achieve this, we utilized data from multiple space-based observatories, including γ-ray data from *Fermi* Large Area Telescope (LAT) and X-ray, UV, and optical observations from *Swift* Observatory. The launch of the *Fermi* Gamma-ray Space Telescope in 2008 revolutionized the study of the high-energy γ-ray sky, enabling unprecedented long-term monitoring of blazar activity. This thesis utilizes long-term monitoring capabilities of *Fermi*-LAT and the rapid response of *Swift* to probe the processes occurring in the vicinity of the central black hole system. A brief description of the data, instrumentation, and its analysis procedure used in this study is discussed further in the chapter.

2.1 *Fermi* Telescope

The *Fermi* Gamma-ray Space Telescope, named after physics pioneer Enrico *Fermi*, is a pioneering satellite observatory designed to detect photon energies ranging from

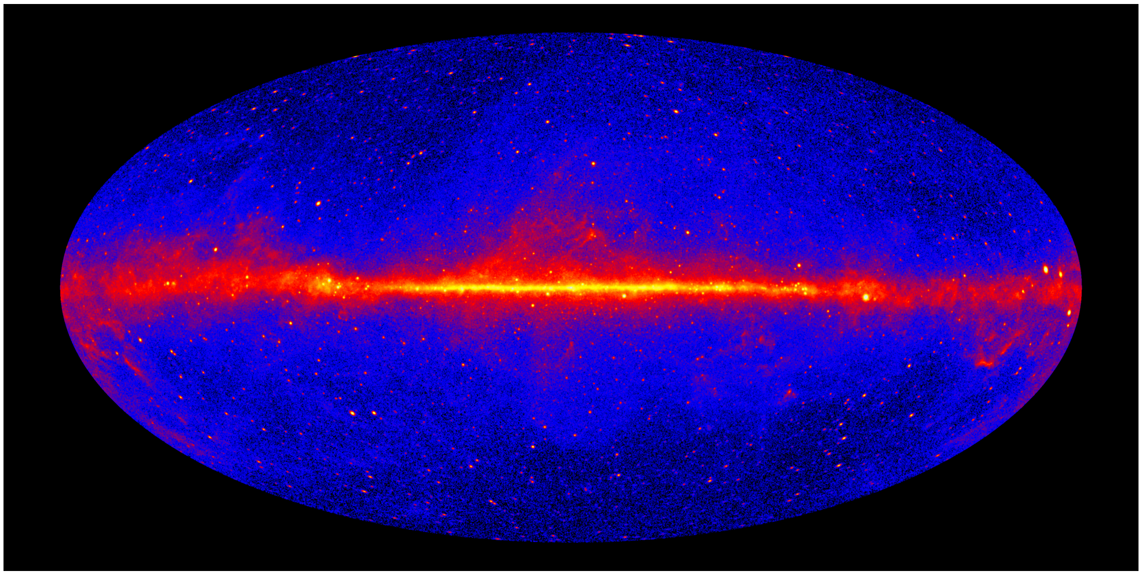

Figure 2.1: Entire high energy sky as observed by *Fermi*'s LAT over 12 years, using front-converting γ rays with energies exceeding 1 GeV. The most striking feature is the bright, diffuse band along the center, representing the Milky Way's central plane. Here, gamma rays are primarily produced by energetic particles, accelerated in supernova shock waves, colliding with interstellar gas and light. Above and below the plane, the star-like features are distant galaxies powered by supermassive black holes, while many bright sources along the plane are pulsars. Image Credit: NASA/DOE/Fermi LAT Collaboration

8 keV to over 300 GeV. It was formerly called the Gamma-ray Large Area Space Telescope (GLAST) but was later renamed post-launch. Launched on June 11, 2008, it orbits Earth at an altitude of 535 km with a 26° inclination, completing an orbit every 96 minutes. Since its launch, *Fermi* has revolutionized our understanding of the cosmos, with a sensitivity factor 30 times greater than that achieved by earlier gamma-ray missions such as EGRET [Strigari, 2013]. *Fermi* has mapped the entire sky in gamma-rays, the highest-energy radiation, and has detected thousands of sources so far. The gamma-ray sky using 12 years of *Fermi*-LAT observations is shown in Figure 2.1.

Fermi is equipped with two state-of-the-art scientific instruments onboard: (1) the

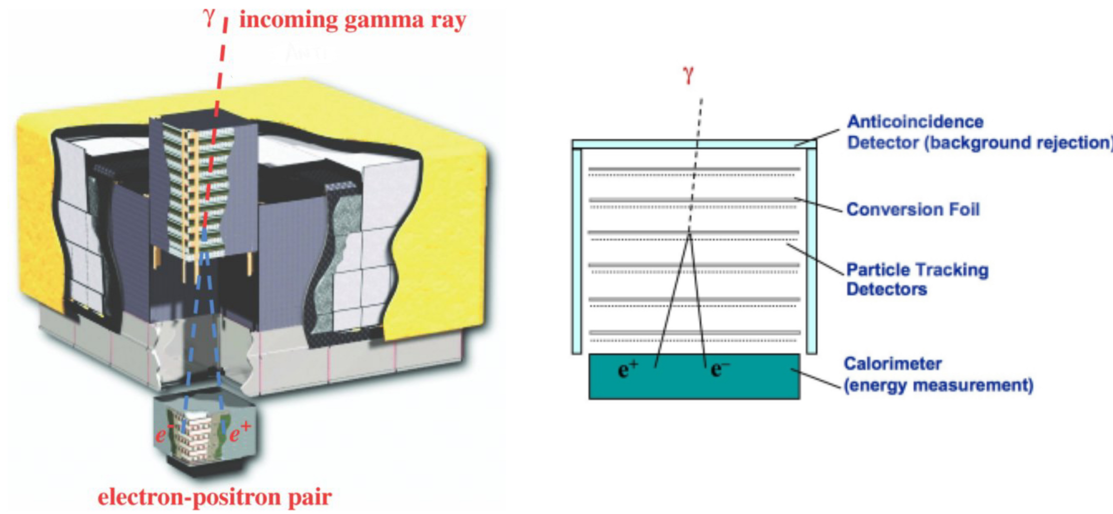

Figure 2.2: (Left) Cutaway of Large Area Telescope onboard *Fermi* Gamma-ray Space Telescope. Figure credit - Atwood et al. [2009]

Large Area Telescope and (2) the Gamma-ray Burst Monitor (GBM). The LAT is *Fermi*'s primary instrument, while the GBM, operating from 8 keV to 40 MeV, complements it by monitoring γ-ray transients.

The LAT utilizes the pair conversion technique to observe the high-energy sky in the 0.2–300 GeV range. As shown in Fig. 2.3, the instrument features 16 layers of high-Z tungsten material, where incoming γ-rays convert into an electron (e^-) and positron (e^+) in the field of a heavy nucleus.

These conversion layers are interleaved with 18 xy silicon strip detector planes, which trace the trajectories of the resulting particles, enabling the reconstruction of the event's direction. A calorimeter, comprising 96 CsI(Tl) crystals in a hodoscopic configuration, measures the particles' energies and provides 3D imaging resolution for precise event characterization. By combining the energy deposited in the calorimeter with the x-y coordinates of each event tracked on the silicon strip detector, one can reconstruct the particle trajectory and energy losses. Both onboard and ground-based analyses use these data to trace the paths of charged particles and characterize the interactions that generated them. This process accurately identifies photon events and determines their direction and associated energy. Background noise from charged particles is effectively suppressed using a segmented anticoincidence detector (ACD) that surrounds the tracker array, enabling efficient background rejection.

The LAT flags γ-ray events over charged particle events by utilizing three primary identifiers:

1. No signal in the anticoincidence detector,
2. Multiple tracks originating from the same location within the tracker,
3. An electromagnetic shower detected in the calorimeter.

The LAT observes 20% of the sky at any moment and is optimized for all-sky scanning. To maximize astrophysical photon detection, the LAT avoids pointing near the Earth by maintaining orientation relative to the zenith (the direction away from Earth), resulting in constant movement relative to the sky. With a 70-degree half-angle field of view ($\sim 2.4\,\mathrm{sr}$), it alternates between the northern and southern hemispheres during each orbit, completing a full sky survey every three hours. Each region receives approximately 30 minutes of observation per cycle, ensuring uniform and comprehensive coverage of the high-energy universe. More technical details about the instrument design and working can be found in [Atwood et al., 2009].

2.1.1 LAT data reduction

Photon events of astrophysical origin identified by the LAT are stored in 'event files', which serve as the primary data source for analysis. Spacecraft position and orientation data, recorded at 30-second intervals, are stored in the 'spacecraft files'. To prevent detector saturation from the intense particle flux in the South Atlantic Anomaly (SAA), the LAT team temporarily disables data collection by lowering the voltage on the photomultiplier tubes (PMTs). These non-detection periods are logged in the spacecraft file. This procedure ensures data integrity but reduces effective observing time by approximately 15%.

Both event and spacecraft files are critical for most analyses and can be downloaded from the *Fermi* Science Support Center[1] (FSSC).

Photon data are analyzed using the *Fermi* ScienceTools package, developed and maintained by NASA. This package runs within the FTOOLS environment, a suite of utilities for creating, examining, and modifying FITS data files. For long-term analysis, the open-source *Fermipy* package is employed. Built on the pyLikelihood interface of the *Fermi* Science Tools, *Fermipy* is a Python-based toolkit offering high-level functions to streamline common analysis tasks for LAT data.

LAT data can be analyzed using two methods: binned and unbinned likelihood analysis. Binned analysis is typically preferred, especially when the source is near a bright background region, such as the galactic plane. In contrast, unbinned analysis is more suitable for point sources where the number of events per bin is low, such as in shorter time periods. We performed binned analysis using the open-source *Fermipy* package. Where necessary, unbinned analysis was performed using *Fermi* ScienceTools.

Due to the LAT's large field of view (FoV), *Fermi* simultaneously observes above 20% of the sky. As a result, data collected for a given source are interspersed with data from many other sources. Instead of considering LAT data as discrete observations of individual sources, it is more accurate to conceptualize the data as a continuous event stream from the mission's start to its end. The frequency of counts from the source of interest depends on the LAT's effective area toward that source at any given time.

[1] https://fermi.gsfc.nasa.gov/ssc/

Initial data cuts are applied to ensure accurate time and positional analysis. To exclude albedo γ-rays from Earth's limb, we implemented a zenith angle cut of 90°. Additionally, a data cut of `(DATA_QUAL>0)&&(LAT_CONFIG==1)` selects intervals when the satellite operated in standard data-taking mode with good data quality. These cuts ensure the LAT instrument was functioning in normal science mode, providing reliable data for analysis.

Fermi-LAT utilizes maximum likelihood optimization to detect sources, measure flux, and derive spectral parameters for specified time ranges and spatial regions. The likelihood function evaluates the probability of the observed data given a model of γ-ray sources, including their intensity and spectra. Accurate likelihood estimation requires proper modeling of the LAT sky, accounting for the target source and nearby sources. While the influence of distant sources is attenuated, it cannot be entirely neglected. While modeling the entire LAT sky ensures accuracy, it is often impractical due to the high computational and time costs involved. For event reconstruction, events are extracted from a circular region of interest (ROI) centered on the target source. The ROI radius should be determined by the density and brightness of surrounding sources and is typically chosen to be several times larger than the LAT's point spread function (PSF). Additionally, a broader source region is defined for modeling, with a radius larger than the ROI to account for surrounding sources. In the model file, spectral parameters for sources within the ROI are allowed to vary, while sources in the surrounding source region are generally fixed to their 4FGL catalog values. Exceptions can be made for particularly bright sources in the source region, which can be left free to improve background modeling. Additionally, galactic diffuse emission (using the model `gll_iem_v07.fits`) and extragalactic isotropic diffuse emission (`iso_P8R3_SOURCE_V3_v1.txt`) are included in the model and allowed to vary. The model file is generated using the user-contributed package

LATSourceModel [2], recommended by the *Fermi*-LAT Collaboration. This package creates an XML file containing information on all nearby sources within the ROI and source region based on the latest *Fermi* catalog.

The significance of the sources detection is determined using the likelihood-ratio test-statistics (TS), which is defined as :

$$\mathrm{TS} = -2\ln(\mathcal{L}_0/\mathcal{L}_1). \tag{2.1}$$

Here, $\mathcal{L}_0$ and $\mathcal{L}_1$ represent the likelihood values for models without (null hypothesis) and with the point source at the position of interest, respectively. The TS is maximized when the likelihood of the model including the source is highest. A higher TS value indicates stronger evidence against the null hypothesis. In general, the detection significance is approximately $\sim \sqrt{TS}$. The specific analysis procedures for each study in this thesis are detailed in the following chapters.

2.2 *Swift*

The launch of the UHRU satellite by the Harvard-Smithsonian group in 1971 marked a significant milestone in the advent of satellite-based X-ray astronomy. This was soon followed by a series of missions such as SAS-3, ANS, and ARIEL 5, which collectively advanced the field. In India, the initial efforts in X-ray astronomy began with balloon-borne experiments conducted between 1966 and 1976, eventually transitioning to satellite-based platforms that revolutionized the exploration of the X-ray universe [Manchanda, 2010].

At present, the X-ray sky is extensively monitored by advanced space-based observatories, including Chandra, NICER, NuSTAR, Swift, and XMM-Newton, each offering unique capabilities for probing high-energy astrophysical phenomena. Among these, Swift has played a particularly versatile role. Launched on November 20, 2004,

[2] https://github.com/physicsranger/make4FGLxml

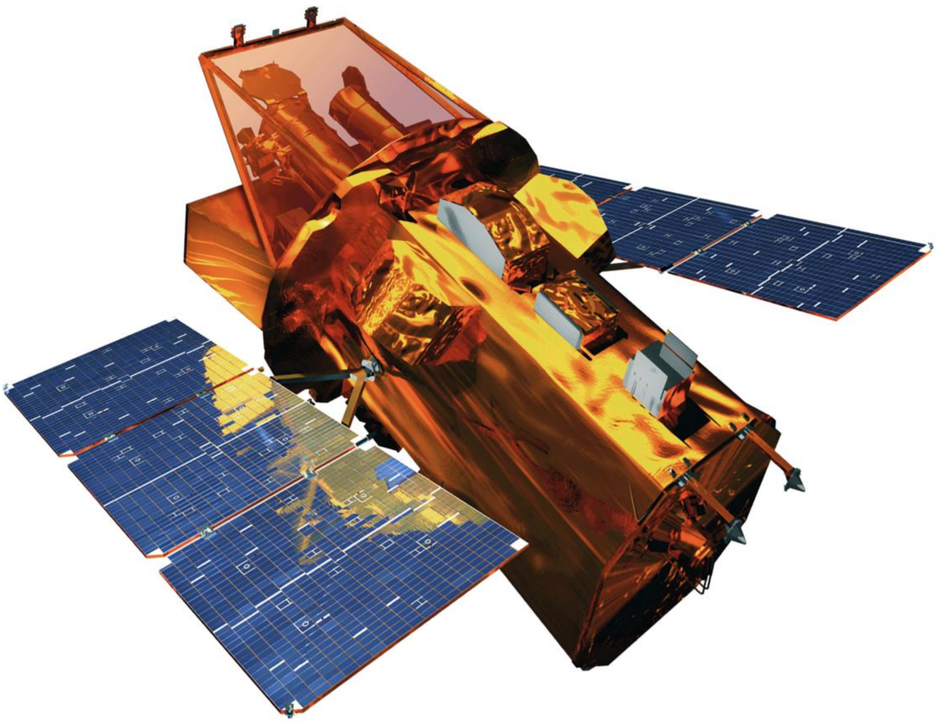

Figure 2.3: *Swift* satellite image [NASA E/PO, 2014]

Swift is a rapid-slewing, multi-wavelength observatory with simultaneous coverage from optical-UV to hard X-ray energies. Designed primarily for GRB observations, *Swift* has also advanced research in other fields, including blazar studies [Ghisellini, 2015]. Its flexible scheduling and target of opportunity (ToO) capabilities allow prompt follow-up of extraordinary events.

Since 2008, joint observations with *Fermi* have enabled broadband studies, enhancing our understanding of high-energy phenomena. All *Swift* data are publicly available, making its archive a valuable resource for future research.

Swift carries three instruments:

1. The Burst Alert Telescope (BAT; Detecting Area: 5200 cm^2, FOV 1.4 sr,

Energy range: $\sim 15 - 150$ KeV) [Barthelmy et al., 2005]

2. The X-ray Telescope (XRT; Effective area $> 125\text{cm}^2$ at 1.5 KeV, FOV 23.6' $\times$ 23.6', Energy range: $\sim 0.2 - 10$ KeV,) [Burrows et al., 2005]

3. The Ultravoilet/Optical Telescope (UVOT; FOV 17' $\times$ 17', $\lambda \sim$ 170-600 nm) [Roming et al., 2005]

The burst alert telescope, the largest instrument on *Swift*, observes approximately one-sixth of the sky at a time. BAT localizes the GRB, and upon identifying the burst direction, pinpoints its location to within 1–4 arcminutes within 20 seconds. The spacecraft then autonomously re-orients to direct the XRT and UVOT at the burst, enabling high-precision X-ray and optical localization and spectral analysis. The XRT operates in pointing mode, while the UVOT captures snapshots during each observation.

In addition to GRBs, it regularly observes other astrophysical events, including blazars. The data are available within 24 hours. XRT and UVOT data are accessible through NASA's HEASARC data portal[3] and are analyzed using the standard analysis procedures specified by the team[4,5]. We have used version 1.0.2 of the calibration database and version 6.29 of the HEASOFT software package.

2.2.1 X-Ray Telescope

The XRT utilizes a Wolter I grazing incidence telescope to focus X-rays onto a thermoelectrically cooled CCD, functioning as a highly sensitive X-ray imaging spectrometer. It is designed to measure fluxes, spectra, and light curves with high timing resolution (≥ 10 ms) across an extensive dynamic flux range spanning over seven orders of magnitude. With an angular resolution of 18", the XRT can precisely lo-

[3] https://heasarc.gsfc.nasa.gov/cgi-bin/W3Browse/w3browse.pl
[4] https://www.swift.ac.uk/analysis/xrt/index.php
[5] https://www.swift.ac.uk/analysis/uvot/index.php

cate GRBs to arcsecond accuracy. Operating autonomously, it dynamically adjusts its readout modes based on the count rate in each CCD frame, ensuring efficient and seamless observation of unpredictable astrophysical events without requiring ground intervention. The readout modes are briefly described here (more details in [Burrows et al., 2005; Hill et al., 2004]):

1. **Imaging Mode (IM)**: In Image Mode, the CCD readout captures positional information and flux estimates without X-ray event recognition based on the accumulated charge. Exposure times of 0.1 s or 2.5 s are automatically selected onboard based on source flux.

2. **Photon diode mode**: This Fast Timing Mode was designed to provide precise timing for extremely bright sources, such as GRBs. In this mode, a high-speed light curve with a time resolution of 0.14 ms is produced, suitable for incident fluxes up to 60 Crabs. However, this mode has been disabled since May 2005.

3. **Windowed Timing (WT) mode**: WT mode of the XRT is designed for observing bright X-ray sources with rapid variability. It offers 1.8 ms timing resolution by collapsing one spatial dimension into a 1D image, allowing it to handle higher count rates (up to 100-300 counts/sec) without pile-up [Romano et al., 2006]. WT mode is ideal for bright GRBs, X-ray binaries, and AGNs where full imaging isn't necessary but high timing accuracy is crucial.

4. **Photon Counting (PC) mode**: PC mode of the XRT offers full imaging and spectroscopic resolution, but time resolution of only 2.5 seconds, suitable for faint sources. It allows precise source localization and imaging but suffers from pile-up for count rates exceeding 0.5 counts/sec.

The standard analysis procedure for XRT analysis is described by the instrument team[6] and is briefed as below: Level 1 archival XRT data were processed using the `xrtpipeline` tool with the `cleanup=no` parameter to generate cleaned event files in both PC and WT modes. To mitigate pile-up effects[7], an annular extraction region was applied, excluding the pile-up-affected core pixels. The inner exclusion radius was determined based on pile-up severity, while the outer radius was fixed at 30 arcseconds. Background regions were selected using a 50-pixel circular region placed away from the source.

For spectral analysis, ancillary response files (ARFs) and redistribution matrix files (RMFs) are required to account for the instrument's effective area, energy resolution, and detector response. ARFs, customized for specific detector positions and extraction radii, are generated using the `xrtmkarf` tool, incorporating calibration files for filter transmission, effective area, PSF, and vignetting. RMFs are retrieved from CALDB. The source spectrum is then combined with the ARF, RMF, and background spectrum using the `grppha` tool.

Spectral analysis was performed in `XSPEC` [Arnaud, 1996], fitting the background-subtracted data with an absorbed power-law model incorporating the `tbabs` photoelectric absorption model. To account for interstellar absorption of soft X-rays, the neutral hydrogen column density (N_H) was fixed to its galactic value [Kalberla et al., 2005].

2.2.2 UVOT

The ultraviolet/optical Telescope aboard *Swift* is co-aligned with the XRT, enabling simultaneous multi-wavelength observations across the optical, UV, and X-ray bands. UVOT features a 30 cm modified Ritchey-Chrétien primary mirror with diffraction-limited performance, covering a wavelength range of 170–600 nm and a FoV of 17 × 17 arcminutes. The instrument includes six broadband fil-

[6] https://www.swift.ac.uk/analysis/xrt/index.php
[7] https://www.swift.ac.uk/analysis/xrt/pileup.php

ters—three for the optical range (V, B, U) and three for the UV range (UVW1, UVM2, UVW2)—along with two grisms for spectroscopy. Observation data were obtained from the HEASARC archive[8]. The data is analyzed using standard analysis procedure[9]. Multiple exposures were combined using the `uvotimsum` tool, and fluxes were extracted with `uvotsource` via aperture photometry. Source counts were extracted using a 5-arcsecond circular aperture centered on the target, while background counts were taken from a nearby source-free region with a radius of 20-arcseconds. Host galaxy flux contributions, based on Raiteri et al. [2013], were subtracted to reduce contamination. Galactic extinction corrections were applied using the $E(B-V)$ value and the extinction law from Cardelli et al. [1989]. Corrected magnitudes were converted to fluxes using the zero points and flux density factors from Poole et al. [2008] and Roming et al. [2008], ensuring accurate flux measurements for analysis.

2.3 Variability Study

Blazars are known for their extreme variability across a wide range of timescales and the entire electromagnetic spectrum. However, the relationship between rapid flux variations and longer-term changes spanning days to years remains a subject of ongoing investigation. This thesis employs various tools to quantify and analyze variability across multiple timescales, aiming to uncover its origin and underlying mechanisms. Some of the tools are described below:

2.3.1 Power Spectrum

In the case of blazars, this temporal variability is often described by power-law noise, where the power spectral density (PSD) provides a quantitative measure of how the variance in the lightcurve is distributed across different temporal frequencies. The

[8] https://heasarc.gsfc.nasa.gov/cgi-bin/W3Browse/w3browse.pl
[9] https://www.swift.ac.uk/analysis/uvot/index.php

PSD is typically proportional to the frequency of the signal raised to a negative power, α, such that α ($P(\nu) \propto \nu^{-\alpha}$) [Isobe et al., 2015]. This indicates that lower frequencies (longer timescales) tend to dominate the variability.

To characterize this behavior, the power spectrum of the lightcurve was calculated, and its best-fit parameters were estimated using the PSRESP (Power Spectral Response) method. This technique, as detailed in Max-Moerbeck et al. [2014] and based on the framework of Uttley et al. [2002], provides a robust statistical approach for modeling the PSD under the assumption of power-law noise. The details of the PSRESP method are outlined below:

2.3.1.1 Measuring the Raw Periodogram

For a uniformly sampled time series $f(t_i)$, recorded at discrete times t_i, with N total data points sampled at a fixed time interval ΔT, the power corresponding to different frequencies present in the signal is determined by the squared modulus of its discrete Fourier transform (DFT):

$$|F(v_k)|^2 = \left[\sum_{n=1}^{N} f(t_i) cos(2\pi v_k t_i)\right]^2 + \left[\sum_{n=1}^{N} f(t_i) sin(2\pi v_k t_i)\right]^2 . \qquad (2.2)$$

The periodogram is normalized to its root mean square (rms) value to produce a normalized power spectrum [Vaughan, 2005], expressed as:

$$P(v_k) = \frac{2\Delta T}{\mu^2 N^2} |F(v_k)|^2 , \qquad (2.3)$$

where squared modulus of the discrete Fourier transform, $|F(\nu_k)|^2$, is calculated after subtracting the mean flux μ from the total flux to reduce the power at the zeroth frequency. The periodogram is sampled at frequencies $\nu_k = k/T$, where $k = 1, 2, 3, \ldots, N/2$ for even N, and $k = 1, 2, \ldots, (N-1)/2$ for odd N. The minimum frequency is given by $\nu_{\min} = 1/T$, and the maximum frequency, known as the Nyquist frequency, is $\nu_{\rm Nyq} = (N/2)(1/T)$. The total duration of the time series is $T = N(t_N - t_1)/(N-1)$.

The normalization factor is chosen such that integrating the power spectrum over the frequency range from ν_1 to the Nyquist frequency $\nu_{\rm Nyq} = N/(2\Delta T)$ corresponds to the fractional RMS squared variability.

Measurement uncertainties introduce additional power across all frequencies. This background noise, arising from statistical fluctuations, is described by [Isobe et al., 2015; Vaughan, 2005]:

$$P_{stat} = \frac{2\Delta T}{\mu^2 N}\sigma_{stat}^2 \tag{2.4}$$

where $\sigma_{\rm stat}^2 = \frac{1}{N}\sum_{j=1}^{N} \Delta f(t_j)^2$ represents the mean variance of the flux uncertainties $\Delta f(t_j)$ in the time series.

Typically time series in astrophysical observation is not uniformly sampled. The Fourier transform of an unevenly sampled time series introduces additional power at higher temporal frequencies in the Fourier domain (see Max-Moerbeck et al. [2014]). To address these effects, we perform linear interpolation between consecutive data points with a period 10 times smaller than the original sampling interval of the observed time series. The periodogram is then calculated using Equation 2.3 for the interpolated, evenly sampled time series. It is subsequently clipped up to the mean Nyquist frequency, given by $1/(2T_{\rm mean})$, where $T_{\rm mean} = (t_k - t_i)/N$. No window function, as recommended by Max-Moerbeck et al. [2014], has been applied in this analysis. The resulting periodogram represents the power spectrum of the observed time series.

The output of Equation 2.3 is referred to as the raw periodogram, which is distributed around the true power spectrum following a chi-square (χ_2^2) distribution with two degrees of freedom. To reduce fluctuations, the power spectrum can be smoothed by averaging it in logarithmic frequency bins with a factor of 1.8 [Isobe et al., 2015]. This binning factor ensures that each bin contains at least two periodogram points, except for the first bin.

The power in each bin is calculated as the average of the logarithms of the powers within that bin, $\overline{\log(P(f))}$, and the corresponding frequency is represented by the geometric mean of the frequencies in the bin [Goyal et al., 2017; Isobe et al., 2015]. The error bars for each frequency bin are given by $0.310/m$, where m is the number of points in the bin [Papadakis & Lawrence, 1993].

At a given frequency f_i, the periodogram value $P(f_i)$ fluctuates randomly around the true power spectrum $P_{\text{true}}(f_i)$ according to a χ_2^2 distribution with two degrees of freedom:

$$P_{f_i} = P_{true}(f_i)\frac{\chi^2}{2} \tag{2.5}$$

The scatter in the periodogram, as described by Equation 2.5, is multiplicative when represented on a linear scale. However, on a log-log scale, this scatter becomes additive.

$$\log[P_{f_i}] = \log[P_{true}(f_i)] + \log[\frac{\chi^2}{2}] \tag{2.6}$$

The expectation value of the periodogram in log-log space does not correspond to the expectation value of the logarithm of the true spectrum. However, the bias remains constant due to the properties of the χ_2^2 distribution in log-log space [Isobe et al., 2015].

$$\Big\langle \log[P_{f_i}] \Big\rangle = \Big\langle \log[P_{\text{true}}(f_i)] \Big\rangle + \Big\langle \log[\frac{\chi^2}{2}] \Big\rangle$$
$$\text{where, } \Big\langle \log[\frac{\chi^2}{2}] \Big\rangle = -0.25068$$

This constant bias is added to the binned periodogram estimates.

2.3.1.2 Estimating the Best fit parameters

Using the raw periodogram, we aim to estimate the best-fit parameters for the binned periodogram. The binned periodogram of the observed lightcurve is compared to a power-law model of the form $P(\nu) \propto 1/\nu^{\alpha}$. To efficiently determine the best-fit parameters, we employ the PSRESP method described in Uttley et al. [2002] and Max-Moerbeck et al. [2014]. This method effectively addresses the challenges posed by red noise leakage and aliasing effects. This has been described in detail in Max-Moerbeck et al. [2014].

Distortion effects arising from sampling and the finite length of the time series cause power transfer to higher frequencies and smearing effects, respectively. To mitigate these issues, we simulate 1000 light curves with flux distributions similar to those of the observed light curves. These simulations are performed using the method described by Emmanoulopoulos et al. [2013]. A key advantage of this method is its ability to preserve the flux distribution of the observed light curve while generating non-Gaussian light curves, a characteristic commonly observed in high-energy blazar light curves. The simulated light curves closely replicate the flux profile of the observed light curve.

To account for red noise leakage, we simulate light curves that are ten times longer than the observed light curve. From these extended simulations, a random segment with the same duration as the observed light curve is selected. To address the aliasing effect, the simulated light curves are sampled using the same temporal sampling pattern as the observed light curve. These steps ensure that the simulated light curves closely replicate the observed light curve while accounting for all potential distortion effects. The log-log raw periodogram for the simulated light curves is then calculated in the same manner as described in Subsection 2.3.1.1 for the observed light curves.

For each sampled frequency, we calculate the mean $\overline{P_{\rm sim}(\nu)}$ and the spread $\overline{\Delta P_{\rm sim}(\nu)}$ of the powers corresponding to the model being tested.

To evaluate the goodness of fit and compare the model against the periodogram of the observed light curve, we compute two parameters, $\chi^2_{\rm obs}$ and $\chi^2_{\rm dist}$, defined as:

$$\chi^2_{\rm obs} = \sum_{\nu=\nu_{\rm min}}^{\nu_{\rm max}} \frac{[\overline{P_{\rm sim}(\nu)} - P_{\rm obs}(\nu)]^2}{\Delta\overline{P_{\rm sim}(\nu)}^2} \tag{2.7}$$

$$\chi^2_{\rm sim,i} = \sum_{\nu=\nu_{\rm min}}^{\nu_{\rm max}} \frac{[\overline{P_{\rm sim}(\nu)} - P_{\rm sim,i}(\nu)]^2}{\Delta\overline{P_{\rm sim}(\nu)}^2} \tag{2.8}$$

Here, $P_{\rm obs}$ and $P_{{\rm sim},i}$ represent the observed and simulated log-binned periodograms, respectively. The fraction of simulated periodograms for which $\chi^2_{{\rm sim},i} > \chi^2_{\rm obs}$ provides the p-value. A higher p-value indicates greater confidence in accepting the model.

This process is repeated for multiple power-law models with α values ranging from 0.1 to 3. The best-fit model is identified as the one with the highest p_α. The uncertainty in the best-fit parameter is determined by fitting a Gaussian to the p_α versus α distribution. The full width half maximum (FWHM) of this distribution provides a 98% confidence interval for the estimated best-fit parameter.

2.3.2 Fractional variability

Fractional variability ($F_{\rm var}$) is a statistical metric used to quantify the variability of a source relative to its mean flux, making it particularly useful for studying the highly variable nature of blazars across multiple timescales and wavelengths, from radio to gamma rays. For a light curve with flux measurements x_i at times t_i, the sample variance is calculated as:

$$S^2 = \frac{1}{N-1}\sum_{i=1}^{N}(x_i - \overline{x})^2; \tag{2.9}$$

where, $\overline{x}$ is the arithmetic mean of the flux. However, real measurements include uncertainties ($\sigma_{\rm err,i}$), which add variance to the data. To account for this, the normalized excess variance is defined as:

$$\sigma^2_{\rm NXS} = \frac{S^2 - \overline{\sigma^2_{err}}}{\overline{x}^2}. \tag{2.10}$$

Here, $\overline{\sigma^2_{\rm err}}$ is the mean square error:

$$\overline{\sigma^2_{\rm err}} = \frac{1}{N}\sum_{i=1}^{N}\sigma^2_{\rm err,i}. \tag{2.11}$$

The square root of the normalized excess variance gives the fractional variability [Edelson et al., 1990; Rodríguez-Pascual et al., 1997]:

$$F_{\rm var} = \sqrt{\frac{S^2 - \overline{\sigma^2_{\rm err}}}{\overline{x}^2}}. \tag{2.12}$$

Fractional variability is often expressed as a percentage, enabling direct comparisons of variability across different energy bands and flux levels. The uncertainty in F_{var}, as described by Poutanen et al. [2008]; Vaughan et al. [2003], is given by:

$$\Delta F_{\rm var} = \sqrt{F^2_{\rm var} + {\rm err}(\sigma^2_{\rm NXS})} - F_{\rm var}. \tag{2.13}$$

where:

$${\rm err}(\sigma^2_{\rm NXS}) = \sqrt{\left(\sqrt{\frac{2}{N}}\cdot\frac{\overline{\sigma^2_{\rm err}}}{\overline{x}^2}\right)^2 + \left(\sqrt{\frac{\overline{\sigma^2_{\rm err}}}{N}}\cdot\frac{2F_{\rm var}}{\overline{x}}\right)^2}. \tag{2.14}$$

In the context of blazars, F_{var} provides a robust method for quantifying and comparing variability across energy bands. This is particularly valuable for understanding the physical mechanisms driving flux changes in blazar jets and the relative contributions of different emission regions and processes. By comparing variability at different wavelengths and activity states, fractional variability helps identify the dominant emission mechanisms and the dynamic interplay between synchrotron and inverse Compton processes in the highly energetic blazar jets.

2.3.3 Bayesian Block and HOP algorithm

To detect and characterize localized variability over time, we use Bayesian Block (BB) representation [Scargle et al., 2013] to model flux points and their uncertainties as step-functions. Each transition in the BB representation corresponds to a 3σ variation from the previous block. To further analyze these variations, the BB output is processed with the HOP algorithm, which is based on a *watershed* approach inspired by topological data analysis [Eisenstein & Hut, 1998].

The HOP algorithm identifies flaring states or high-flux periods by clustering data points from neighboring regions where the flux exceeds a specified threshold. Combined with BB, this method pinpoints peaks by identifying blocks higher than their adjacent ones and then tracing the flux downward in both directions until subsequent blocks fall below the previous one. For this analysis, the mean flux serves as the lower threshold.

This approach segments the light curve into flaring and quiescent epochs, with consecutive BBs above the mean flux baseline grouped into what are referred to as HOP groups. Throughout this thesis, we have used the flare identification code developed by Wagner et al. [2021]. The identified flares are then used for further analysis based on the motivation of the work. This method, as also demonstrated in Meyer et al. [2019], allows for a detailed analysis of flaring epochs across multiple timescales, uncovering evidence of compact emission regions in blazars. Periods with flux levels below the mean are subsequently classified as low-activity states in the following studies.

Chapter 3

Transitioning Blazar BL lacertae : Magnetic reconnection

This chapter is structured based on the paper titled "Flaring activity from magnetic reconnection in BL Lacertae" by Agarwal et al. [2023].

This work focuses on understanding the flaring emission and state transitions in the BL Lac object BL Lacertae during its intense flaring episode from 2020 to 2021. During this period, the gamma-ray flux reached its brightest state, exhibiting sub-hour-scale variability in the gamma-ray band. Minute-scale variability observed during this phase suggests a highly compact emission zone, smaller than the size of the black hole. Alongside this rapid variability, the source displayed a notable state transition from a low-energy-peaked BL Lac to a high-energy-peaked BL Lac, correlated with flux levels.

During these transitions, the X-ray spectrum softened, and the gamma-ray spectral peak shifted to higher energies, indicating a shift of the SED to higher frequencies during enhanced flux states. Conversely, as the gamma-ray flux decreased, the SED transitioned back to lower frequencies. These rapid transitions and variabilities are characteristic of blazars, with shock acceleration models requiring unrealistically high Doppler factors (>100) to explain such behavior. In contrast, jet-in-jet models based on magnetic reconnection offer a more plausible explanation, as they relax the constraints on Doppler factors. In this scenario, the observed transitions may result from the selective alignment of plasmoids along the line of sight.

The state transitions suggest a magnetic field strength of approximately $\sim 0.6\,\mathrm{G}$ within a reconnection region located near the edge of the BLR at a distance of $\sim 0.02\,\mathrm{pc}$. These findings highlight the significance of magnetic reconnection in driving variability and state transitions in blazars.

3.1 About BL lacertae

Bl Lacertae (Bl Lac) is the prototype of the class of blazars known as BL Lac objects. Initially misclassified as a star with an 'identity crisis,' it was discovered by Cuno Hoffmeister in 1929 [Hoffmeister, 1929] due to its rapid variability in intensity, polarization and featureless spectrum [Andrew et al., 1969; Angel & Stockman, 1980]. Subsequent radio observations suggested an extragalactic origin for these variables, indicating their role as defining members of this class [Andrew et al., 1969].

This realization was further supported when Carswell [1975]; Oke & Gunn [1974] identified spectral features indicating a redshift of 0.07, later refined to z=0.0695 ± 0.001 by Miller et al. [1978]. These findings confirmed the presence of weak optical emission lines, anchoring BL Lac's classification as an extragalactic object.

Bl Lac is primarily classified as a LBL object [Nilsson et al., 2018], though it occasionally exhibits IBL to HBL characteristics [Ackermann et al., 2011; Prince, 2021]. Interestingly, despite its BL Lac classification, it shows weak H_α and H_β emission lines, indicating the presence of a faint BLR [Corbett et al., 1996].

The broadband SED of BL Lac is characterized by two distinct humps. The low-energy hump is attributed to synchrotron emission, while the origin of the high-energy hump remains debated, with both leptonic and hadronic models proposed. To address this ambiguity, modeling the multi-wavelength SED of BL Lac during both flaring and quiescent phases suggests that the second hump is primarily driven by γ-ray emission resulting from IC scattering of external seed photons [Abdo et al., 2011]. The BLR likely serves as a source of these seed photons for the electron population in the BL Lac jets. These UV photons from the BLR can absorb and attenuate high-energy γ-rays, leading to a characteristic curvature in the high-energy spectrum [Poutanen & Stern, 2010].

Bl Lac stands out as a recognized TeV emitter, with MAGIC and VERITAS observations detecting very-high-energy (E $>$ 30 GeV) γ-rays characterized by rapid variability [Abeysekara et al., 2018; Arlen et al., 2012; MAGIC Collaboration et al., 2019]. Several mechanisms have been proposed to explain such rapid TeV variability, including:

1. A compact emission zone near the black hole magnetosphere [Aleksić et al., 2014],
2. A mini jet-in-jet scenario caused by magnetic reconnection [Giannios et al., 2009],
3. Jet-star interactions, where the jet collides with a nearby star [Banasiński et al., 2016], and
4. A two-zone emission model, where a small, high-Doppler-factor blob interacts with a larger emission region [Tavecchio et al., 2011].

Building on these theoretical and observational insights, this chapter aims to understand the physical mechanisms driving state transitions and the origins of minute-scale variability in BL Lac during periods of enhanced activity. To achieve these goals, a comprehensive multi-wavelength analysis was performed on four distinct flaring events observed between 2020 and 2021. This analysis spans a broad energy range from optical to γ-ray, ensuring robust broadband coverage through data from space-based facilities, including *Fermi*-LAT, *Swift*-XRT, and *Swift*-UVOT.

The findings reveal a significant state transition in X-rays, where the dominant emission mechanism shifts from synchrotron emission during high states to IC during low states. Simultaneous transitions are also observed in high-energy γ-rays (100 MeV to 300 GeV). The study explores the implications of shocks and magnetic reconnections as possible particle acceleration process driving the spectral shifts and rapid variability. While the Doppler factor inferred in a shock-based scenario appears excessively large for blazar jets, the particle acceleration model involving minijets from magnetic reconnections during flares provides a plausible explanation, easing the constraints on the required bulk Doppler factor.

3.2 Data Acquisition and Analysis

To achieve broadband coverage, we analyzed archival *Fermi*-LAT and identified periods of simultaneous X-ray observations with *Swift*-XRT and *Swift*-UVOT. This approach ensures comprehensive coverage during flaring epochs, allowing us to study temporal and spectral evolution across different flux states. The analysis procedures, detailed in §2.1.1, §2.2.1, and §2.2.2, are summarized here.

3.2.1 *Fermi*-LAT

We analyzed 13 years of *Fermi*-LAT data for BL Lac (MJD 54683–59473) using standard procedures from the *Fermi* Science Tools [Abdo et al., 2009] and the open-source *Fermipy* package [Wood et al., 2017]. The latest instrument response function, `P8R3_SOURCE_V3`, was used to analyze the data, as detailed in §2.1.1.

For data selection, only high-confidence photon events were included by applying a selection cut with `gtselect` using evclass=128. We selected photon events in the

100 MeV to 300 GeV energy range within a 15° radius of the source to accommodate for the broad PSF of the *Fermi*-LAT telescope. To minimize contamination from Earth's albedo, a zenith angle cut of 90° was applied. Further quality refinements were made using `gtmktime` with the filters `DATA_QUAL > 0 && LAT_CONFIG==1` and evtype=3 to ensure high-quality data.

With the high-quality photon dataset prepared, we constructed the spectral model using sources listed in the *Fermi*-LAT fourth source catalog [4FGL-DR3; Abdollahi et al., 2022]. We considered all sources within a 15° radius around BL Lac's position (RA = 330.68°, DEC = 42.2778°). The spectral parameters and normalizations of sources within a 5° circular radius around BL Lac's position and bright sources with TS > 9 were set as free parameters. For sources outside the 5° radius or with TS < 9, the parameters were fixed to their catalog values.

The source spectrum was modeled using a log-parabola function described as :

$$\frac{dN}{dE} = N_{\circ} \left(\frac{E}{E_b} \right)^{-(\alpha + \beta(\log(E/E_b)))} . \tag{3.1}$$

The best-fit parameters were derived using the binned likelihood method [Abdo et al., 2009]. This approach ensures a precise estimation of BL Lac's spectral parameters, minimizing contamination and improving the robustness of the fit.

3.2.2 *Swift*-XRT

For a broad multi-wavelength coverage - including optical, UV and X-ray energies, for BL Lac co-aligned with the high energy γ-ray from *Fermi*-LAT we analyzed publicly available *Swift* archival data from HEASARC[1] database, consisting of 33 pointing observation for the source over four different time periods corresponding to the flaring episodes in high energy *Fermi*-LAT band. BL lac is a known X-ray emitter and is occasionally observed with *Swift*-XRT. Selected time intervals are

[1] https://heasarc.gsfc.nasa.gov/

indicated in the Figure 3.1c. The selected time epochs are as follows: MJD 59120 – 59140, MJD 59329 – 59340, MJD 59400 – 59410, MJD 59420 – 59440.

We used the latest version of the calibration data base (CALDB) and version 6.29 of the HEASOFT software [2] for data reduction. The `xrtpipeline` tool was executed with the parameter `cleanup=no` on level 1 archival files to produce cleaned XRT event files in 'Photon Counting (PC)' and 'Window Timing (WT)' modes. To address pile-up effects[2], an annular extraction region was applied, centering on the source coordinates. Pixels at the core of the image, affected by pile-up, were excluded, with the inner radius determined by the degree of pile-up and an outer radius fixed at 30-arcseconds. Background regions were defined using a circular area of 50 pixels positioned away from the source.

For further spectral analysis, ARFs were generated with `xrtmkarf`, and the appropriate RMF was sourced from CALDB. The source spectrum was then combined with the ARF, RMF, and background spectrum using `grppha` tool.

For spectral modeling, the background-subtracted data were modeled with an absorbed power-law function using the `tbabs` photoelectric absorption model in `XSPEC` [Arnaud, 1996]. The galactic hydrogen column density was fixed at $N_H = 2.70 \times 10^{21}\,\mathrm{cm}^{-2}$, consistent with previous studies by D'Ammando [2021].

3.2.3 *Swift*-UVOT

For a coverage over lower energy synchrotron hump, we utilized simultaneous UV-optical data for BL lac using *Swift*-UVOT during the considered flaring epochs. The photometry procedure is same as described in §2.2.2 and are summarised below.

We utilize simultaneous *Swift*-UVOT observations across six filters to achieve comprehensive optical and UV coverage: V (500–600 nm), B (380–500 nm), U (300–400

[2] https://heasarc.gsfc.nasa.gov/docs/software/heasoft/
[2] https://www.swift.ac.uk/analysis/xrt/pileup.php

nm), W1 (220–400 nm), M2 (200–280 nm), and W2 (180–260 nm). Source counts are extracted from a circular region with a 5-arcseconds radius centered on the source, while background counts are derived from a nearby source-free region with a 20-arcseconds radius [D'Ammando, 2021].

Using the extracted source and background files, magnitudes and fluxes are computed. Flux contributions from the host galaxy, as determined by Raiteri et al. [2013], are subtracted to minimize contamination. Specifically, the host galaxy flux densities in the V, B, U, W1, M2, and W2 bands are 2.89, 1.30, 0.36, 0.026, 0.020, and 0.017, mJy, respectively, accounting for approximately 50% of the total galaxy flux Raiteri et al. [2013]. This host contribution is removed from the observed magnitudes to yield host-free flux values.

Further corrections for galactic extinction are applied using an E(B-V) value of 0.291 [Schlafly & Finkbeiner, 2011] and the galactic extinction law by Cardelli et al. [1989]. The corrected magnitudes are then converted to flux values using zero points and flux density conversion factors provided by Poole et al. [2008] and Roming et al. [2008], ensuring accurate flux measurements for scientific analysis.

3.3 Results

3.3.1 Flare Identification and blazar variability

The 13 years of high-energy flux evolution in *Fermi*-LAT provides a comprehensive view of the underlying jet activity. The flux evolution in 100 MeV - 300 Gev from the direction of BL Lacertae is shown in Figure 3.1. Visual inspection of Fig. 3.1 shows that the high-energy lightcurve of BL lac could be divided into 5 states marked with vertical dashed lines, namely - State 1 (S1; MJD 54683 - 55692), State 2 (S2; MJD 55693 - 56103), State 3 (S3; MJD 56103 - 57003), State 4 (S4; MJD 57003 - 59003), State 5 (S5; MJD 59003 - 59463) based on state of activity and flux levels. Identifying these states is crucial for studying spectral and flux variability across

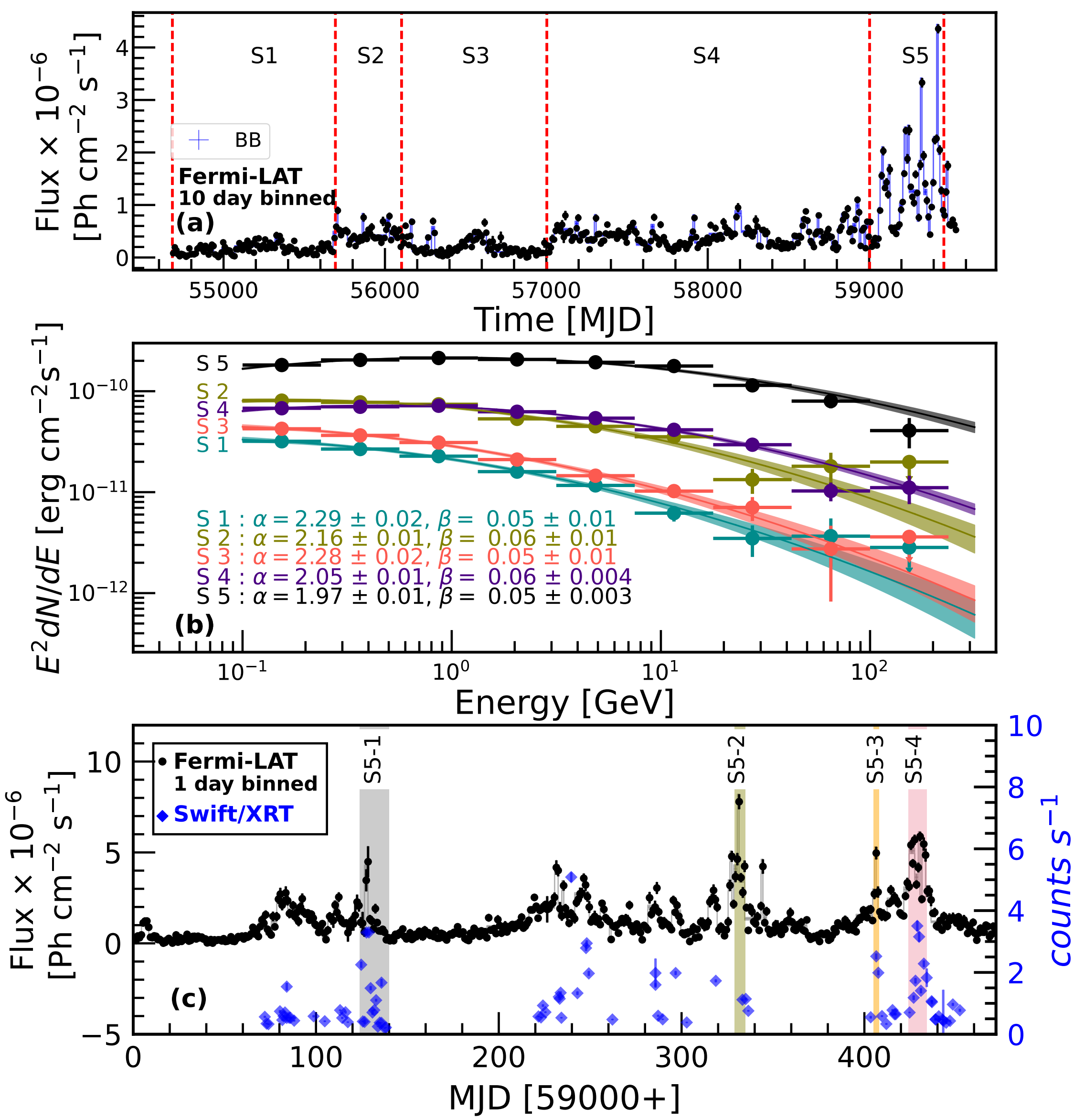

Figure 3.1: (a) The *Fermi*-LAT LCs of BL Lac for MJD 54683-59473. The red lines categorize 13 years of data into 5 flux states (S1-S5).(b) The high-energy (0.1 - 300 GeV) spectrum of the 5 states. (c) The 1 day binned *Fermi*-LAT LC of BL Lac for MJD 59000-59478 (S5). The highlighted regions in grey, olive, orange, and pink represent the periods under study (S5-1, S5-2, S5-3, S5-4). Bayesian blocks on top highlight the variable nature of the LC. *Swift*-XRT overall binned LC for MJD 59000- 59478 is plotted alongwith (in blue).

different flux levels. BB analysis on the 10-day binned light curve is performed as described in §2.3.3. The algorithm identifies 94 change points across the five flux states as shown in Fig. 3.1a. Intrinsic variability across flux states sheds light on jet dynamics driving flux changes. To explore the variability dependence on the flux levels, we studied the PSD of the five identified states. The PSD fitting was performed using the `PSRESP` methods described in §2.3.1. The PSD analysis of the light curve was conducted using various time binning intervals, ranging from 10 days down to 3 hours, utilizing 13 years of *Fermi*-LAT data. The detailed results of this analysis are presented in Table 5.1.

The PSD spectra spanning timescales from 10 days to 3 hours align with pink noise, characterized by a power-law index of approximately 1 in the 0.1–300 GeV range. Interestingly, the PSD behavior remains unaffected by the source's flux state. The consistent pink noise across these timescales suggests a unified variability mechanism driving jet activity, irrespective of the flux levels and timescales. Additionally, we evaluated the fractional variability ($F_{\rm var}$) and its associated uncertainty using the method described in §2.3.2, based on Vaughan et al. [2003]. The source displays larger variability for state S3 and S5 with the values of fractional variability as 0.70 ± 0.03 and 0.64 ± 0.01, respectively (See Table 5.1).

Additionally, we estimated the flux profile for different states using Acciari et al. 2021. For S3 and S5, the flux distribution aligns more closely with a log-normal profile, whereas S1, which lacks significant flares, is better described by a Gaussian distribution. The presence of log-normal flux distributions has been widely reported in other blazars across X-rays to VHE γ-rays (Acciari et al. 2021 and references therein), attributed to variability driven by multiplicative processes, such as those occurring in the accretion disk. However, Scargle [2020] highlights that multiplicative mechanisms in disk are not a prerequisite to reproduce the skewness of the flux and the observed variability. Instead, such correlations and variabilities can also arise from purely additive processes in the jet, as demonstrated for minijets-in-a-jet models discussed in Biteau & Giebels [2012].

3.3.2 Spectral variability

The broadband spectrum offers valuable insights into the particle acceleration mechanisms within the jet. To investigate spectral evolution over 13 years, the high-energy LAT spectra across different states were modeled using a log-parabola function, parametrized as:

$$\frac{dN}{dE} = N_{\circ} \left(\frac{E}{E_b}\right)^{-(\alpha+\beta(log(E/E_b)))} \tag{3.2}$$

where E_b was fixed at 0.7 GeV, as specified in the 4FGL catalog. The best-fit spectral parameters are summarized in Fig. 3.1b. The spectral index (α) exhibits a clear trend of hardening with increasing flux across the five states, while the curvature parameter (β) remains consistent for all states. Notably, the spectral peak shifts toward higher energies during periods of elevated flux, reaching 1 GeV in S5, corresponding to the brightest γ-ray emission.

3.3.3 Spectral and Temporal variability of brightest state - S5

Given that S5 is the brightest state over the 13-years of observation period and exhibits significant variability, a deeper investigation into the origins of its prominent flares is warranted. To explore the broadband spectral evolution, we analyze four specific activity regions within S5:

- S5-1: MJD 59120–59140
- S5-2: MJD 59329–59340
- S5-3: MJD 59400–59410
- S5-4: MJD 59420–59440

These regions, highlighted in Fig. 3.1c, were selected based on the availability of

Table 3.1: Summarizes the flux states an their resulting power spectrum index and Fractional variability.

Flux state	Time period [MJD]	T_{obs} [day]	$N_{TS>9}/N_{tot}$	ΔT_{min} [day]	ΔT_{max} [day]	T_{mean} [day]	$\alpha \pm \alpha_{err}$	p_β	$F_{var} \pm \Delta F_{var}$
State 1 (S1)	54683 – 55692	1010	93/101	10	20	10.89	0.81 ± 0.37	0.80	0.52 ± 0.03
State 2 (S2)	55693 – 56103	410	41/41	10	10	10	0.43 ± 0.66	0.98	0.30 ± 0.02
State 3 (S3)	56103 – 57003	900	83/90	10	30	10.86	1.07 ± 0.52	0.65	0.71 ± 0.03
S1+S2+S3	54683 – 57003	2320	216/231	10	30	10.75	1.17 ± 0.34	0.51	0.69 ± 0.01
State 4 (S4)	57003 – 59003	2000	195/195	10	50	10.26	0.94 ± 0.23	0.36	0.42 ± 0.01
State 5 (S5)	59003 – 59463	460	46/46	10	10	10	1.24 ± 0.62	0.22	0.64 ± 0.01
State 5 (S5)	59000 – 59463	464	447/464	1	4	1.04	1.21 ± 0.21	0.46	0.84 ± 0.01
S5-4	59420 – 59440	10	79/79	0.125	0.25	0.13	0.77 ± 0.34	0.14	0.41 ± 0.02
S1+S2+S3+S4+S5	54683 – 59463	4770	457/472	10	50	10.44	1.24 ± 0.29	0.84	1.04 ± 0.01

Here, we summarize the five flux states along with their resulting power spectra over various binning intervals, ranging from 10 days to 3 hours. The first column lists the flux states, where S1, S2, and S3 have been combined to improve statistics due to the limited number of points in S2 and S3. The second through seventh columns represent: (2) the time epochs of the flaring states in Modified Julian Dates (MJDs), (3) the total number of exposure days, (4) the fraction of data points with TS ¿ 9, (5) the minimum sampling interval in the observed light curve, (6) the maximum sampling interval, and (7) the mean sampling interval—i.e., total observation time divided by the number of data points in that interval. The eighth and ninth columns show the power-law index from the power spectral density (PSD) analysis and the corresponding p-value. The power-law model is considered a poor fit if $p_\beta \leq 0.1$, indicating a rejection confidence greater than 90%. The final column presents the fractional variability and its associated uncertainty, as computed following Vaughan et al. [2003].

dense X-ray data corresponding to different flux states during the γ-ray activity. Notably, S5-2 is included to investigate variability during the period of the brightest gamma-ray emission from the source.

Given the improved photon statistics during the brightest state, S5, we improved the binning from 10 days upto 3h, 6h and 12h for the activity regions in S5. We also examine the available X-ray and optical data corresponding to the selected flaring epochs analyzed in this study. The available *Swift*-XRT X-ray observations are marked in the twin axis in blue in Fig. 3.2 (left).

The variability timescales are evaluated using, $t_{var} = (t_2 - t_1)\frac{\ln 2}{\ln(F_2/F_1)}$, where F_1 and F_2 are the fluxes at time t_1 and t_2 respectively and t_{var} is the flux doubling and halving timescales. In addition to the γ-ray variability, we studied the variability in X-rays based on X-ray lightcurves binned for 10, 15, 20, 25, and 30 s. The fastest flux variation during S5 occurred on 2020 October 6, detected by *Swift*-XRT, showing a variability timescale of $\Delta t_{var} = 7.7 \pm 1.6$ min with a significance of $4.8\,\sigma$. A potential shorter variability of 2.4 ± 0.9 min was also observed with $2.6\,\sigma$ confidence. These rapid flux changes are evident as a new BB in Fig. 3.3b.

Simultaneous flux enhancement was observed in the 0.1–300 GeV range; however, no sub-hour variability was detected in the LAT data, likely due to sensitivity limitations. Notably, an hour-scale variability was identified on 2021 April 27 during S5-2, with a rise time of 78 minutes and a decay time of 46 minutes, as seen in the orbit-binned lightcurve in Fig. 3.3a.

In addition to temporal variability, spectral evolution during the flare, pre-flare and post-flare is studied over the four activity periods utilizing the multi-wavelength data for the epochs of simultaneous X-ray observation by *Swift* and γ-ray observations by *Fermi*-LAT.

Epochs with simultaneous observations from *Swift*-XRT, *Swift*-UVOT, and *Fermi*-

LAT were selected based on BBs overlapping the *Swift* observation period, as indicated by vertical dashed lines in Fig. 3.2. Simultaneous multi-wavelength SEDs are shown on the right side of Fig. 3.2. The X-ray spectrum is fitted using the absorbed power-law model described in §2.2.1.

The source demonstrates a "softer when brighter" trend within the 0.2–10 keV energy range during S5. A notable state change in the X-ray band is highlighted by the transition from hard X-ray emission linked to inverse Compton processes during low flux states to softer X-ray emission driven by synchrotron processes during higher flux states. This transition is further supported by a possible shift in the *Fermi*-LAT spectrum toward higher energies, marked by the apparent peak shift of the second hump and the concurrent detection of the highest energy photons (HEP) during the observed state.

This effect is particularly evident during the flares in S5-1 and S5-4. For S5-1, the X-ray emission lies in the rising part of the IC hump from 2020 October 11 to 2020 October 16, in contrast to the observed soft X-ray emission via synchrotron process from 2020 October 2 to 2020 October 10. During this period, LAT data simultaneously shows a shift in the IC peak. This suggests that as the X-ray spectrum becomes softer, the high-energy (100 MeV - 300 GeV) peak shifts to higher energies. The observed shift in the high-energy peak corresponds to detected highest energy photons ranging from 7.6 GeV to 53.6 GeV. Similarly, for period S5-4, we observe a transition from a soft X-ray emission via synchrotron process during 2021 August 2 to the hard X-ray emission through EC process during 2021 August 12. A possible simultaneous shift is observed in the high-energy spectrum, with its peak transitioning from 0.67 GeV during periods of a hard X-ray spectrum to 1.84 GeV during periods of a softer X-ray spectrum. This shift is further corroborated by the detection of high-energy photons ranging from 71 GeV to 114 GeV during these periods. A similar trend is hinted at in S5-3, marked by the detection of a 172 GeV

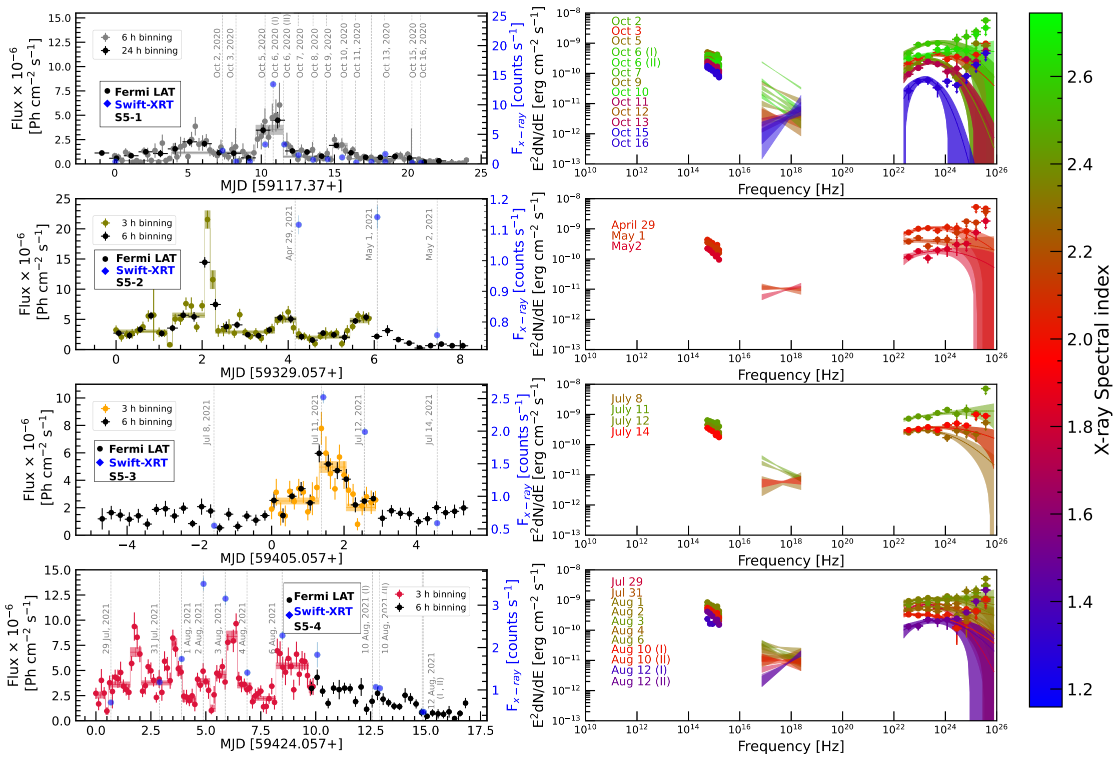

Figure 3.2: (Left) The *Fermi*-LAT LC of periods highlighted in Fig. 3.1c, 3.1d . The *Swift*-XRT LC is plotted on twin axis in blue. Vertical dashed lines represent the times when the MWL SED is studied (right) for the chosen period.

photon on July 11, 2021, when the soft X-ray spectrum aligns with the first hump, compared to a 50 GeV photon on July 14, 2021, during a significantly harder X-ray spectrum. The spectral shift is illustrated in Fig. 3.2.

3.4 Discussion

Bl Lac exhibits flux variability over time, with its high-energy spectrum (0.1–300 GeV) well-described by a log-parabola model. The *Fermi*-LAT spectral index (α) hardens as flux increases, indicating the presence of freshly accelerated or re-energized electrons. The spectrum's curvature parameter (β) remains consistent over 13 years, despite significant flux variations. This stability suggests a similar influence of external UV photons, likely originating within or at the edge of the BLR [Poutanen & Stern, 2010], on the emitted jet photons. The detection of Lyman H_α lines indicates the presence of a weak BLR from the standard scaling relation, such that, luminosity $L_{BLR} = 2.5 \times 10^{42}$ erg/s and $R_{BLR} = 2 \times 10^{16}$ cm [Ghisellini & Tavecchio, 2009].

The source exhibits variability across multiple wavebands [Weaver et al., 2020]. During its high activity period in 2020–2021, several state changes were observed, with X-ray emission transitioning from the second to the first SED hump. For the first time, minute-scale X-ray variability was observed alongside a rare shift of X-ray emission to the first SED hump. Additionally, this rapid variability and X-ray state change were accompanied by a simultaneous shift of the inverse Compton peak to higher energies during activity regions S5-1 and S5-4. Such rare events in blazars provide critical insights into emission mechanisms and particle acceleration models. The brightest γ-ray flux, observed on MJD 59331, revealed sub-hour variability of 46 min in orbit-binned data, consistent with previously reported TeV variability [Arlen et al., 2012]. The flux-rms vs. flux correlation and the prevalence of a log-normal flux distribution suggest a potential multiplicative effect probably linked to the accretion process [Uttley et al., 2005]. Alternatively, these observations could also be explained by a minijet-in-jet model [Biteau & Giebels, 2012]. The similar PSD observed across categorized states points to a consistent variability mechanism in the *Fermi*-LAT band. The combination of quasi-simultaneous TeV emission, rapid variability, peak shifts, X-ray observations at the first SED hump, and a log-normal flux distribution presents significant challenges to the shock-in-jet model [Spada et al., 2001].

3.4.1 Locating the emission region

During the peak X-ray flux, a minimum variability timescale of $\sim$ 8 min was detected in the X-ray light curves with a significance of 4.8σ on MJD 59128. Using the causality relation, the minimum size of the emission region required for the observed variability is given by $R_{emm} < c\Delta t_{var}\delta/(1+z)$ [Rieger, 2019], where Δt_{var} is the minimum variability timescale, z is the redshift, and δ is the Doppler factor. Assuming $\delta = 10$, the emission region size for $\Delta t_{var} \sim 8$min is estimated to be 1.3×10^{14}cm. The location of the emission region, determined using $d_{diss} = 2c\gamma_b^2\,\Delta\,t_{var}$, is constrained to 2.9×10^{15} cm, or approximately 61 r_g from the central engine, assuming the emission region spans the entire cross-section of the jet.

Hints of shorter variability was identified in the 30-second binned *Swift*-XRT light curve, revealing a shorter variability timescale of 2.4 ± 0.9 min (2.6σ), consistent with the findings of D'Ammando [2021]; Sahakyan & Giommi [2022]. Additionally, sub-hour variability of 46 ± 24 min was observed on MJD 59331 during the source's brightest γ-ray state. Pandey & Stalin [2022] also suggesting the presence of minute-scale GeV $\gamma-$ray variability during this intense $\gamma-$ray outburst.

3.4.2 Jet energetics

The extension of the synchrotron spectrum to ∼7.5 keV during high-flux states, coupled with the hardening of the X-ray spectra during low-flux states, suggests either a selective viewing angle during the flare ($\upsilon_{syn} \propto \gamma^2 B\delta$) or a robust particle acceleration process. The detection of 7.5 keV synchrotron photon provides critical evidence of the maximum energy of accelerated electrons.

Using synchrotron cooling timescales, $\tau = \frac{3m_e c}{4\sigma_T \gamma U}$, as described in Eq. 12 of Tammi & Duffy 2009, and frequency of emitted synchrotron photons $\nu_s = 4.2 \times 10^6 \gamma^2 B' \frac{\delta}{1+z}$ Hz [Chatterjee et al., 2021], we constrain $\gamma^2 B'\delta = 4.3 \times 10^{11}$ where $\mathrm{U}=\mathrm{U}_{\mathrm{mag}}=\mathrm{B}'^2/8\pi$ accounts for synchrotron losses.

By translating the observed timescale of 7.7 minutes into the jet frame with a Doppler factor of 5–50, the electron energies driving the 7.5 keV emission are estimated to be $\gamma = 6.5 \times 10^4 - 5.5 \times 10^5$. This constrains the magnetic field strength

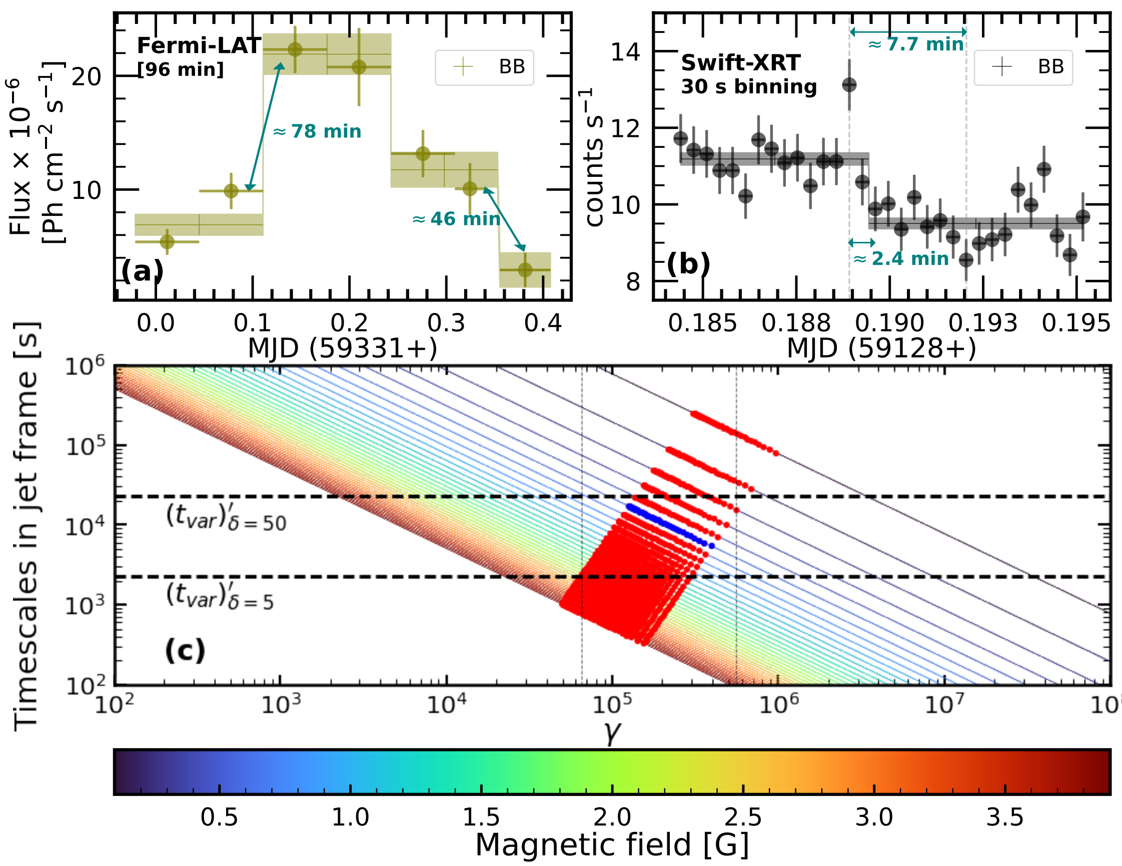

Figure 3.3: (a) Orbit binning LC of BL Lac on April 27, 2021, with BBs with a false positive of 5% plotted on top. The flux doubling timescales at the point of change of the BB is specified. (b) 30 s binned *Swift*-XRT LC for BL Lac corresponding to the brightest X-Ray flux observed on Oct 6, 2020. (c) Synchrotron cooling timescale corresponding to different electron energies. The red point represent the timescale for the observed synchrotron emission upto 7.5 keV. The horizontal black line represents the observed timescales of 7.7 min in jet frame corresponding to Doppler factor between 5-50.

to a range of 0.3–2.2 G, as illustrated in Fig.3.3c.

3.4.3 Shock and Recollimation scenario

In the comoving jet frame, for an emission region corresponding to a variability timescale of ~ 2 minutes and covering the entire jet cross-section, the magnetic energy luminosity at the emission site (with $B' \sim 0.6$ G) is given by $\pi r'^2 c \left(\frac{B'^2}{8\pi}\right)$. This represents the electron luminosity under an equipartition scenario. Assuming 10% of the particle energy ($\eta = 0.1$) is converted into photon energy, the total photon luminosity (L_{ph}) in the observer frame can be expressed as $L_{ph} = \eta \left(\frac{B'^2}{8\pi}\right) \pi r'^2 c \delta^4$ erg/s. For the observed synchrotron luminosity of 8.2×10^{45} erg/s, the required Doppler factor in shock scenario is ~ 125. Additionally, we considered the emission region within the recollimation shock, however the required Doppler factor in such scenario is challenging (~ 100) [Bromberg & Levinson, 2009]. Such high Doppler factors conflict with values derived from kinematic studies of parsec-scale jets ($\sim 5 - 40$) and predictions from magneto-hydrodynamical (MHD) jet models [Jorstad et al., 2005], making this scenario difficult to justify.

3.4.4 Mini-jet in jet model : Magnetic reconnection

Ghisellini & Tavecchio [2008] introduced the needle-in-a-jet model, suggesting that rapid variability could be explained by fast minijets—active regions within a larger jet—that are closely aligned with the observer's line of sight. Building on this concept, Giannios et al. [2009] explored the idea of fast variable emission arising from minijets within a Poynting-flux-dominated jet, driven by magnetic reconnection processes. Narayan & Piran [2012b] further refined these models, incorporating relativistic turbulence to account for both the observed variability timescales and the relative rarity of flaring events, providing a more comprehensive framework for understanding the dynamic processes within jets.

First observational signature for magnetic reconnection was proposed by Giannios [2013] which suggested a fast moving flare on top of a slowly moving envelope. Shukla & Mannheim [2020b] later observed such peak-in-peak variability pattern from structures smaller than the shock yet at a large gravitational radius from central engine. This established magnetic reconnection as a probable model for fast variability in blazar jets.

In this work, the extended synchrotron X-ray emission up to 7.5 keV, coupled with the observed rapid variability and apparent shift into the second hump, could be attributed to the preferred alignment of the emission region along the line of sight, consistent with a jet-in-jet scenario [Meyer et al., 2021; Shukla & Mannheim, 2020a]. Significant energy dissipation occurs when the reconnection timescales match the jet expansion timescales, at distances approximated by $R_{diss} \simeq \Gamma^2 r_g/\varepsilon$. Here, ε represents the reconnection rate [Giannios, 2013], placing the dissipation region at $R_{diss} = 4.74 \times 10^{16}\,\mathrm{cm} = 1012\,\mathrm{r_g}$ from the central engine, near the outer boundary of the BLR. At this reconnection site, magnetic energy is converted into particle energy, leading to the formation of plasmoids [Morris et al., 2019]. Enhanced emission and a shift in the SED to higher energies are expected due to Doppler boosting caused by the selective alignment of a plasmoid along the observer's line of sight. However, as the source returns to a low state post-flare, or when the plasmoid moves out of the line of sight, the Doppler boost diminishes, causing the SED to shift back to lower energies.

Assuming a jet aligned with the line of sight and Γ_j=10, the Doppler factor of a large plasmoid is computed as δ_p=40. Emission from the entire reconnection region produces an envelope emission, significantly weaker than that from mini-jets aligned with the observer's line of sight. The characteristic size, l' , is estimated from the envelope timescale t_{env} as $l' = t_{env}\Gamma_j\varepsilon c \sim 5.1 \times 10^{15}\,\mathrm{cm}$.

The plasmoid responsible for minute-scale flares grows to 10% ($f = 0.1$) of the reconnection region size. The rise/decay time of these flares, superimposed on the envelope emission, is calculated as $t_{flare} = fl'/\delta_p c \sim 425\,\mathrm{s}$.

In the jet-in-jet model, the total luminosities of the envelope and plasmoid, which account for envelope and fast-flare emissions respectively, are expressed as:

$$L_{env} = 2\Gamma_j^2\delta_p^2 l'^2 U_j' \varepsilon c \;\; \mathrm{erg\,s^{-1}} \tag{3.3}$$

$$L_P = 4\pi f^2 l'^2 U''_p c\delta_p^4 \ \mathrm{erg\,s^{-1}} \tag{3.4}$$

where ε is the reconnection rate, U'_j is the energy density in the dissipation zone in the jet's co-moving frame, and U''_p is the energy density of the plasmoid in its co-moving frame [Shukla & Mannheim, 2020a]. Using $U'_j = U''_p/2$ as described in Giannios [2013], the isotropic envelope luminosity is calculated as $L_{env} = 3.6 \times 10^{44}\,\mathrm{erg/s}$, while the plasmoid luminosity is $L_p = 7.2 \times 10^{45}\,\mathrm{erg/s}$ (for $B' = 0.6\,\mathrm{G}$). For this magnetic field strength, the electron energies corresponding to the observed cooling timescales range from lorentz factor $1.2 \times 10^5 - 4 \times 10^5$.

3.5 Summary and conclusion

We conclude that the observed SED variations and variability timescales align with mini-jet in jet from reconnection regions, involving both flaring and steady components. These reconnection regions are located where jet collimation breaks down by instabilities impeding the collimated jet flow. Such current-driven kink or shear-flow instabilities are expected to be triggered outside the BLR, where the powerful winds of accretion disk cannot support the jet collimation. As noted by Jorstad et al. 2022, such instabilities, fuel optical activity and co-spatial γ-ray emission via Synchrotron Self-Compton processes. Closer to BLR, the SED is primarily shaped by inverse-Compton scattering of external optical photons from the BLR [e.g. MAGIC Collaboration et al., 2019]. This work establishes magnetic reconnection as a feasible mechanism for the observed rapid variability and class transitions in the source, possibly occurring beyond the broad-line region (BLR). However, further investigation is needed to explore the exact location of these acceleration sites.

Chapter 4

Imprint of local jet environment : Origin of γ-rays

The chapter has been adopted from the paper titled "Imprint of 'Local Opacity' Effect in $\gamma-$Ray Spectrum of Blazar Jet" by Agarwal et al. [2024]

Relativistic jets from accreting supermassive black holes are powerful $\gamma-$ray emitters, yet the exact mechanisms and sites of energy dissipation responsible for $\gamma-$ray production remain unclear. In the flat-spectrum radio quasar PKS 1424$-$418, we identify an intrinsic absorption feature in the $\gamma-$ray spectrum above 10 GeV during a high-flux state. This feature likely arises from photon - photon pair production involving low-ionization lines near the outer edge of the broad-line region (BLR). Notably, this absorption signature is absent during low$-$flux states, suggesting that $\gamma-$ray emission initially occurs within or at the BLR's edge and subsequently shifts to fainter emission regions beyond the BLR, potentially linked to moving radio knots seen in very long baseline interferometry (VLBI) observations. The inferred $\gamma-$ray emission site aligns with the variability timescale of the brightest flare, supporting an external Compton scattering scenario involving BLR photons.

This chapter outlines the motivation behind the study along with a detailed discussion of the technical methodology and its scientific significance.

4.1 Localizing the gamma-ray emission site

The GeV-range spectra of blazars are shaped not only by non-thermal emission processes within the relativistic jet and also by the immediate jet environment, including the BLR, accretion disk, and torus. Additionally, the EBL contributes to the overall spectral shape. Radiation from the infrared to extreme UV (0.1–100 eV) bands can affect the opacity in the 1-1000 GeV range, leaving characteristic imprints in the spectra. These imprints could provide insights into the localization of the γ-ray emission site.

In particular, these spectral imprints are especially relevant in the study of FSRQs, where the influence of external seed photons plays a dominant role. The observed high Compton dominance in FSRQs suggests a significant contribution of external photons, primarily from the BLR [Ghisellini & Tavecchio, 2009]. These sources typically host massive black holes, enhanced radiative efficiency from accretion disks, and near-Eddington accretion rates, leading to highly luminous disks [Maraschi & Tavecchio, 2003]. Disk radiation reprocessed in the BLR and torus enhances the photon density near the jet base [Ghisellini et al., 2011; Sbarrato et al., 2012]. Consequently, γ-ray photons produced near the black hole on propagating through this dense photon environment, are expected to exhibit a photon-photon pair production cutoff between 10–200 GeV [Liu & Bai, 2006]. Interestingly, the lack of a BLR-induced cutoff in the high-energy spectra of FSRQs challenges this model and suggests that the γ-ray emission region lies beyond the BLR [Costamante et al., 2018]. This interpretation is supported by the detection of TeV photons from FSRQs such as 3C 279 [Aleksić et al., 2011b], PKS 1510−089 [H. E. S. S. Collaboration et al., 2013; MAGIC Collaboration et al., 2018], PKS 1222+216 [Aleksić et al., 2011a], and PKS 1441+25 [Abeysekara et al., 2015]. However, the observed rapid variability and Compton dominance necessitate an emission region located in close proximity to a dense environment of seed photons [H. E. S. S. Collaboration et al., 2013; MAGIC Collaboration et al., 2018]. In contrast to the previous results, Poutanen & Stern [2010] presented evidence of a break in the high-energy spectrum. The idea gains further support from Fermi-LAT observation of 3C 454.3 and 4C +21.35 [Isler et al., 2013; León-Tavares et al., 2013; Stern & Poutanen, 2014; Tanaka et al., 2011]. This constrains the emission site to within the region of influence of the BLR, also supporting multiple observations of rapid variability, which have been proposed to be driven by magnetic reconnection near the BLR [Agarwal et al., 2023; Shukla & Mannheim, 2020a].

In this context, we studied a high-redshift ($z = 1.522$) FSRQ PKS 1424−418 through flux-resolved spectroscopy. The source recently exhibited exceptional outbursts during 2022, reaching 10 times the average flux level. The large black hole mass of $4.5 \times 10^9\, M_\odot$ [Abhir et al., 2021; Fan & Cao, 2004] in PKS 1424−418 provides a possibility of strong accretion rate and thus sufficient seed photons from BLR for the observed Compton dominance ($q \sim 30$; Abhir et al. [2021]). The structure of the chapter is as follows: §4.2 discusses the methods and techniques, §4.3 presents the results, and a discussion is provided in §4.4. Our results are summarized in §4.5.

4.2 Methods and Techniques

4.2.1 Data Resuction : Fermi-LAT

We analyzed approximately ≈15 yr of γ-ray data in the energy range of 0.1−300 GeV to investigate the varying flux states of PKS 1424−418. This dataset was collected by the Large Area Telescope aboard the Fermi Gamma-ray Space Telescope, covering the period from August 4, 2008, to March 21, 2023 [Atwood et al., 2009]. The analysis of the source data in the 0.1–300 GeV energy range was performed using the standard procedures outlined in the Fermi Science Tools documentation[1] and the open-source Fermipy package [Wood et al., 2017].

[1] https://fermi.gsfc.nasa.gov/ssc/data/analysis/documentation/Cicerone/Cicerone_Data_Exploration/Data_preparation.html

The latest instrument response function, `P8R3_SOURCE_V3`, was utilized for this analysis. Photons within 20° of the source location were analyzed to account for the telescope's broad PSF. A zenith angle cut of 90°, a `GTMKTIME` filter with `DATA_QUAL` $>$ 0 && `LAT_CONFIG==1`, and evtype=3 were applied during the analysis. To ensure the selection of high-probability photon events, a `GTSELECT` cut was implemented on the event class, focusing on the `SOURCE` class with `evclass=128`.

Spectral analysis of the dataset was conducted using the Galactic diffuse model `gll_iem_v07` and the isotropic diffuse model `iso_P8R3_SOURCE_V2_v1`. To accurately model photons from the vicinity of the target source, spectral parameters of sources within 10° of the ROI were allowed to vary. Additionally, sources with a variability index greater than 25 within 15° were also allowed to vary. Sources outside 5° of the ROI and with a variability index less than 25 had their spectral parameters fixed to their 4FGL catalog values.

The flux and spectrum of PKS 1424−418 were determined using a log-parabola model, described mathematically as:

$$\frac{dN}{dE} = N_{\circ} \left(\frac{E}{E_b}\right)^{-(\alpha+\beta\log(E/E_b))}. \tag{4.1}$$

Here, the break energy (E_b) was fixed at 677.45 MeV, consistent with the 4FGL catalog [Ballet et al., 2023], while N_o served as the normalization parameter. The spectrum is fitted with the binned `gtlike` algorithm employing the NewMinuit optimizer. A TS value greater than 9 indicated a detection significance exceeding 3σ ($\sqrt{\mathrm{TS}} \sim 3$).

4.2.2 Flare Identification using the Bayesian Block and HOP algorithms

Only periods with significant detections are considered for further analysis. In this study, a time bin in the Fermi-LAT light curve is classified as a detection if it satisfies

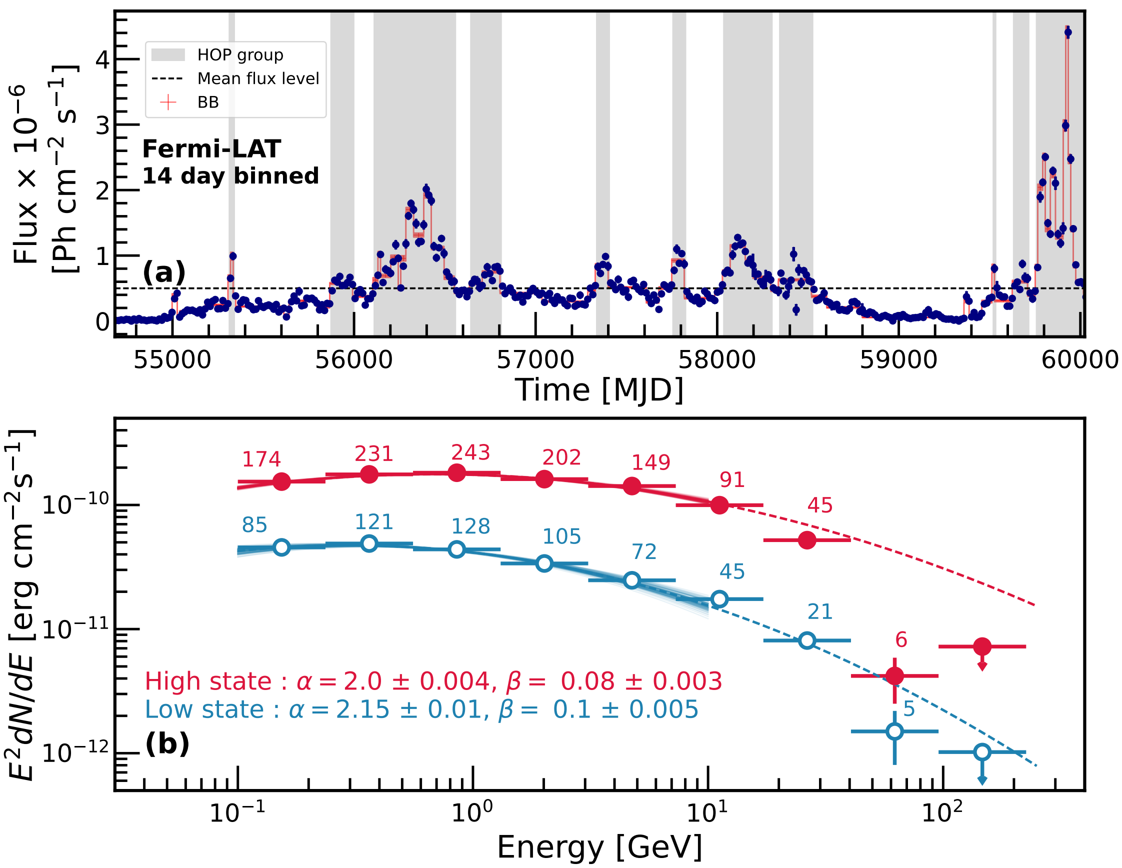

Figure 4.1: (a) The 14-day binned light curve of PKS 1424−418, based on $\approx$ 15 years of Fermi-LAT data. Gray regions indicate high states (flaring periods), while white regions represent low states (quiescent periods). (b) The combined γ−ray spectrum for the flaring and quiescent epochs identified in panel (a). The intrinsic spectrum is modeled with a log−parabola function up to 10 GeV (solid line with shaded uncertainty) and extrapolated to ∼300 GeV (dotted lines). The detection significance ($\sqrt{\mathrm{TS}}$) for each energy bin is shown above the corresponding bins.

TS > 9 and the flux in the bin exceeds its uncertainty, i.e., $F_t > \sigma_t$.

The flux points and their associated uncertainties are represented in a step-function format using the BB method to detect and characterize localized variability structures [Agarwal et al., 2023; Scargle et al., 2013]. Each transition point in the step-function corresponds to a 3σ variation from the previous block.

To identify flaring features in the light curve, the BB output is processed using the

HOP algorithm as described in §2.3.3 for flare identification and grouping. The flare identification code from Wagner et al. [2021] was applied to classify the HOP groups, resulting in 11 HOP flaring groups and 11 quiescent periods, as illustrated in Fig. 4.1(a).

4.2.3 Flux distribution

The flux patterns of the identified HOP flaring groups in PKS 1424−418 are analyzed following the methodologies described by Acciari et al. [2021] and Agarwal et al. [2023]. These flux profiles are subsequently fitted using the following functions:

1. Gaussian:
$$\mathrm{G}(\mathrm{x};\mu_{\mathrm{G}},\sigma_{\mathrm{G}}) = \frac{\mathrm{N_G}}{\sigma_{\mathrm{G}}\sqrt{2\pi}} \exp\left[-\frac{(\mathrm{x}-\mu_{\mathrm{G}})^2}{2\sigma_{\mathrm{G}}^2}\right]. \tag{4.2}$$

2. Lognormal :
$$\mathrm{LN}(\mathrm{x};\mu_{\mathrm{LN}},\sigma_{\mathrm{LN}}) = \frac{\mathrm{N_{LN}}}{\mathrm{x}\sigma_{\mathrm{LN}}\sqrt{2\pi}} \exp\left[-\frac{(\log(\mathrm{x})-\mu_{\mathrm{LN}})^2}{2\sigma_{\mathrm{LN}}^2}\right]. \tag{4.3}$$

Here, N_i, μ_i and σ_i represent the normalization constant, mean, and standard deviation of the fitted profiles, respectively (i= G or LN indicating Gaussian or Lognormal profiles). The preferred distribution fit is selected based on the Akaike Information Criterion (AIC) values [Akaike, 1974], with lower AIC values indicating a better fit to the data.

4.3 Result

4.3.1 Identifying Activity Periods

A comprehensive analysis of the high-energy γ-ray light curve $(0.1 - 300\,\mathrm{GeV})$ over the past 15 years highlights distinct phases of high and low activity. Among these, the 2022 extended flare emerges as a standout event, marked by an intense outburst captured across multiple wavelengths. This multi-wavelength activity included optical observations (ATOM; Jankowsky et al. 2022), radio detections (ATCA; Kadler et al. 2022), and γ-ray emissions recorded by Fermi-LAT and AGILE (La Mura

2022; Verrecchia et al. 2022).

Flaring periods, highlighted by gray-shaded regions in Fig. 4.1(a), alternate with quiescent intervals, depicted as white regions in the same figure. These intervals were identified using the HOP algorithm, as outlined in §4.2.2.

We examine the cumulative high-energy γ-ray spectrum (ranging from 0.1 to 300,GeV) for photons detected during distinct activity phases, categorized as "flaring" and "quiescent" periods. For simplicity, the combined flaring intervals are collectively referred to as the "high state," while the quiescent intervals are designated as the "low state." The γ-ray spectra for these states are characterized using a log-parabola function. We also evaluated the γ-ray spectrum using a power-law model (with spectral index Γ) of the form:

$$\frac{dN}{dE} = N_\circ \left(\frac{E}{E_b}\right)^{-\Gamma}. \tag{4.4}$$

However, the results strongly favored the log-parabola model, as evidenced by TS values of 231 and 151 for the high and low states, respectively, indicating a significantly better fit over a power-law.

For PKS 1424−418, a redshift of $z = 1.522$ implies significant attenuation of γ-ray photons due to interaction with the optical-UV-near-IR EBL, particularly beyond the critical energy $E_{\rm crit} \approx 170(1+z)^{-2.38}\,{\rm GeV} = 18.8\,{\rm GeV}$ [Ackermann et al., 2012]. Poutanen & Stern [2010] first identified a distinct spectral break in bright blazars, attributing it to γ-ray absorption via photon-photon pair production involving helium II (He II) and hydrogen (H) recombination continuum photons. Subsequently, Stern & Poutanen [2014] reported a prominent spectral break near 20 GeV in the source frame, linked to the H Lyman continuum (LyC), based on an improved Pass 7 Fermi-LAT response function. Their findings also showed that spectral breaks associated with He II LyC photons were less significant. Such spectral features in the soft spectrum at energy $E_{\rm soft}$ interact with γ-ray photons at energy $E_{\rm hard}$, resulting in observable attenuation above the threshold energy:

$$E_{\rm th} \gtrsim \frac{(m_e c^2)^2}{E_{\rm soft}(1+z)(1-\cos\,\theta)} \simeq 10 \left(\frac{10\,\rm eV}{E_{\rm soft,Ly\alpha}}\right) \rm GeV \tag{4.5}$$

which is the minimum energy for absorption in a head on collision ($\theta = 180°$). Photons from the BLR can influence the high-energy spectrum only above 10 GeV (see Equation 4.5). As a result, the spectrum below approximately 10 GeV serves as a reliable representation of the source's unabsorbed intrinsic emission. The combined high-energy γ-ray spectra for both high and low states, up to 10 GeV, were modeled using a log-parabola fit (Equation 5.1), yielding consistent β parameters as shown in Fig. 4.1(b). Since attenuation due to the EBL and BLR photons becomes significant only beyond 10 GeV, the observed consistency in β indicates a similar contribution of external seed photons to the emission below this energy threshold.

4.3.2 High energy fast variability

In 2022, PKS 1424−418 experienced extraordinary flaring activity, with its flux soaring to nearly 10 times its $\approx$ 15-year average. On December 20, 2022, Fermi-LAT observed unprecedented rapid variability during the source's most luminous flare. The orbit-binned light curve, with a temporal resolution of ≤ 96 minutes (Fig. 4.2), vividly captures these fluctuations, with the 3σ variation marked by the corresponding BB. Furthermore, during the brightest flux state, Fermi-LAT detected a significant intraday variability of 0.15 $\pm$ 0.06 days, with a statistical significance of $3.8\,\sigma$, as illustrated in Fig. 4.2.

The source exhibits significant variability during its peak activity phase, spanning MJD 59760 to 59961, as evidenced by pink noise behavior extending to timescales as short as 6 hours (power-law index $\approx 1.16 \pm 0.25$; details in Agarwal et al. 2025, in preparation). With a black hole mass of $M_{\rm BH} = 4.5 \times 10^9\,M_\odot$, the minimum variability timescale in the jet frame, based on light-crossing considerations, is approximately ≈ 0.5 days [Spada et al., 2001].

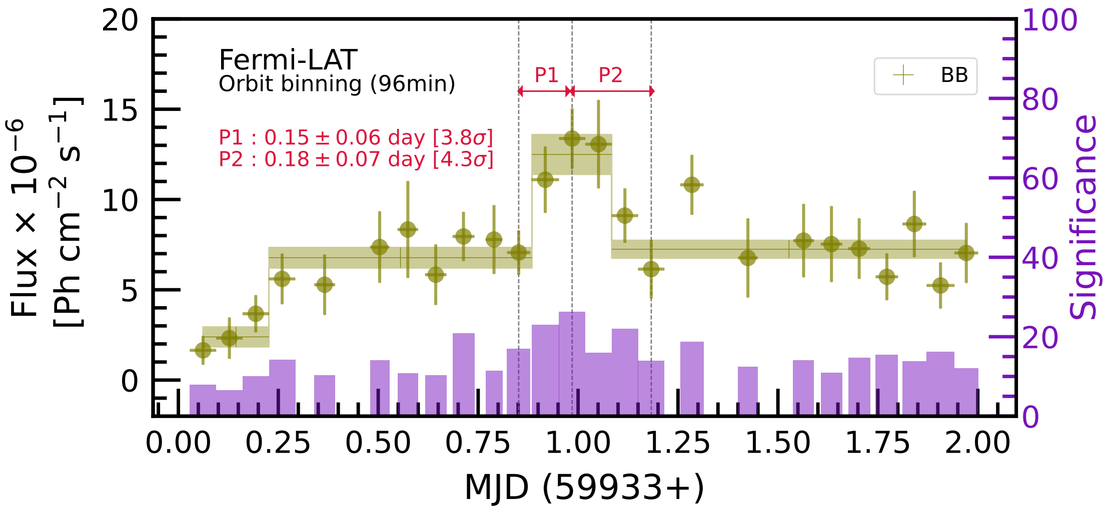

Figure 4.2: The orbit−binned Fermi-LAT light curve reveals the fastest variability periods for PKS 1424−418. Bayesian Blocks, calculated with a 5% false alarm probability, highlight significant flux changes. Grey dotted lines mark key intervals of rapid variability, underscoring significant shifts in the source's emission.

Between MJD 59758 and 60024, the flux of PKS 1424−418 doubled over an observed variability timescale of $(t_{\rm var})_{\rm obs} = 0.15 \pm 0.06$ days, as illustrated in Fig. 4.2. The variability timescales were calculated using $t_{\rm var} = (t_2 - t_1)\frac{\ln 2}{\ln(F_2/F_1)}$ [Foschini et al., 2011], where F_1 and F_2 represent fluxes at times t_1 and t_2, respectively. These exceptionally short timescales impose strict constraints on the size and location of the emission region, which is estimated to be comparable to the size of the black hole itself.

This event represents the fastest variability recorded for this source to date, surpassing the previously reported variability of 3.6 days (4.74 σ) observed during MJD 56015–56020 by Abhir et al. [2021]. The observed variability limits the maximum radius of the emission region to $r'_{\rm emm} = ct_{\rm var}\delta/(1+z) = 1.5 \times 10^{15}(\delta/10)$ cm. For a radiation region of this size, the dissipation distance from the supermassive black hole is estimated as $R_{\rm diss} = 2c\Gamma_j^2 t_{\rm var} = 0.025\,(\delta/10)^2$ pc, assuming the Doppler factor

Table 4.1: Flux distribution parameters for Low- and High-state

State (1)	Model (2)	Mean (μ_i) (3)	Sigma (σ_i) (4)	AIC (5)
High state	Gaussian	3.74 ± 0.01	2.00 ± 0.01	-55999.5
	Lognormal	1.43 ± 0.01	0.57 ± 0.01	-65411.3
Low state	Gaussian	7.36 ± 0.01	4.16 ± 0.01	-47024.6
	Lognormal	2.11 ± 0.01	0.51 ± 0.01	-35417.7

(1) The activity level of the light curves, categorized as either high state or low state. (2) The models applied on the observed flux distribution. (3) The mean value derived from the best-fit model. (4) The standard deviation calculated from the fitted model. (5) The Akaike Information Criterion (AIC) values associated with each fitted model, used to evaluate model performance and suitability.

$\delta = \Gamma_j$ [Rieger, 2019].

If the emission region spans the entire jet cross-section, the 0.025 pc dissipation region likely resides near seed photon sources, such as the BLR or the accretion disk, suggesting their potential influence on the observed variability.

4.3.3 Flux Distribution

The flux patterns in high and low states were analyzed using the flux distribution method detailed in §4.2.3. The Akaike Information Criterion (AIC) results indicate a preference for a log-normal distribution during high states, while low states align better with a Gaussian distribution (refer to Table 4.1).

The log-normal behavior observed during high states suggests the presence of a multiplicative process, commonly associated with accreting galactic sources such as X-ray binaries. This implies a potential influence of the accretion disk on the jet dynamics [Uttley et al., 2005] or the presence of a minijet within the jet structure, as described by Pareto distribution models [Biteau & Giebels, 2012]. This scenario could result from magnetic reconnection processes occurring near the edge of the BLR, as explored in Agarwal et al. [2023].

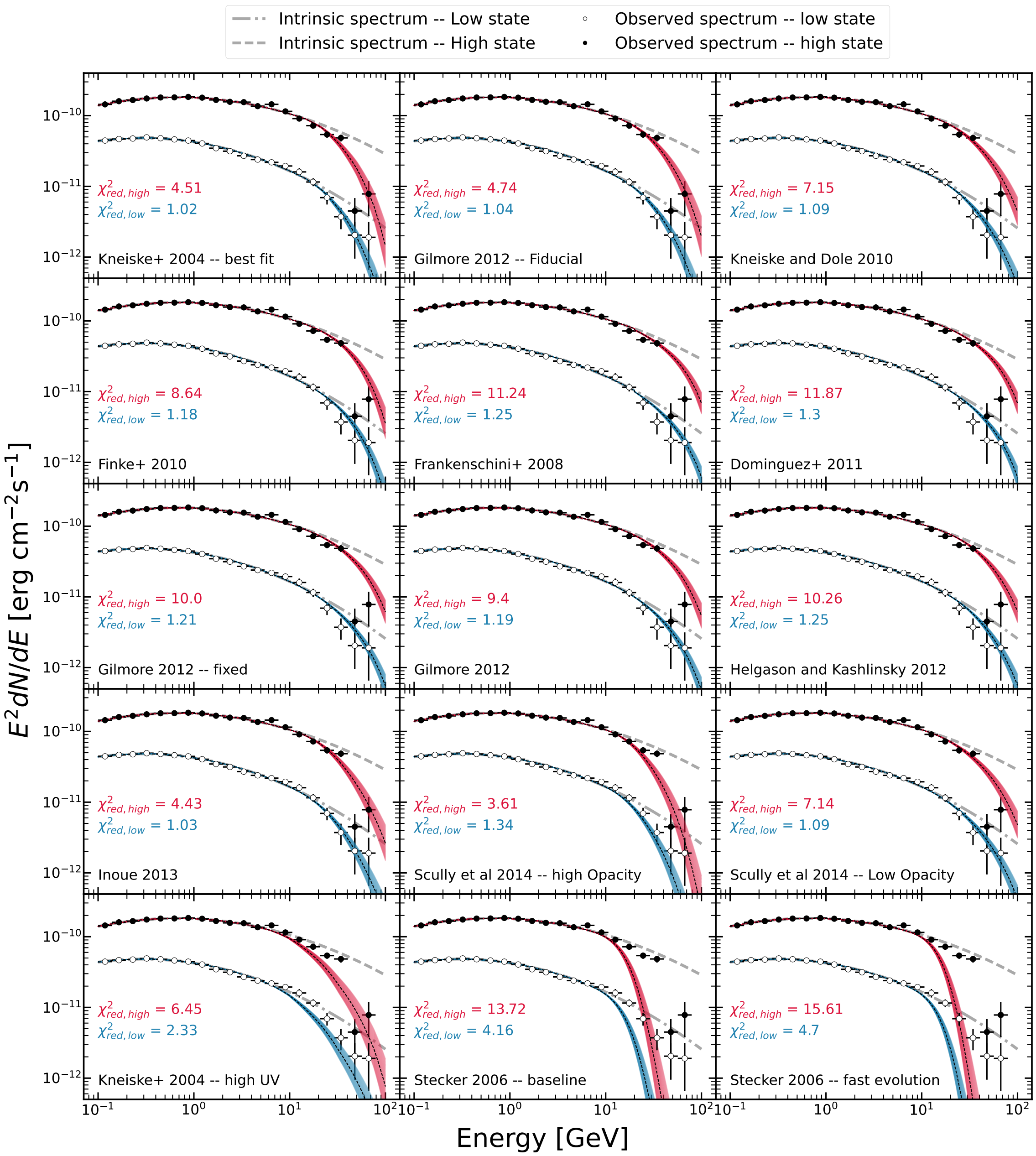

Figure 4.3: The observed γ-ray spectra for both high and low states are displayed across the 0.1−100 GeV energy range. The intrinsic spectra, derived for 0.1−10 GeV and extrapolated up to 100 GeV, are represented by gray dashed lines for the high state and gray dotted-dashed lines for the low state. The solid red and blue envelopes illustrate the EBL-attenuated intrinsic spectra for the high and low states, respectively, incorporating an opacity scaling factor b from 0.75 to 1.25 across the various models specified in each panel. The black dashed lines represent the mean for b=1. Reduced χ^2 values quoted in each panel correspond to the best-fit model at b=1, highlighting the fit quality for the modeled EBL attenuation.

4.3.4 EBL attenuation

The unabsorbed intrinsic spectrum of the source, estimated from $0.1-10$ GeV, is extrapolated to higher energies up to 100 GeV, as shown in Fig. 4.1(b). To evaluate whether the intrinsic spectrum accurately represents the observed spectrum up to 100 GeV, we applied a reduced chi-square (χ^2) test following the methodology of Costamante et al. [2018].

the intrinsic spectrum was strongly rejected with a p-value $< 10^{-5}$ for the high state, while for the low state, the model was rejected with a p-value of $\sim 10^{-4}$. Particularly, the largest contribution to the high χ^2 values originates from the high-energy end of the spectrum ($E > 10$ GeV), as illustrated in Fig. 4.1(b).

The observed spectrum exhibits a significant deviation from the extrapolated intrinsic fit, with a $21.8\,\sigma$ deviation for high-state photons and a $2.8\,\sigma$ deviation for low-state photons in the energy range of $40-95$ GeV. This discrepancy is likely caused by the absorption of γ-ray photons due to interactions with the EBL alone or a combination of EBL photons and soft photons from the local jet environment, such as those from the accretion disk, torus, or BLR, during their propagation to the observer.

To account for EBL absorption, the extrapolated intrinsic spectrum is corrected using an exponential attenuation term, such that $F_{\mathrm{obs}}(E) = F_{\mathrm{int}}(E)\,\exp[-\tau_{\gamma,\gamma}(E,z)]$ [Kneiske et al., 2004], where $\tau_{\gamma,\gamma}(E,z)$ represents the optical depth. Specifically, $\tau_{\gamma,\gamma}(E,z) = b \times \tau_{\gamma,\gamma}^{\mathrm{model}}(E,z)$, with $\tau_{\gamma,\gamma}^{\mathrm{model}}(E,z)$ being the optical depth predicted by various EBL models, and b serving as the opacity scaling factor. The value of b provides insight into the level of EBL absorption:

1. 0: Indicates no EBL attenuation.
2. 1: Confirms the selected model accurately represents EBL absorption, providing a correct estimate of the effect.

To analyze the observed high- and low-state spectra, we compared them against 15 EBL-attenuated spectral models (F_{obs}) with b values ranging from 0.75 to 1.25. This range accounts for a 25% tolerance in optical depths [Ackermann et al., 2012] predicted by models at different energies [Domínguez et al., 2011; Finke et al., 2010; Franceschini et al., 2008; Gilmore et al., 2012; Helgason & Kashlinsky, 2012; Inoue et al., 2013; Kneiske et al., 2004; Kneiske & Dole, 2010; Scully et al., 2014; Stecker et al., 2006].

Among the 15 EBL-attenuated spectra derived from the models mentioned above, 12 showed χ^2 values close to 1 for the low-state spectrum. However, these same models demonstrated significant deviations, with notably high χ^2 values for the high-state spectrum, as illustrated in Fig. 4.3. Since the EBL is uniform and isotropic on large scales, γ-ray absorption caused by photon-photon interactions with EBL photons should be independent of the source flux. Consequently, similar levels of absorption are expected for both high and low states.

However, none of the current EBL models adequately account for the observed absorption levels beyond 10 GeV in the high state using EBL effects alone. The high-state spectrum exhibits additional absorption, likely caused by intervening interacting photons beyond the EBL contribution. Notably, the high-state spectrum deviates from the EBL-absorbed spectra predicted by using the Scully et al. [2014] (high-opacity model) by approximately $\sim 4.7\sigma$ beyond 10 GeV. For the widely used models by Franceschini et al. [2008] and Domínguez et al. [2011], the absorption significance beyond E$>$ 10 GeV exceeds $> 5\sigma$. This indicates the presence of an additional absorption mechanism over EBL absorption influencing the high-state spectrum.

4.4 Discussion

Spectral breaks in the γ-ray spectrum are expected at various energies due to two key factors:

1. **Internal absorption** caused by photon-photon interactions with external seed photons originating from the BLR, accretion disk, and dusty torus.

2. **External absorption** of high-energy photons by the EBL in optical, UV, and near-IR wavelengths.

These absorption mechanisms significantly hinder the detection of high-energy photons in high-redshift sources, compounded by poor photon statistics. Our analysis reveals a pronounced deviation of the stacked high- and low-state spectra from the fitted log-parabola model at energies $E > 10$ GeV, as demonstrated in Fig. 4.1(b).

At energies above 10 GeV, the high state exhibits significant deviations, with two energy bins showing deviations greater than 3σ (Fig. 4.1(b)). In contrast, during the low state, the deviations are much smaller, measured at 0.6σ within the $17-40$ GeV range and 2.8σ within $40-95$ GeV. These deviations are significantly less pronounced compared to the 4σ and 21.8σ deviations observed in the same energy ranges during the high state (Fig. 4.1(b)). This pronounced deviation in the high state reflects the imprint of absorbed high-energy photons, highlighting the significant absorption processes occurring during periods of heightened activity. The observed absorption features in the high state stem from interactions with both the EBL and external jet photons, including those from the BLR, dusty torus, or accretion disk. The prominence of these absorption features during high states is influenced by the location of the emission site within the jet. In contrast, the absence of such absorption in the low state suggests that external photons, apart from the EBL, play a minimal role in shaping the γ-ray spectrum during periods of lower activity.

Low-activity states are typically associated with emission from the outer parsec-scale regions of the jet or are the result of combined emissions along the jet length, without a dominant emission zone. High-activity states, however, are linked to emissions from energetic particles in the inner jet, located within parsec scales of the black hole [Ezhikode et al., 2022]. The high Compton dominance of the source ($q \sim 30$; Abhir et al. 2021) further suggests that accelerated high-energy electrons scatter soft photons, producing γ-rays. This process requires the proximity of high-energy electrons to major soft photon sources, such as the accretion disk, BLR, or dusty torus, emphasizing the dynamic interplay between the jet environment and external photon fields during high states.

The observed variability timescale of 0.15±0.06 days places a lower limit on the emission region's distance from the central black hole, estimated at $R_{\rm diss} > 0.025$ pc. During the 2022 flaring activity, we detected a photon with $E_{\rm HE,max} = 65\,\mathrm{GeV}$, along with approximately 200 photons with $E > 10$ GeV, with over 99% probability of association with PKS 1424−418.

Assuming a flat BLR, the γ-ray emission site is constrained to a minimum distance of $r_{\rm min} = r_{\rm BLR}/\tan\theta_{\rm min} \simeq 0.45\,\mathrm{pc}$ from the central supermassive black hole. We use a BLR radius of $r_{\rm BLR} = 0.5\,\mathrm{pc}$, derived from a disk luminosity of $L_{\rm disk} = 2.5 \times 10^{47}\,\mathrm{erg\,s^{-1}}$ [Abhir et al., 2021; Buson et al., 2014], and the relation $r_{\rm BLR} = 0.1\,\mathrm{pc} \times (L_{\rm disk}/10^{46})^{1/2}$ from Nalewajko et al. [2012].

The minimum collision angle, $\theta_{\rm min}$, at the threshold energy $E_{\rm th} = E_{\rm HE,max}$, is determined using Equation 4.5 as,

$$\theta_{\rm min} = \arccos\left(1 - \frac{2(m_e c^2)^2}{(1+z)E_{\rm HE,max}E_{\rm soft,Ly\alpha}}\right) \simeq 47^\circ. \tag{4.6}$$

At a distance of 0.45 pc, both the BLR and the accretion disk can serve as significant sources of external seed photons. However, if the BLR extends beyond $r > r_{\rm BLR}$, forming a substantial "tail", the high-energy emission is produced at least within the parsec scale.

This observed attenuation is likely influenced by "local opacity" effects caused by interactions with photons from the BLR and accretion disk. To investigate this further, we explore the potential factors contributing to variations in γ-ray opacity within a local jet environment.

4.4.1 Imprint of BLR

The BLR emits several prominent line features due to varying degrees of ionization. Poutanen & Stern [2010] provide a comprehensive synthesis of the most significant features in the BLR spectrum and their impact on the propagation of high-energy photons. Interactions between BLR line photons and jet photons can lead to photon-photon absorption, occurring at the energy threshold for pair production.

The energy threshold for photon-photon pair production depends on both the energy of the soft seed photon and the collision angle, following the relation $E_{\rm th} \propto 1/E_{\rm soft}(1 - \cos\theta)$. Consequently, the angular distribution of external radiation near the emission zone becomes a critical factor. This highlights the importance of BLR geometry and the location of the emission site relative to the BLR in influencing the opacity of γ-ray radiation [Abolmasov & Poutanen, 2017; Lei & Wang, 2014; Tavecchio & Ghisellini, 2012].

When the emission region is located within the BLR at $r = R_{\rm BLR}$, the isotropic distribution of BLR radiation significantly increases the optical depth, leading to enhanced absorption of high-energy photons. However, as the emission region moves toward the outer edge of the BLR, the optical depth declines rapidly. This decrease is due to a transition from head-on collisions ($\theta = 180°$) to less favorable angles ($\theta < 90°$), particularly pronounced near the opacity threshold energy [Abolmasov & Poutanen, 2017; Tavecchio & Ghisellini, 2012].

Spectral breaks on the high-energy spectrum are typically caused by key emission lines, such as hydrogen Lyα (H Lyα) and helium II Lyα (He Lyα), originating near the central engine. Abolmasov & Poutanen [2017] highlighted the additional contributions of various emission lines from larger distances within the BLR, which are predominantly dominated by low-ionization lines.

At $r_{\rm min} = 0.45\,\rm pc$, near the outer edge of the BLR, low-ionization lines become more prominent due to larger collision angles. This contrasts with the smaller collision angles associated with high-ionization lines closer to the inner BLR boundaries. Absorption in the source frame, around $\sim 10 - 30$ GeV, may result from increased γ-ray opacity due to H Lyα and LyC emission lines ($E_{\rm BLR,Ly\alpha} = 10.2$ eV and $E_{\rm BLR,LyC} = 13.6$ eV). While the resulting spectral break could shift to higher energies, the efficiency of photon-photon absorption diminishes as collision angles decrease. The observed absorption in the $100/(1+z)$ - $140/(1+z)$ GeV range cannot be explained by dominant H Lyα and LyC lines within the BLR. Instead, this absorption is likely due to lower-energy Balmer lines such as Hα ($E_{\rm BLR,H\alpha} = 1.89$eV) and H$\beta$ ($E_{\rm BLR,H\beta} = 2.55\,\rm eV$) [Sol et al., 2013]. At the emission site's position of 0.45 pc, near the BLR's outer edge, these low-ionization Balmer lines dominate, contributing to the observed absorption within $40 - 95$ GeV in the observer's frame.

Toward the BLR's flat outer boundary, head-on collisions become less frequent as collision angles are limited to $\theta < 90°$, potentially doubling the break energy [Stern & Poutanen, 2014]. However, if some BLR photons are aligned along the jet axis, facilitating head-on collisions outside the γ-ray emitting region, the observed absorption at $40 - 95$, attributed to $H\alpha$ and $H\beta$, can be justified.

We applied a BLR cutoff to the EBL-absorbed high-state spectrum using the widely adopted EBL model from Franceschini et al. [2008]. The results showed a significant improvement in the fit, with the χ^2 value decreasing from ~ 11.2 to ~ 2.5, and the inferred cutoff energy at 44 GeV. However, the reduced $\chi^2 > 1$ for the BLR cutoff model likely reflects the limitations of using a single exponential cutoff model, which oversimplifies the complex contributions from the BLR's lines and continuum.

4.4.2 Imprints of Accretion disk

The absorption observed beyond 10 GeV suggests that the soft photon energies responsible for this attenuation fall within the range of $E_{\text{soft}} = 1$ to 10 eV. While absorption caused by the EBL would result in consistent attenuation across all flux levels, the enhanced absorption during the flaring state points to a different origin for these optical photons, potentially linked to the accretion disk at the base of the jet. PKS 1424−418 exhibits strong disk emission, which dominates in the optical range [Abhir et al., 2021; Buson et al., 2014], further supporting the idea that the disk may contribute significantly to the observed variability in γ-ray absorption during periods of heightened activity.

The flux distribution in high-energy γ-rays during the high state follows a lognormal pattern, contrasting with the Gaussian distribution observed in the low state. This difference suggests distinct emission mechanisms in the two states. The lognormal distribution during the high state points to the potential influence of disk photons on the jet [Rieger, 2019] or the presence of a minijet within the jet structure, possibly driven by magnetic reconnection at the edge of the BLR [Agarwal et al., 2023; Biteau & Giebels, 2012].

At $r_{\min} = 0.45$ pc, the accretion disk's radiation field, which dominates up to $\approx 10^{17}$ cm ~ 0.03 pc), has a minimal impact on γ-ray opacity. The alignment of soft disk photons with the γ-ray emission from the jet significantly reduces the interaction rates, making the contribution of accretion disk photons to the high-energy spectrum negligible [Abolmasov & Poutanen, 2017]. Additionally, for reasonable Thomson optical depths in the hot intercloud medium, disk photons scattered by free electrons contribute minimally to the optical depth for photon-photon pair production.

However, unabsorbed photons from the accretion disk are subject to further attenuation from BLR photons scattered at larger angles, leading to increased opacity. This indicates that the γ-ray emission site is unlikely to reside within the inner radius of the BLR.

4.5 Summary

In this chapter, we present evidence of significant γ-ray photon absorption at energies above 10 GeV in PKS 1424−418, likely caused by photon-photon pair production involving low-ionization BLR photons originating from the outer edge of the BLR. This absorption signature was observed with high significance during the source's high state.

In contrast, the absence of this absorption feature during the low state suggests that the emission region in this phase is located farther from the BLR. The stark difference between the high- and low-state absorption features supports the hypothesis that intense emission events originating within or near the edge of the BLR transition into faint emission components as the emission site moves beyond the BLR.

This interpretation is further supported by the detection of rapid variability during the high state, consistent with an emission region size of approximately 0.45 pc, placing it within the outer boundaries of the BLR.

Chapter 5

Constraining gamma-ray emission in lensed quasar : PKS 1830−211

The chapter has been adopted from the paper titled Constraining $\gamma-$ray dissipation site in gravitationally lensed quasar - PKS 1830−211 by Agarwal et al. [2025]

Minute-scale variability in γ-ray flares points to extreme particle acceleration regions. However, detecting such rapid variations in high-redshift blazars remains challenging due to current telescope sensitivities. Gravitationally lensed blazars provide a unique opportunity to study γ-ray production zones in distant sources. Time delays between lensed signals offer valuable insights into the spatial distribution of emission regions relative to the lens's mass-weighted center.

In this study, we analyzed one such bright blazar, PKS 1830−211, lensed by an intervening galaxy. Using 15 years of *Fermi*-LAT γ-ray data, we investigated the high-energy flaring emission zones across various flux states. The lensed high-energy light curve is expected to repeat flaring patterns with a specific time lag and demagnification.

To estimate the lensed time delay, we employed a Gaussian Process Regression algorithm along with traditional techniques such as the Autocorrelation Function and Double Power Spectrum. Our analysis consistently revealed a time delay of approximately 20 days across all flaring states, indicating a stable γ-ray emission site likely located within the radio core. Notably, this γ-ray delay is significantly shorter than previously observed radio delays, suggesting that the γ-ray emission zone is closer to the central engine, while the radio emission originates farther out.

The subsequent sections will provide a detailed discussion of the motivation, methodology and key findings from this analysis.

5.1 Lensed delay to resolve distant universe

The detection of extremely rapid γ-ray variability on timescales as short as minutes highlights extreme particle acceleration processes in compact emission zones near supermassive black holes. Such rapid flares in both HE and VHE emissions indicate that the emission region spans only a few tens of gravitational radii from the black hole [Ackermann et al., 2016; Agarwal et al., 2023; Aleksić et al., 2011a; Shukla et al., 2018]. Variable radio emissions on parsec (pc) to megaparsec (Mpc) scales are often correlated with γ-ray activity, suggesting co-spatial origins within the jet [Ghirlanda et al., 2011; Marscher et al., 2008]. However, the absence of rapid variability in the radio band and synchrotron self-absorption at frequencies up to hundreds of GHz limit radio detection in smaller jet structures [Rybicki & Lightman, 1979].

Observations spanning radio to X-ray wavelengths reveal emission regions ranging from subparsec to megaparsec scales [Fuentes et al., 2023; Harris & Krawczynski, 2006; Marscher et al., 2008; Tavecchio et al., 2007]. High-energy telescopes' limited resolution complicates identifying precise γ-ray emission zones, positioning source variability as the key tool for investigating high-energy emission processes and their corresponding production regions. This limitation constrains our understanding of the connection between radio and γ-ray variability [Blandford & Levinson, 1995; Jorstad et al., 2001], particularly in high-redshift blazars, where rapid variability is challenging to detect due to current telescope sensitivities.

However, gravitational lensing offers a complementary perspective on γ-ray emission processes. First predicted by Einstein's general relativity as the deflection of light by the Sun [Einstein, 1936], Zwicky [1937] later proposed that galaxies could act as gravitational lenses. In such systems, photons from a background galaxy are bent by a foreground lensing galaxy, creating magnified and distorted images of the background source. Time-variable sources in lensed systems exhibit similar variability patterns across images, separated by time delays and magnifications. These delays and magnifications are determined by the geometry of the source-lens-observer system.

Time delays and magnifications across different energy ranges provide insights into the size and distribution of emission zones relative to the lens's mass-weighted center [Barnacka et al., 2014]. Analyzing these time delays offers a unique approach to probing the origin of γ-rays in blazars. Long-term monitoring with instruments like *Fermi* enables the study of flux variability over extended periods, revealing the evolution of distant sources. To date, two gravitationally lensed quasars have been detected at γ-ray energies: PKS 1830-211 [Abdo et al., 2015] and QSO B0218+357 [Cheung et al., 2014].

5.1.1 About PKS 1830−211

PKS 1830-211 was first identified as a gravitationally lensed system through observations by the Very Large Array Radio Telescope, revealing two compact components in the northeast and southwest [Subrahmanyan et al., 1990]. Subsequent observations by the Australian Telescope Compact Array (ATCA) demonstrated these components were separated by 0.98" and connected by an elliptical Einstein ring [Jauncey et al., 1991; Nair et al., 1993]. PKS 1830−211, classified as a flat-spectrum radio quasar at a redshift of $z = 2.507$, should appears as a point source but exhibits a double radio structure due to gravitational lensing by an intervening galaxy at $z = 0.89$ [Koopmans & de Bruyn, 2005; Wiklind & Combes, 1996; Winn et al., 2002]. Evidence also indicates a secondary intervening galaxy at $z = 0.19$, identified through H I and OH absorption. However, its lensing effects are likely negligible [Lovell et al., 1996; Muller et al., 2020; Nair et al., 1993; Winn et al., 2002].

Radio time delays were first measured at 8.6 GHz using the ATCA, with a delay of 26^{+4}_{-5} days [Lovell et al., 1998]. Following the launch of *Fermi*-LAT, the first gravitational time delay in γ-rays was observed during the quiescent state of the source, measuring 27.1 ± 0.6 days [Barnacka et al., 2011]. The similarity between radio and γ-ray time delays suggests a co-spatial origin for emissions during low states of γ-ray activity [Barnacka et al., 2014]. Further studies of *Fermi*-LAT data during active states revealed shorter time delays, with 23 ± 0.5 days and 19.7 ± 1.2 days reported [Barnacka et al., 2015]. Additionally, an independent study using molecular absorption lines derived a differential time delay of 24^{+5}_{-4} days, confirming that the northeast component leads the southwest [Wiklind & Combes, 2001].

The detection of time delays in lensed systems depends heavily on the length and quality of the light curve. Understanding the origin of γ-ray flares can be significantly enhanced by analyzing various flaring states at different flux levels. PKS 1830-211 has exhibited substantial activity over the past decade, with multiple flares detected in the *Fermi*-LAT light curve. In this study, we estimated time delays during high-flux flaring periods using methods such as the Autocorrelation Function (ACF) and Double Power Spectrum (DPS). Additionally, we implemented a machine-learning approach—Gaussian Process Regression (GPR)—to estimate time delays across different flux states. A comprehensive 15-year search for time delays was conducted, focusing specifically on the source's active states.

The structure of this chapter is as follows: § 5.2 details the data analysis procedures, the tools and techniques used for time delay estimation. § 5.3 and § 5.4 present the results and an in-depth discussion of the findings, respectively. A summary of the

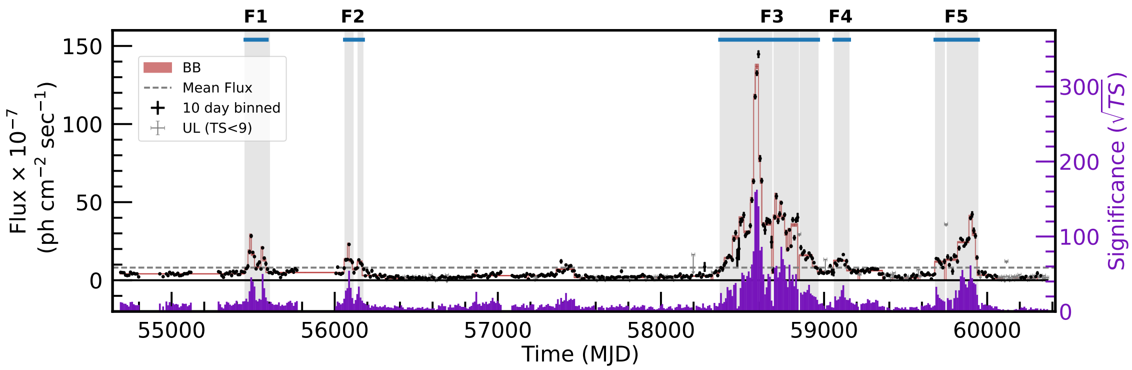

Figure 5.1: 10-day binned light curve of $\approx$ 15.5 years of *Fermi*-LAT observation of gravitationally lensed FSRQ PKS 1830−211. The high-activity states are represented with the grey region, and the white region represents the low-activity state. The light curve is divided into flaring epochs identified using HOP groups, marked by grey patches. HOP groups separated by less than 50 days are combined into flaring states, labeled as F1 to F5 (indicated by horizontal lines). The secondary y-axis (right) shows the detection significance as $\sqrt{\mathrm{TS}}$. Periods with TS < 9 are represented by upper limits.

results is provided in § 5.5.

5.2 Methods and Techniques

5.2.1 Data Reduction - *Fermi*-LAT

Although PKS 1830−211 is a lensed quasar, it appears as a point source at $E >$ 100 MeV due to the spatial resolution limitations of the *Fermi*-LAT telescope. Despite this constraint, *Fermi*-LAT remains a powerful tool, capturing the combined flux from the two lensed images, which have now coalesced into a single signal with a measurable time delay. These time delays serve as a critical probe to constrain the size of the source's emission region.

The *Fermi* Large Area Telescope, a pair-conversion γ-ray detector, is sensitive to photons within the energy range of 20 MeV to 300 GeV [Atwood et al., 2009]. For this study, we analyzed 15.5 years of *Fermi* observations (spanning MJD 54683 to MJD 60373), focusing on a region within 10° of the location of PKS 1830−211.

Positioned approximately 5° from the galactic center, this source is subject to significant contamination from galactic emission. To mitigate this effect, we restricted our analysis to photons in the energy range of 0.2 to 300 GeV.

Photon statistics were extracted using the standard analysis procedures recommended by the *Fermi* Science Tools and the open-source *Fermipy* package [Wood et al., 2017]. The analysis was conducted within the energy range of $0.2 - 300$ GeV, utilizing the latest instrument response function, `P8R3_SOURCE_V3`. To ensure data quality, we applied a zenith angle cut of 90°, a `GTMKTIME` filter with the condition `DATA_QUAL` > 0 && `LAT_CONFIG==1`, and an event type selection of evtype=3. Additionally, only events highly likely to be photons were retained by using a `GTSELECT` filter on event class, specifically selecting `SOURCE` class events with evclass=128.

A source model was constructed by incorporating the target source at RA = 278.413 and Dec = -21.075, along with all 4FGL catalog sources located within 20° of the region of interest. The target source was modeled using a log-parabola function, parameterized as:

$$\frac{dN}{dE} = N_\circ \left(\frac{E}{E_b}\right)^{-(\alpha+\beta(\log(E/E_b)))} \tag{5.1}$$

where scale parameter E_b was fixed at the 4FGL catalog value of 645.56,MeV, with α representing the spectral index, β denoting the curvature parameter, and N_o serving as the normalization. Spectral parameters for sources within 5° of the region of interest were allowed to vary, while those beyond 5° were held fixed at their 4FGL catalog values. The background was modeled using the diffuse galactic emission model (`gll_iem_v07`) and the extragalactic isotropic diffuse emission model for point source analysis (`iso_P8R3_SOURCE_V3_v1`), with both components allowed to vary during the analysis.

A binned likelihood analysis was conducted using `GTLIKE` to determine the best-fit model parameters, including the source's spectral shape and intensity across different epochs. The detection significance was assessed using the TS as described in §2.1.1 . For further analysis, only epochs meeting specific criteria were selected: TS > 9, more than 3 predicted photons, and flux values exceeding their associated uncertainties ($F_t > \sigma_t$).

5.2.2 Analysis Tools and Techniques

5.2.2.1 Bayesian Block and HOP algorithm

To detect and characterize localized variability over time in the lensed lightcurve, we use Bayesian Block and HOP algortihm [Scargle et al., 2013] to model and categorize flux points and their uncertainties as step-functions as described in §2.3.3. The technique allows categorizing the lightcurve into epochs of flaring and quiescent periods.

Using the flare identification code developed by Wagner et al. [2021], nine distinct HOP groups were identified for the lensed source, depicted as gray-shaded regions in Fig. 5.1. According to Barnacka et al. [2015], the maximum time delay between the source and its lensed counterpart is approximately 70 days. Among the nine HOP groups, some occur within intervals shorter than 70 days, indicating potential source-echo flare pairs caused by lensing effects.

To account for these overlaps, HOP groups separated by less than 70 days were consolidated into five flaring states: F1 (MJD 55450–55600), F2 (MJD 56063–56173), F3 (MJD 58363–58963), F4 (MJD 59063–59153), and F5 (MJD 59683–59943), as illustrated in Fig. 5.1. The time delays and magnification effects associated with these flaring states are discussed in detail further.

5.2.2.2 Power Spectrum

To explore the intrinsic temporal properties of the time series, we analyze the PSD of high-energy γ-ray light curves. For stochastic time series, the power distribution at each frequency generally follows a power-law form, expressed as :

$$P(f) \propto f^{-k} \tag{5.2}$$

over range of wavelengths and varying timescales, with the power index k typically ranging from 1 to 3 [Finke & Becker, 2014; Nakagawa & Mori, 2013; Sobolewska et al., 2014]. Studies indicate that the average PSD slope for γ-ray emissions is approximately 1.5 for the brightest flat-spectrum radio quasars and 1.7 for BL Lac objects [Abdo et al., 2010]. During quiescent states, blazars often exhibit pink noise variability, characterized by a power-law slope of ~ 1.

To quantify temporal variability during the observed period, we calculated the power-law variability index for the 1-day and 12-hour binned *Fermi*-LAT LCs corresponding to flares F1–F5 as described in §2.3.1. This analysis employed the `PSRESP` method outlined by Max-Moerbeck et al. [2014] and based on Uttley et al. [2002]. The resulting PSD was modeled using a PL function as described in equation 5.2.

To ensure robust results, we simulated 1000 light curves with flux distributions and statistical variability consistent with the observed LC, following the approach of Connolly [2015]. Additionally, we accounted for red noise leakage and aliasing effects, as described in Goyal et al. [2022], to minimize systematic biases.

5.2.3 Estimating time delay

Gravitational lensing serves as a powerful tool for measuring cosmological distances [Blandford & Narayan, 1992; Refsdal, 1964; Schechter et al., 1997]. Moreover, the time delay and magnification ratio observed at any wavelength provide insights into the location of the emission region relative to the central black hole [Barnacka et al., 2014]. Atwood [2007] anticipated that the LAT instrument could detect delayed emission from bright lensed objects.

High-energy observations of blazars reveal pronounced variability due to their compact emission regions. The lensing-induced delay in photon arrival modifies the

Table 5.1: Summarizes the flux states an their resulting power spectrum index and Fractional variability.

Flux state (1)	Time period [day] (2)	T_{obs} [day] (3)	$N_{TS>9}/N_{tot}$ (4)	ΔT_{min} [day] (5)	ΔT_{max} [day] (6)	T_{mean} [day] (7)	$k \pm k_{err}$ (8)	p_β (9)	$F_{var} \pm \Delta F_{var}$ (10)
F1	MJD 55450 - 55600	150	123/150	1	5.0	1.22	0.91 ± 0.39	0.85	0.66 ± 0.02
			168/360	0.5	5.0	0.77	0.96 ± 0.24	0.60	0.60 ± 0.02
F2	MJD 56063 - 56173	110	101/110	1	3.0	1.08	0.72 ± 0.33	0.05	0.46 ± 0.03
			153/220	0.5	4.0	0.71	1.15 ± 0.24	0.70	0.37 ± 0.03
F3	MJD 58363 - 58963	600	517/600	1	21.0	1.18	1.36 ± 0.24	0.83	0.88 ± 0.01
			941/1200	0.5	21.0	0.64	1.37 ± 0.22	0.54	0.84 ± 0.01
F4	MJD 59063 - 59153	90	75/90	1	4.0	1.19	0.88 ± 0.47	0.14	0.19 ± 0.05
			105/180	0.5	5.0	0.86	0.50 ± 0.27	0.34	0.12 ± 0.08
F5	MJD 59683 - 59943	260	213/260	1	22.0	1.22	1.27 ± 0.37	0.72	0.53 ± 0.02
			355/320	0.5	21.5	0.73	1.23 ± 0.20	0.08	0.45 ± 0.02

Note: (1) Flux states extracted from use of BB and HOP algorithm (2) Period of the flaring states (3) Total exposure time (4) Fraction of points having TS > 9 (5) Minimum sampling time in observed LC (6) Maximum sampling time in observed LC (7) Mean Sampling time i.e. total observation time over a number of data points in that interval (8) The power law index for the power law model of PSD analysis using PSRESP method (9) p-value corresponding to the power law model. The power law model is considered a bad fit if $p_\beta \leq 0.1$ as the rejection confidence for such model is > 90% (10) Fractional variability as described in Section 2.3.2.

intrinsic flux pattern of the source. Unlike radio and optical telescopes, which can resolve multiple magnified images of a lensed source, high-energy observations are constrained by limited spatial resolution. As a result, the composite flux from the source and its echo image appears as a single point source in *Fermi*-LAT data. This creates a repeated flux pattern in the time domain, separated by a time delay of a days and demagnified by a factor of b. The total observed flux is mathematically represented as:

$$S_{\text{obs}} = s(t) + s(t+a)/b. \tag{5.3}$$

The total flux from the two lensed images is integrated into a single combined light curve when observed by high-energy telescopes like *Fermi*-LAT. This introduces a significant challenge: disentangling repeated flares imprinted in the composite light curve, which appears as a point source. Cheung et al. [2014] addressed this issue by separating the flares in the lensed blazar B0218+537, identifying distinct leading and trailing components.

In this study, we employed three techniques to estimate time lags in the data: (1) the autocorrelation function, (2) double power spectrum analysis, and (3) Gaussian process regression. Figure 5.1 illustrates the five identified flaring epochs, which are further analyzed in subsequent sections.

5.2.3.1 Auto-Correlation Function (ACF)

The Autocorrelation Function (ACF) is a widely used statistical tool for assessing the similarity of a time series with its time-delayed copy. By identifying periodicity or repeated patterns within a signal, the ACF is particularly effective for estimating time lags in data.

For noise-dominated signals, variable structures are often embedded within power-law noise, especially with an index greater than 1. Barnacka et al. [2015] highlighted the role of ACF in detecting lags in noisy lensed signals, showing that sources with higher variability indices (k) facilitate easier time-delay detection. In such cases, steep power spectra for a lightcurve with spurious peaks enhance the likelihood of a confident detection.

The statistical significance of the estimated lags was assessed through Monte Carlo simulations, as described further in §5.2.3.4. To handle gaps in the time series, epochs with no or minimal significant observations were interpolated with zeros, following the approach of Barnacka et al. [2015]. We applied the ACF method to 1-day and 12-hour binned time series for flares F1 to F5. The results of this analysis are presented in §5.3.

5.2.3.2 Double Power Spectrum (DPS)

A lensed time series is mathematically described in Equation 5.3. The long, continuous, and evenly spaced nature of *Fermi*-LAT light curves makes it possible to extract time lags using Fourier transform techniques, as outlined by Barnacka et al. [2011], Barnacka [2013], and Barnacka et al. [2015]. This approach was first applied to estimate lags in lensed light curves by Barnacka et al. [2011].

The method involves taking the Fourier transform of the first power spectrum derived from Equation 5.3. Specifically, the Fourier transform of the first component, $s(t)$, is $\tilde{s}(f)$, while the transform of the second component is $\tilde{s}(f)e^{-2\pi ifa}$. Consequently, the observed signal in the frequency domain can be expressed as:

$$\mathscr{F}(S_{\text{obs})} = \tilde{s}(f)(1 + b^{-1}e^{-2\pi ifa}). \tag{5.4}$$

The First Power Spectrum (FPS) is defined as the squared modulus of the Fourier transform of S_{obs}, expressed as:

$$|\tilde{S}(f)|^2 = |\tilde{s}(f)|^2(1 + b^{-2} + 2b^{-1}cos(2\pi fa)) \quad (5.5)$$

An intrinsic lag imprinted on the signal manifests as periodicity in the First Power Spectrum (FPS), with a time period inversely proportional to the lag. Consequently, the power spectrum of the FPS is expected to exhibit a prominent signal corresponding to the time delay. Barnacka et al. [2011] demonstrated that the Double Power Spectrum (DPS) method is 90% efficient at detecting the encoded lag, a significant improvement over the 10% detection efficiency of the Autocorrelation Function (ACF), regardless of the power-law noise index.

To address the smearing effects caused by the finite signal length and sampling limitations, the data must be pre-processed using specific correction techniques. Following the method outlined in Barnacka et al. [2015] and based on Brault & White [1971], we applied an approach capable of accurately extracting time delays from the signal. This method works effectively for light curves dominated by either white noise or red noise and eliminates spurious time delay peaks commonly associated with red noise signals.

5.2.3.3 Gaussian Process Regression (GPR)

A Gaussian Process (GP) is a stochastic process in which any point x in the real domain is associated with a random variable $f(x)$, and the joint distribution of a finite set of these variables follows a multivariate Gaussian distribution. Mathematically, for a set of inputs x_1,x_2,...,x_n with corresponding outputs y_1,y_2,...,y_n, where $y = f(x)$, the function values $f(x)$ collectively exhibit a joint Gaussian distribution. GPs can be considered a generalization of infinite-dimensional multivariate Gaussian distributions. In finite-dimensional cases, correlations between variables are defined by a covariance matrix. In GPs, this matrix is replaced by a “covariance function,” also known as a kernel [Rasmussen, 2004].

To simplify computations, the mean function of the GP is often set to zero. Afterward, the mean of the observational data is added back to ensure predictions align with the original data scale, leveraging the scaling properties of Gaussian distributions. Standardization — subtracting the mean and dividing by the standard deviation of the data before fitting the GP — is a common preprocessing step to enhance computational efficiency and accuracy.

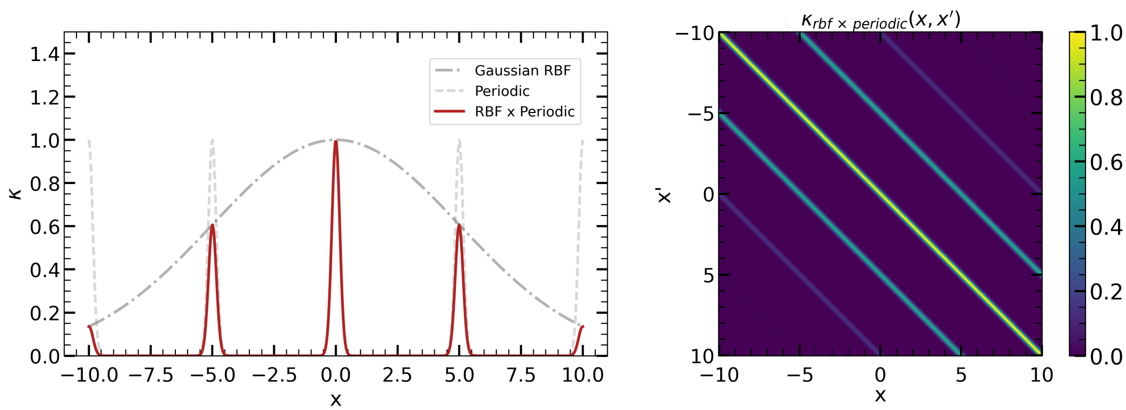

Figure 5.2: (Left) Kernel visualization using covariance between each sample location and zeroth point for RBF, Periodic and RBF × Periodic. (Right) Covariance matrix of the sample space for RBF × Periodic kernel where warmer colors indicate higher correlations.

Kernel selection: Selecting an appropriate kernel requires incorporating prior knowledge about the underlying characteristics of the data. In our analysis, we account for the observed lag effect in the data, which guides us in choosing the following kernel:

$$\kappa(x, x') = \exp\left(-\frac{|x - x'|^2}{2l^2}\right) \times \exp\left(-\frac{2}{l^2}\sin^2\left(\pi\frac{|x - x'|}{p}\right)\right), \tag{5.6}$$

where l represents the length scale, and p denotes the distance between repetitions. The first component of the kernel corresponds to a Gaussian-shaped correlation function, while the second component introduces a periodic correlation structure. The product of these two elements creates a kernel that combines smoothness with periodicity.

As illustrated in Fig. 5.2, the resulting kernel shape reflects this multiplicative structure. Notably, the periodicity parameter p serves as an effective measure of the lag in the data.

Hyper-parameter estimation : The likelihood function serves as an objective function for non-linear optimizing algorithm to obtain the maximum likelihood parameter values. Rather than using the standard likelihood function, GPR employs the log marginal likelihood, which combines a data fit term with a penalty term to prevent overfitting. The log marginal likelihood comprises three components:

- Fit Quality Term:
$$-\frac{1}{2}\mathbf{y}^T(\mathbf{K}(\mathbf{X},\mathbf{X}') + \sigma_n^2\mathbf{I})^{-1}\mathbf{y} \tag{5.7}$$
This term measures how well the model fits the data.

- Penalty Term:
$$-\frac{1}{2}\log\det(\mathbf{K}(\mathbf{X},\mathbf{X}') + \sigma_n^2\mathbf{I}) \tag{5.8}$$
This term discourages overfitting by incorporating the complexity of the covariance matrix.

- Normalization Term:
$$-\frac{n}{2}\log(2\pi) \tag{5.9}$$
This ensures the marginal likelihood represents a valid probability distribution.

Here, $\mathbf{K}(\mathbf{X},\mathbf{X}')$ is the covariance matrix, $\mathbf{I}$ is the identity matrix, and n is the number of data points.

We optimized the kernel hyperparameters using the scikit-learn GPR module [Pedregosa et al., 2011] for computational efficiency. Specifically, we adjusted the length scale hyperparameter for various fixed periodicity hyperparameter values and derived the log marginal likelihood profile over a range of lag values (1–70 days in

1-day steps), as shown in Fig. 5.8. The upper limit of 70 days is informed by prior knowledge of the gravitationally lensed source [Zhang et al., 2008].

To address the challenge of comparing marginal likelihood values that may be very close across different lags, we introduced a "likelihood metric." This metric transforms the marginal likelihood values by multiplying them by -1 and subtracting the maximum value, making it easier to identify the optimal lag. The lag corresponding to the maximum likelihood metric value is selected as the best estimate.

Given the probabilistic nature of this method, the estimated lag is expected to follow a distribution centered on the true lag. The uncertainty in the derived lag is quantified by analyzing the spread of this distribution.

5.2.3.4 Statistical significance

To determine whether the observed time delay is intrinsic to the signal or a result of random fluctuations, we assessed the significance of spurious peaks in the Autocorrelation Function (ACF) and Double Power Spectrum (DPS).

Using the method described by Emmanoulopoulos et al. [2013], we simulated 10^5 artificial light curves that replicate the flux distribution and temporal variability of the observed light curve. This approach addresses a key limitation of earlier techniques [Timmer & König, 1995] by enabling the generation of non-Gaussian distributions. Given that high-energy γ-ray light curves of blazars typically follow a log-normal flux distribution [Bhatta, 2021; Romoli et al., 2018], the simulated light curves exhibit statistical properties identical to those of the observed data.

To enhance realism, data gaps identical to those in the observed light curve were incorporated into the simulations and interpolated with zeros. This ensured that the ACF and DPS of the simulated data were subject to the same observational effects as the original signal.

For each time delay, we constructed cumulative probability distributions of the derived powers and assessed their significance at levels of 1σ, 2σ, 3σ, 4σ. Time delays associated with significant powers ($> 3\sigma$) were classified as intrinsic time delays, distinguishing them from spurious peaks caused by noise or random variability.

5.3 Results

The high-energy (HE) light curve of PKS 1830-211 appear quite complex, characterized by multiple flaring periods interspersed with quiescent states. Figure 5.1 illustrates significant variability in the 10-day binned high-energy flux (200 MeV–300 GeV) over time. This variability is highlighted by fluctuating flux levels, with certain periods exhibiting higher fractional variability compared to others (see Table 5.1).

The flaring periods predominantly display pink noise behavior, with a PSD power-law index close to 1. Interestingly, a transition from pink to red noise behavior is observed during the brightest flux state of the source, identified as F3 in this study (Table 5.1).

These flaring states provide critical insights into the dominant emission zones of the lensed blazar. Such zones are expected to manifest as twin flare pairs separated by a characteristic time interval. The flaring epochs, defined as periods where the flux exceeds the mean level, were identified using BBs, represented by gray patches in Fig. 5.1. BBs separated by less than 70 days were merged, resulting in five distinct flaring states labeled F1, F2, F3, F4, and F5.

The flaring periods, with the exception of F4, exhibit consistent α parameters in the high-energy *Fermi*-LAT spectrum, indicating a uniform physical process within a 3σ range. Moreover, the β values across all flaring periods show remarkable consistency, suggesting a similar contribution from external seed photons to the production of high-energy γ-rays. A detailed summary of the spectral parameters for the flaring periods F1–F5 is provided in Table 5.2.

Flare state	$\alpha \pm \delta\alpha$	$\beta \pm \delta\beta$
F1	2.39 ± 0.03	0.16 ± 0.02
F2	2.29 ± 0.03	0.10 ± 0.02
F3	2.38 ± 0.01	0.15 ± 0.01
F4	2.55 ± 0.04	0.13 ± 0.04
F5	2.41 ± 0.02	0.14 ± 0.02
Quiet state	2.47 ± 0.02	0.08 ± 0.01

Table 5.2: *Fermi*-LAT Spectral parameters for the chosen flaring states and the quiet state. The parameters are derived from the fitted log-parabola model.

The time lag between counterpart flares from lensed images is estimated using the three methods outlined in §5.2.3. The maximum time delay between the lensed images can be expressed as:

$$\sim 6 \left(\frac{z_g}{0.1}\right) (2h)^{-1} \,\text{days} \tag{5.10}$$

where z_g is the redshift of the lensing galaxy, and h is the Hubble constant in units of 100 $\mathrm{km\,s^{-1}\,Mpc^{-1}}$ [Zhang et al., 2008]. Using redshift of $z_g = 0.89$ and $h = 75\,\mathrm{km\,s^{-1}\,Mpc^{-1}}$, the maximum time lag is calculated to be approximately 71 days. This represents the maximum delay between mirage images when the source is near the Einstein ring. For larger time delays, the magnification ratio between the lensed images becomes significant. Consequently, detecting large delays is less likely, as the trailing component would be demagnified beyond the sensitivity threshold of *Fermi*-LAT. Moreover, to effectively explore the full range of potential time delays, the lightcurve must be at least twice as long as the longest expected time delay.

Detecting the trailing counterpart of a lensed blazar during quiescent states is inherently challenging due to its expected demagnification, which often falls below detection thresholds. However, the sensitivity of *Fermi*-LAT enables the identification of multiple flaring states (F1 to F5). During flaring epochs, dominant pink noise introduces spurious peaks, increasing the likelihood of detecting both the leading

Flare	Lag_{ACF}	Lag_{DPS}	Lag_{GPR}
F1	-	17±1.5 ($> 3\sigma$)	19.0±1.5
F2	20.3±2.3	20.0±0.5 ($\sim 2\sigma$)	22.1±2.6
F3	20.5±1.0	21.0 ± 0.5 ($\sim 3\sigma$)	21.1±1.2
F4	-	14.0±0.5 ($< 2\sigma$)	22.4±2.2
F5	-	17.0±0.5 ($> 2\sigma$)	19.4±2.7

Table 5.3: Estimated lags for flares F1, F2, F3, F4, F5 using the three methods (a) Autocorrelation Function (b) Double Power Spectrum (c) Gaussian Process regression

and trailing components.

The source exhibits the highest variability during F3 and F1, with respective fractional variability values [F_{var}; Vaughan et al., 2003] of 0.88 ± 0.01 and 0.66 ± 0.02 (see Table 5.1). Our objective is to determine time delays for flares with sufficient magnification factors to ensure that the demagnified flare remains distinguishable above the baseline flux levels. When feasible, pairs of leading and trailing flares within the identified time lag are selected for analysis to study the spectral properties of the source and its echo flare, as well as the relationship between lag and magnification.

To investigate the variability properties of these flares, we fitted an exponential model to the sharp, distinct features in the light curve using the functional form:

$$F(t) = F_0 \times \left[\exp\left(\frac{t_o - t}{\tau_{\text{rise}}}\right) + \exp\left(\frac{t - t_o}{\tau_{\text{decay}}}\right) \right] \tag{5.11}$$

Here, τ_{rise} and τ_{decay} denote the rise and decay timescales of the flare, respectively. The parameter t_o represents the time of the flare's peak, while F_0 corresponds to half the peak flux at t_o.

5.3.1 Flare F1 - MJD 55453 - 55583

The 1-day and 12-hour binned light curve for flare F1 is shown in Fig. 5.3(a). This flaring period spans 150 days, with 18% of the flux points not resulting in significant detections. Two prominent features are observed in the γ-ray light curve: a sharp peak from MJD 55483 to MJD 55488 and another distinct peak from MJD 55553 to MJD 55573.

The light curve demonstrates pronounced pink noise behavior, characterized by a power-law index of $k = 0.91 \pm 0.39$. To assess the significance of time delays, Monte Carlo simulations were performed, generating synthetic light curves with similar power spectral density indices. While the ACF did not yield a significant detection, a feature at 55 ± 2 days ($\sim 2\sigma$) was identified, likely an artifact associated with the *Fermi* spacecraft's precession period of 53.4 days (Fig. 5.3(b)).

According to [Barnacka et al., 2015], the DPS method significantly enhances the likelihood of detecting time delays, achieving up to 90% accuracy compared to only 10% with the ACF method. In our study, we found the DPS method to be consistently more sensitive, identifying a time delay of 17 ± 1.5 days with a significance exceeding 3σ, as illustrated in Fig. 5.3(c). Similarly, GPR analysis on the 1-day binned light curve revealed a maximum marginal likelihood metric at 19.0 ± 1.5 days. The corresponding GPR best-fit light curve is shown in Fig. 5.8(a). Additionally, a marginal likelihood peak at 9.8 ± 2.9 days may represent a lower harmonic of the 19.0 ± 1.5 day delay, consistent with the periodic nature of the chosen kernel. These findings align with prior studies, such as a lag of 19 ± 1 days reported by Abdo et al. [2015] and 17.9 ± 7.1 days by Barnacka et al. [2015] using ACF.

The primary flare at MJD 55483–55488 and the resulting echo flare (F11 in Fig. 5.9(a)) observed after 20.0 ± 1.1 days provide a proxy for calculating the magnification ratio, yielding an estimated ratio of $\sim$2.8. Similarly, the feature at MJD

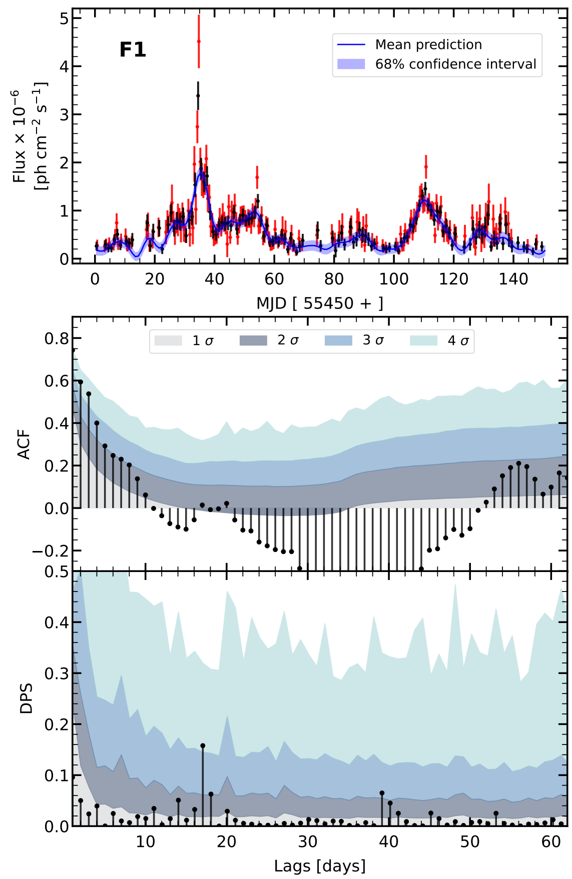

Figure 5.3: (Top panel) 1-day binned (black) and 12hr binned (red) light curve of flaring epochs F1 [MJD 55453 - 55583] (marked in Figure. 5.1) of FSRQ PKS 1830−211. In blue is the GPR predictions on 1 day binned data with largest marginal likelihood. (Middle panel) ACF on 1-day binned light curve of F1 period. (Bottom panel) DPS on 1-day binned light curve.

55553–55573 (F12), assuming a comparable time delay, suggests a magnification ratio of ∼1.6, as illustrated in Fig. 5.9(a).

5.3.2 Flare F2 - MJD 56063 - 56173

Figure 5.4(a) presents the 1-day and 12-hour binned light curves for flare F2. This flaring period remains above the mean flux level, with the preceding and following epochs significantly below the mean. Spanning 110 days, the light curve exhibits pink noise characteristics, with a power-law index of $k = 0.72 \pm 0.33$. Simulated light curves with similar indices were generated to evaluate the significance of the observed lag in the signal.

The ACF for flare F2, shown in Fig. 5.4(b), reveals two features with significance close to 2σ, corresponding to lags of 11.0 ± 2.3 days and 20.3 ± 0.5 days, consistent with findings by Barnacka et al. [2015]. Additionally, a lag of 55.7 ± 2.2 days appears with 2σ significance in both the 1-day and 12 hour binned light curves, likely an artifact of the *Fermi* telescope's 53.4-day processing period, similar to flare F1.

The DPS method applied to the 1-day binned light curve detected a time delay of 20 ± 0.5 days with more than 2σ significance (Fig. 5.4(c)). GPR analysis corroborated these findings, identifying increased marginal likelihood metrics at 13.3 ± 4.3 and 22.1 ± 2.6 days, aligning with the ACF results. The likelihood distribution for GPR on flare F2 is shown in Fig. 5.8(b). The 13.3 ± 4.3 day lag identified by GPR may represent a lower harmonic of the 22.1 day delay in the light curve.

Disentangling flare F2's light curve to identify primary flares and their echo counterparts is particularly challenging. A double-peak structure observed from MJD 56081 to MJD 56098 has a delayed, demagnified counterpart appearing from MJD 56101 to MJD 56118, with a demagnification factor of approximately 1.9, as illustrated in Fig. 5.9(b). However, no echo counterpart is detected for the broader feature between MJD 56142 and MJD 56156 within the 20-day time delay. This absence suggests a much higher demagnification, likely corresponding to a longer time delay.

5.3.3 Flare F3 - MJD 58363 - 58963

Figure 5.5(a) presents the 1-day and 12-hour binned light curves for flare F3, which marks the brightest flux state of the source. During this flare, the flux reaches 14 times the average level, making it the most intense and longest-lasting flare analyzed in this study, spanning an impressive 600 days. The power spectral index

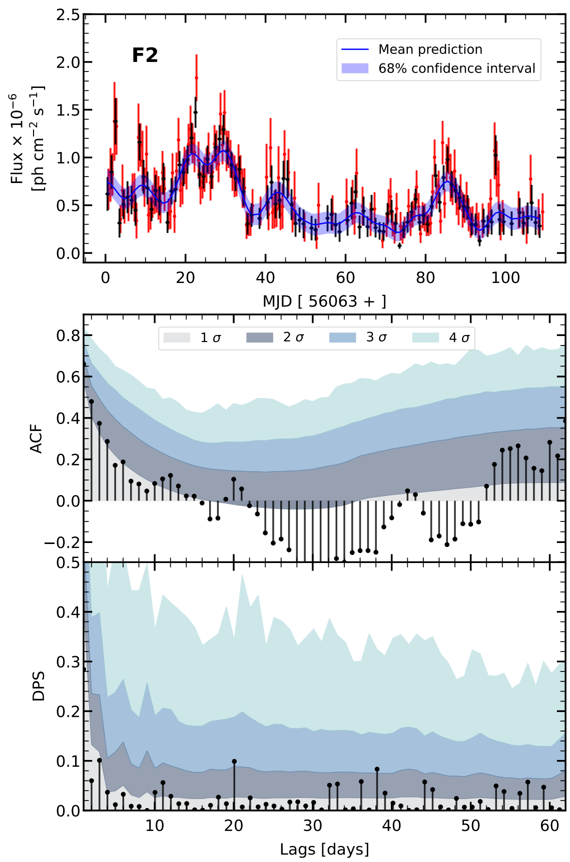

Figure 5.4: (Top panel) 1-day binned (black) and 12hr binned (red) light curve of flaring epochs F2 [MJD 56063 - 56173] (marked in Figure 5.1) of FSRQ PKS 1830−211. In blue is the GPR predictions on 1-day binned data with largest marginal likelihood (Middle panel) ACF on 1-day binned light curve of F2 period (Bottom panel) DPS on 1-day binned light curve of F2 period.

for this flare indicates a transition between pink and red noise behavior. Multiple overlapping flares appear superimposed on a broader envelope, as depicted in Fig. 5.5(a).

The Autocorrelation Function (ACF), shown in Fig. 5.5(b), reveals two highly significant features ($> 3\sigma$): one at 12 ± 1.8 days and another at 21.1 ± 1.2 days. Similarly, DPS method identifies a prominent lag of 21.0 ± 0.5 days ($\gtrsim 3.5\sigma$) and another at 19.0 ± 0.5 days ($= 3\sigma$). Less significant but still notable lags ($\gtrsim 2.5\sigma$)

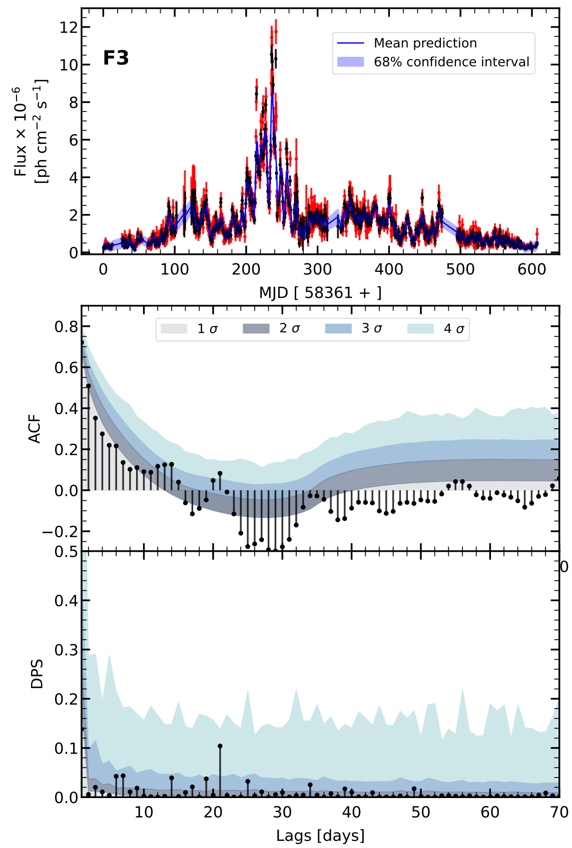

Figure 5.5: (Top panel) 1-day binned (black) and 12hr binned (red) light curve of flaring epochs F3 [MJD 58363 - 58963] (marked in Fig. 5.1) of FSRQ PKS 1830−211. In blue is the GPR predictions on 1-day binned data with largest marginal likelihood (Middle panel) ACF on 1-day binned light curve of F3 period (Bottom panel) DPS on 1-day binned light curve of F3 period.

are observed at 14 ± 0.5 days and 25 ± 0.5 days. These results suggest the presence of multiple lag values imprinted on the flare, potentially reflecting time differences between subsets of overlapping flares. GPR corroborates these findings, detecting consistent lags of 14.0 ± 2.2 and 21.1 ± 1.2 days, aligning with both ACF and DPS results (Fig. 5.8(c)).

The dense overlap of flaring periods during this epoch makes it challenging to distinguish leading and trailing counterparts, thereby preventing the estimation of magnification ratios for flare F3.

5.3.4 Flare F4 - MJD 59063 - 59153

Figure 5.6 presents the 1-day and 12-hour binned light curves for flare F4, spanning 90 days. Among the five analyzed states, flare F4 is the least bright and exhibits the lowest variability. The power spectral density for the 1-day binned data yields a spectral index of $k = 0.88 \pm 0.47$. Ideally, the light curve's duration should be at least twice the maximum expected time delay of 70 days to maximize the likelihood of detecting time delays. The limited 90-day span of flare F4 reduces this probability. Furthermore, the flare demonstrates minimal fractional variability, with $F_{var,F4} = 0.19 \pm 0.05$, underscoring the absence of significant flux variations in the light curve.

No significant time delays were detected using either the ACF or the DPS methods in the 1-day binned data. However, GPR estimated a lag of 22.4 ± 2.2 days, as shown in Fig. 5.8(d). The lack of significant echo flares corresponding to the flux increase between MJD 59113 and MJD 59123 (Fig. 5.6(a)) makes it challenging to confirm the detectability of a lensed image within the sensitivity limits of the telescope.

5.3.5 Flare F5 - MJD 59683 - 59943

Figure 5.7(a) presents the 1-day and 12-hour binned light curves for flare F5, spanning 260 days and characterized by multiple visible peaks. Approximately 18.1% of the data includes gaps or periods of significantly low detection, which were interpolated with zeros to maintain continuity in the analysis. No significant time lags were detected using the ACF. However, the DPS method identified a time lag of 17 ± 0.5 days with more than 2σ significance, consistent with the time delay estimated using GPR at 19.4 ± 2.7 days (Fig. 5.8(e)).

The bright peaks observed between MJD 59890 and MJD 59928 (F51) were modeled

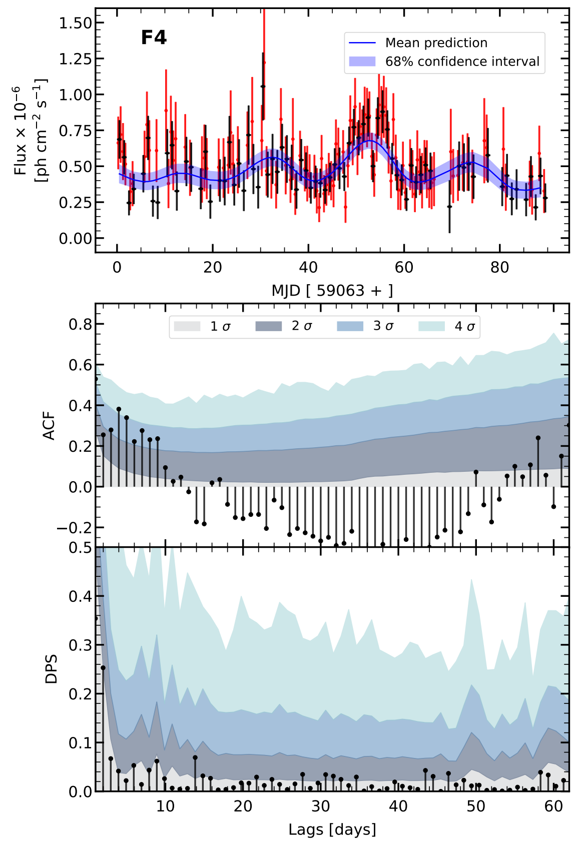

Figure 5.6: (Top panel) 1-day binned (black) and 12hr binned (red) light curve of flaring epochs F4 [MJD 59063 - 59153] (marked in Fig. 5.1) of FSRQ PKS 1830−211. In blue is the GPR predictions on 1-day binned data with largest marginal likelihood (Middle panel) ACF on 1-day binned light curve of F4 period (Bottom panel) DPS on 1-day binned light curve of F4 period.

using an exponential function, as shown in Fig. 5.9(c). However, the presence of multiple overlapping flares complicates the association of specific flares, making it challenging to reliably estimate magnification ratios.

5.4 Discussion

The time delays estimated using the three methods employed in this study — ACF, DPS, and GPR — are summarized in Table 5.3. This work introduces a novel approach utilizing GPR to extract lags in the signal, alongside the established ACF

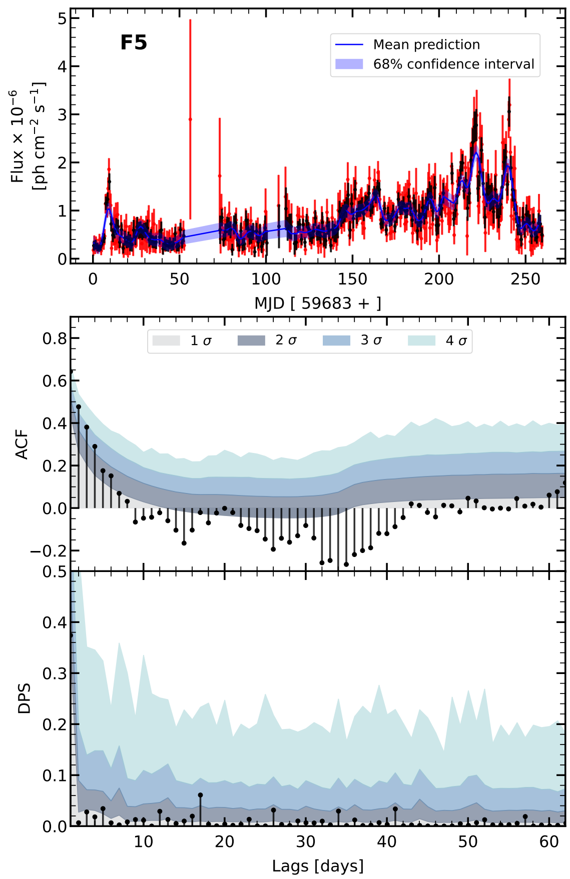

Figure 5.7: (Top panel) 1-day binned (black) and 12hr binned (red) light curve of flaring epochs F5 [MJD 59683 - 59943] (marked in Fig. 5.1) of FSRQ PKS 1830−211. In blue is the GPR predictions on 1-day binned data with largest marginal likelihood (Middle panel]) ACF on 1-day binned light curve of F5 period (Bottom panel) DPS on 1-day binned light curve of F5 period.

and DPS methods commonly used to estimate intrinsic lensed delays.

Our analysis reveals that ACF struggles to efficiently detect intrinsic time delays in most signals due to its sensitivity to noise. However, among the five flares studied, ACF successfully identified an intrinsic lag in flare F3 with a significance exceeding 3σ. This flare, exhibiting a transition between pink and red noise behavior and the presence of multiple overlapping flares, enabled significant detection. The results from DPS and GPR corroborated the findings for flare F3. Overall, the analysis

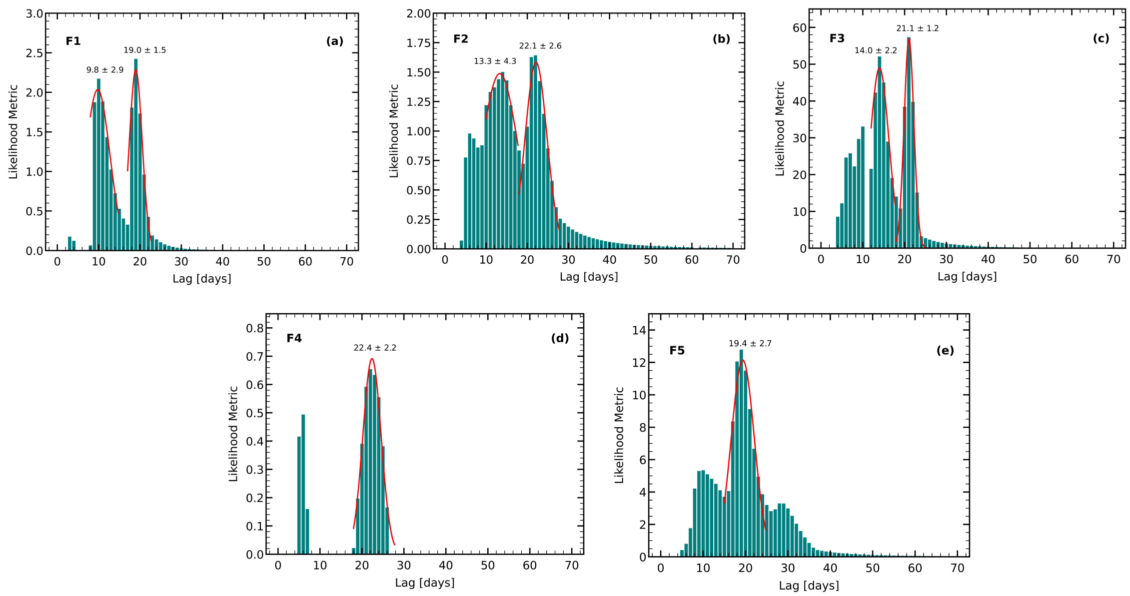

Figure 5.8: The likelihood metric for lags is derived using GPR. The bar represents the likelihood value for each lag, with the highest value indicating the most probable lag. The red Gaussian fit over the likelihood values represents the mean lag value estimated and its corresponding error bar.

suggests a consistent time delay of approximately 20 days during the flaring states of the source, as determined by all three methods. This consistency indicates a stable orientation of the emitting region relative to the mass distribution of the lens. Consequently, the γ-ray emission appears to originate from similar regions of the jet across all flaring states.

The inferred time delay aligns with the estimated lag reported by Barnacka et al. [2015] during high states, supporting the hypothesis that the γ-ray emission originates within the core of the jet. Additionally, the detection of rapid variability ($t_{var} \sim 0.38 \pm 0.22$ days) implies an emission region size of $r_{emm} = c\delta t_{var}/(1+z) = 2.8 \times 10^{15}$ cm, located at a distance of $R_{diss} = 2c\Gamma^2 t_{var} = 0.064$ pc. These findings confirm that the high-energy emission is confined to sub-parsec scales within the core.

Lovell et al. [1996] reported a time delay of 26^{+4}_{-5} days in PKS 1830−211 using the Australian Telescope Compact Array at 8.6 GHz. Similar delays were observed in the γ-ray band during the quiet state of the source [Barnacka et al., 2011]. However, the shorter time delay observed during high states in this study suggests a distinct origin for flaring γ-ray emission. The discrepancy between the γ-ray and radio time delays highlights differences in dissipation sites for these emissions, particularly during the source's high state. Radio emission is typically associated with the outer regions of the parsec-scale jet. At smaller scales, synchrotron self-absorption in a compact jet renders radio emission unlikely in the inner parsec region. Conversely, shorter time delays during active γ-ray states indicate that the dissipation occurs closer to the central engine. This behavior aligns with observations of high-energy photon absorption (above 10 GeV) during high states, driven by interactions with BLR photons at sub-parsec scales [Agarwal et al., 2024]. These findings suggest that γ-ray dissipation occurs in the innermost regions of the jet, while radio dissipation originates farther downstream.

The high-energy spectral properties of the source and its echo flares are consistent within 3σ, as shown in Fig. 5.10. Any deviation in spectral properties would indicate a varying influence of soft seed photons on γ-ray photons through $\gamma - \gamma$ absorption when passing through a more luminous region of the lensing galaxy. For flare F21, a deviation of $\sim 2.8\sigma$ was observed in the spectral index. The consistent β parameters across the four identified lensed flares suggest a uniform influence of external seed photons from the local jet environment, the EBL, and the intervening galaxy on the high-energy spectrum. This uniform absorption indicates that all the flares likely originate from similar regions of the jet.

Our analysis focused on flares with a clearly identifiable source and a demagnified lensed echo at average flux levels, leading us to select flares F1, F2, and F5. In contrast, flare F3 posed challenges due to the presence of multiple overlapping flares,

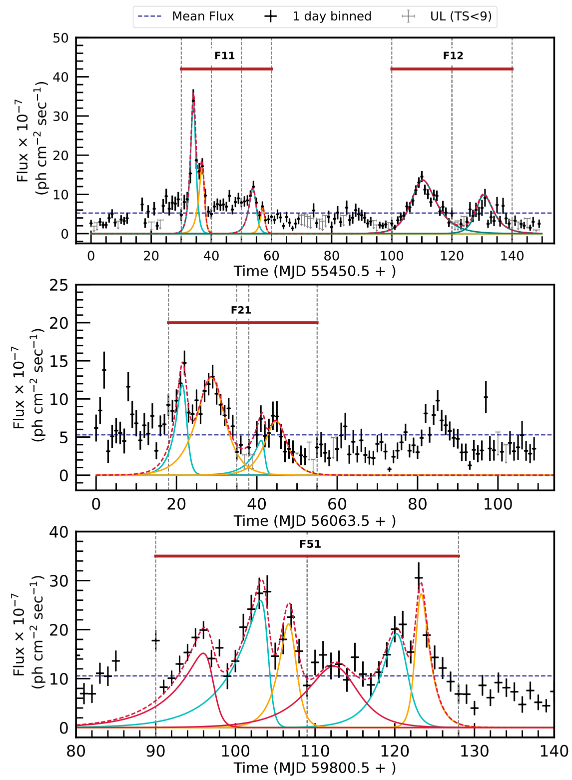

Figure 5.9: High flux states of flare F1, F2 and zoomed section of F5 (MJD 59880 - 59940) and fitted exponential flare using equation 5.11 . The vertical lines represent the source and echo pair for the lensed flares. The exponential fits with similar colors are considered possible pairs of source and echo flares.

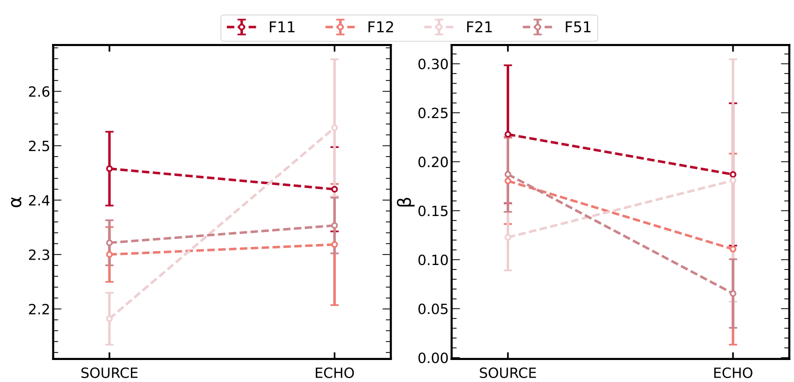

Figure 5.10: High energy spectral parameter of the flare and its associated echo flare. (left) α and (right) β for the fitted log-parabola model.

making it inefficient to isolate individual flares and their echoes, likely caused by the merging of multiple emission events. Exponential fitting of individual flares revealed a linear relationship between time lag and magnification. This relationship suggests that smaller emission regions are confined closer to the base of the jet, while larger magnifications correspond to larger emission regions located farther downstream in the jet. However, further studies with more isolated and distinct flares are necessary to refine these findings.

5.5 Summary

Strong gravitational lensing in γ-ray bright blazars provides a unique opportunity to pinpoint the locations of γ-ray emission during both quiescent and active states. Variations in time delays observed during periods of increased γ-ray flux suggest that emission regions within the jet differ from those during low-flux states [Barnacka et al., 2011]. The consistent lag across five flaring states, as observed in this study, points to a common origin for high-energy γ-ray activity within the radio core. In contrast, the larger lags seen during quiescent γ-ray periods and consistent time delays in radio observations indicate that radio emission originates farther from the central engine compared to the γ-ray emission during flaring periods. These time delays caused by gravitational lensing can also help constrain the Hubble parameter [Refsdal, 1964].

This study introduces a novel method for estimating time delays in long, continuous *Fermi*-LAT light curves. Detecting such delays is pivotal for identifying hidden lensed blazars during flaring periods, particularly those not recognized as lensed sources in radio wavelengths. The characteristic signatures of time delays in γ-ray light curves could provide valuable insights into distant blazars and uncover previously unidentified γ-ray sources.

Looking ahead, future surveys, including those by the Square Kilometre Array

(SKA), are expected to discover numerous lensed quasars. Comprehensive multi-wavelength investigations of these systems will yield critical insights into the origins of high-energy radiation, offering a magnified perspective of the jet structure and its emission regions—capabilities currently limited by existing telescopes.

Chapter 6

GeV point searches over extended sky patches

6.1 Motivation

Gamma-ray emission in blazars serves as a powerful diagnostic tool for probing the innermost regions of jets and their environments. Previous chapters utilized basic *Fermi*-LAT point-source analyses to examine the origin of fast variability as a means to understand the underlying particle acceleration process and associated radiation processes. However, gaining a comprehensive understanding of the mechanisms responsible for gamma-ray emissions requires advanced studies, particularly those incorporating simultaneous multimessenger observations.

Over the past decade, multimessenger astrophysics has transformed our understanding of extreme astrophysical environments by unveiling high-energy cosmic neutrinos and gravitational wave (GW) sources. Unlike gamma rays, neutrinos and GWs are minimally affected by absorption or scattering, making them excellent messengers of distant, high-energy events. However, their weak interaction with matter, while enabling unimpeded travel across cosmic distances, presents a formidable challenge for detection, requiring large, highly sensitive detectors.

Efforts to trace the origins of these multimessenger events rely on coordinated multiwavelength and multimessenger campaigns across diverse observational facilities. While these approaches have enhanced our understanding, they are often hindered by the limited localization capabilities of the detectors, compounded by the transient and diffuse nature of potential sources, which impedes the detection of associated sources without rapid and precise follow-up. Furthermore, the complexity of coordinating simultaneous observations across multiple observatories introduces another layer of difficulty to these efforts. [Halzen, 2016; Mo et al., 2024; Sturani, 2013].

Despite these challenges, two extragalactic sources have been identified as significant neutrino emitters by the IceCube facility: TXS 0506+056 (3.5 σ) [IceCube Collaboration et al., 2018b] and NGC 1068 (4.2 σ) [IceCube Collaboration et al., 2022], firmly establishing AGNs as potential neutrino emitters. The detection of neutrino emission from the blazar TXS 0506+056 in 2017 marked a milestone in multimessenger astrophysics. This identification relied on simultaneous multiwavelength follow-up observations, including gamma-rays detected by Fermi-LAT and very-high-energy (VHE) gamma-rays from MAGIC, corresponding to the IceCube-170922A alert. These observations confirmed the flaring blazar as the likely source of the neutrino emission [IceCube Collaboration et al., 2018a].

However, the two identified AGN neutrino counterparts, TXS 0506+056 and NGC 1068, contribute only about 1% of the diffuse flux of high-energy astrophysical neutrinos [Aartsen et al., 2020; IceCube Collaboration et al., 2018a,b, 2022]. Broader searches for neutrino counterparts suggest that AGNs collectively contribute at most 20% of the total observed emission [Aartsen et al., 2017; Hooper et al., 2019; Smith et al., 2021]. This significant discrepancy highlights a major gap in our understanding of the origins of the diffuse high-energy neutrino flux, emphasizing the need for further investigation.

Similarly, gravitational wave (GW) detected by present facilities such as LIGO, VIRGO, and KAGRA are sensitive to signals from compact object mergers. Some of these mergers, particularly those associated with the progenitors of short gamma-ray bursts (GRBs), produce both a short-lived gamma-ray signal ($\leq$ 2 seconds) immediately after the merger (the "prompt emission") and a longer-lived broadband afterglow emission lasting from minutes to hours. If the jet emission from the GRB falls within the field of view (FoV) – either due to a jet oriented toward the observer or off-axis emission becoming visible at later times – it is possible to detect gamma-ray emission following a GW trigger. In such cases, the *Fermi*-LAT data serve as an efficient tool for identifying gamma-ray counterparts to GW events.

Despite these possibilities, electromagnetic (EM) counterpart searches to GW events remain limited by the rapid and transient nature of such phenomena, which often hinders simultaneous observations. The limited sensitivity of instruments and incomplete understanding of associated counterparts further add to the challenges of detection. However, a major milestone in multimessenger astrophysics was achieved in 2017 with the detection of GW170817, a neutron star merger accompanied by EM counterparts, including GRB 170817A [Abbott et al., 2017]. This event opened a new observational window into high-energy transient phenomena and confirmed compact binary mergers as progenitors of short gamma-ray bursts. Nevertheless, no other gamma-ray counterparts to any other GW event have been identified following GW170817, highlighting the need for enhanced detection strategies and more comprehensive theoretical models.

In this context, we conduct an extended search for gamma-ray sources over wide regions of the sky using *Fermi*-LAT, an all-sky monitoring telescope discussed in Chapter 2.1. *Fermi*-LAT is particularly well-suited for observing point transient events that might otherwise be missed by ground-based telescopes with narrower fields of view. *Fermi*-LAT provides consistent and reliable monitoring of the gamma-ray sky by scanning the entire sky every three hours. Its capability, coupled with 15 years of uninterrupted observations since 2008, makes it an invaluable resource for identifying transient sources in poorly localized multimessenger events, especially those lacking late-time counterparts. Such extended searches are pivotal for detecting counterparts to multimessenger events.

6.2 Pipeline

Typically, *Fermi*-LAT searches focus on point sources with an energy-dependent point spread function. For point source analyses, the LAT achieves angular resolutions of $< 3.5°$ at 100 MeV and $< 0.15°$ above 10 GeV, with a field of view spanning 2.4 sr. To extend these point-source searches over a broader region of the sky—necessary for counterpart identification in poorly localized multimessenger events—we implement a targeted 100 ks observation strategy following a GW trigger (t_{GW}).

As an example, to present the capabilities of the developed tool, we describe LAT observations of the localization region for GW190814, which was detected by LIGO Livingston, LIGO Hanford, and Virgo on 2019 August 14 at 21:11:00 UTC. This search encompasses both the immediate post-trigger window and extends to late-time observations (up to 100 ks) to identify potential EM γ-ray counterparts.

The LIGO and Virgo Collaborations performed a bayesian parameter estimation analysis of GW190814 using a coherent framework that incorporated data from LIGO Livingston, LIGO Hanford, and Virgo. This analysis employed uninformative priors and utilized the `LALInference` stochastic sampling software [Abbott et al., 2020]. Two scenarios were evaluated: a binary black hole (BBH) merger and a neutron star–black hole (NSBH) merger, with tidal effects included in the modeling for the NSBH hypothesis. The absence of detectable tidal deformability signatures, consistent with the system's unequal mass ratio and the significant mass of the secondary object, led to the adoption of BBH waveform models for detailed quantitative analysis [Abbott et al., 2020]. However, uncertainties persist on the nature of the secondary compact object [Biswas et al., 2021]. The analysis constrained the source distance to a range of 220–330 Mpc and localized the sky position to an area of 38 deg^2 at the 90% credible level.

Despite an extensive multimessenger campaign encompassing radio, optical, infrared [Ackley et al., 2020; Alexander et al., 2021; Andreoni et al., 2020; Antier et al., 2020; Dobie et al., 2019; Gomez et al., 2019; Lipunov et al., 2019; Vieira et al., 2020; Watson et al., 2020], and neutrino searches [Abbasi et al., 2021; Ageron et al., 2019], no counterpart was identified during follow-up pointed observations. Notably, no counterpart searches were conducted immediately following the trigger.

To address this, we conducted a gamma-ray search across the extended 90% credible sky region associated with the event, spanning a time window from the GW trigger to 100 ks post-trigger. The analysis employed the standard likelihood analysis methodology for LAT data, incorporating a point-source search conducted systematically using a grid-based approach.

The 90% credible region was derived from the multi-resolution `HEALPix` sky map (distinguished by the `.multiorder.fits` file extension) using the methodology provided by the International Gravitational-Wave Observatory Network (IGWN) [1].

The credible region provided by LIGO was resampled into grids with dimensions of $0.5° \times 0.5°$. This grid size was selected to align with the Fermi LAT PSF at 1 GeV, which has a 60% containment radius of approximately 1°. While smaller grid sizes could enhance resolution, they would significantly increase computational cost. The search centers, referred to as 'pointings' (centers of regions of interest, or RoIs, for Fermi LAT searches), for each grid box were determined based on the median distribution of the sky map pixels within the grid. The resulting grid and associated pointings are illustrated in Figure 6.1.

[1] https://emfollow.docs.ligo.org/userguide/tutorial/multiorder_skymaps.html

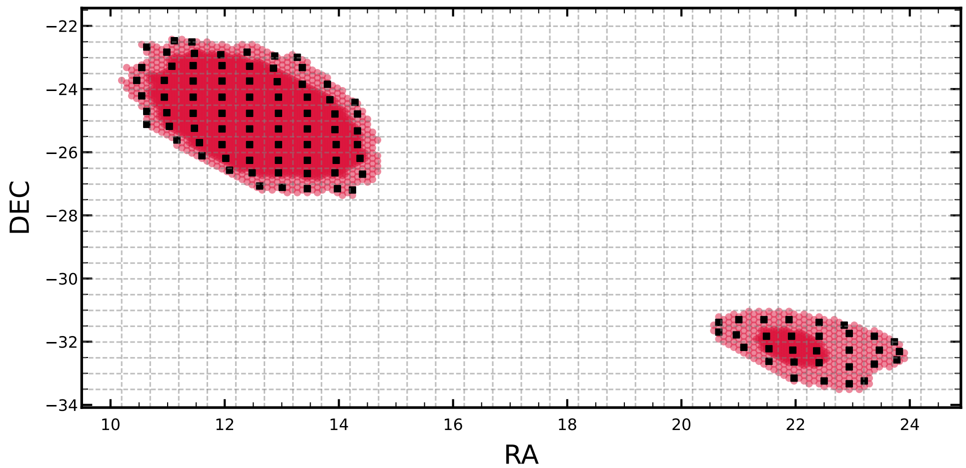

Figure 6.1: Skymap of GW 190818 (90% credible region) with the grids spaced 0.5°

Before performing the Fermi-LAT point search analysis over the identified *pointings* within each grid cell, we impose the condition that at least 70% of the credible region associated with the GW merger event must fall within the FoV of the Fermi-LAT observation. A point in the sky is considered observable by LAT if it lies within the 70° radius FoV and maintains a zenith angle smaller than 100°. The zenith angle constraint is applied to eliminate contamination from Earth's albedo. Taking these factors into account, the LAT coverage over GW patch is determined by integrating the probability density function for each *pointing* across the successive grid cells of the LIGO localization probability map that are observable by Fermi-LAT at a given time. This approach identifies observation epochs that ensure a minimum of 70% LAT coverage of the LIGO map. Subsequently, a detailed point search is conducted for each *pointing* within the grid cells, as described below.

6.2.1 Point analysis

The standard analysis procedure employs the Fermi ScienceTools framework, as outlined in Section 2.1.1, to process LAT data in the energy range of 100 MeV to

10 GeV. The analysis covers a time window from the trigger time up to 100 ks, with flexibility to adjust the duration depending on the specific scientific objectives. Given the transient nature of events associated with GW, the initial focus is on the first 100 ks post-trigger. Data is extracted for a ROI with a 14° radius to accomodate all the sources within the grid of size (5° × 5°) for each *pointing*. We also apply a zenith angle cut of 100° to minimize contamination from Earth's albedo. Quality refinement cuts are implemented using `GTMKTIME`, with the conditions `DATA_QUAL > 0 && LAT_CONFIG == 1` and `evtype = 3`, ensuring the selection of high-quality photon data. The refined dataset is analyzed using unbinned likelihood methods, associating detected photons with nearby sources listed in the 4FGL catalog. Sources within 8° of the ROI are left free to vary during the analysis, while sources beyond 8° are fixed to their catalog parameters to maintain accurate source modeling. The source spectrum is modeled using a simple power-law[2] representation:

$$\frac{dN}{dE} = N_\circ \left(\frac{E}{E_\circ}\right)^{-\Gamma}, \tag{6.1}$$

where, $N_\circ$ is the normalization factor, Γ is the spectral index, and $E_\circ$ is the energy scale. Spectral parameters derived from the unbinned analysis are evaluated across multiple energy bins. The detection significance is quantified using the TS, defined as:

$$\mathrm{TS} = -2\ln(\mathcal{L}_0/\mathcal{L}_1), \tag{6.2}$$

where $\mathcal{L}_0$ is the likelihood of the model without the point source, and $\mathcal{L}_1$ is the likelihood of the model including the point source at the position of interest.

The analysis was performed over two distinct time binning approaches:

1. *Targeted* search: This time bin included epochs between 0 and 20 ks, during which at least 70

[2] https://fermi.gsfc.nasa.gov/ssc/data/analysis/scitools/source_models.html

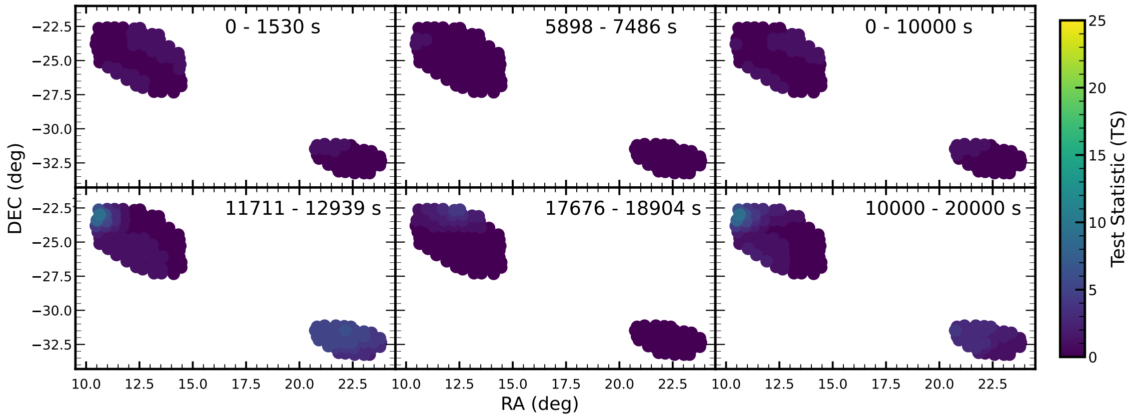

Figure 6.2: TS map for GW190814 (90% credible region) generated from *targeted* search up to 20 ks.

2. *Uniform* search: This binning approach divided the 0–100 ks time window into equally spaced intervals of 20 ks.

A point search was conducted for each *pointing* within the grid cells for both binning strategies, resulting in the associated flux and TS values. TS maps were generated for all *pointings*, providing indications of the presence or absence of significant sources across the extended sky region. A threshold of TS$\geq$ 25 was applied for source detection.

The TS map for the *targeted* search up to 20 ks is presented in Figure 6.2, while the TS maps for *uniform* search of 20 ks intervals up to 100 ks are shown in Figure 6.3.

6.2.2 Luminosity upper limit in localization region

The evaluation of the flux upper limit involves the following steps:

1. **Input Parameters**: For each '*pointing*', we utilize the flux upper limit (F_i), probability density (p_i), and the distance luminosity ($D_{L,i}$) distribution characterized by its mean of distance luminosity ($(D_{L,mean})_i$) and its standard deviation ($(D_{L,sigma})_i$). Probability density is probability per unit solid angle

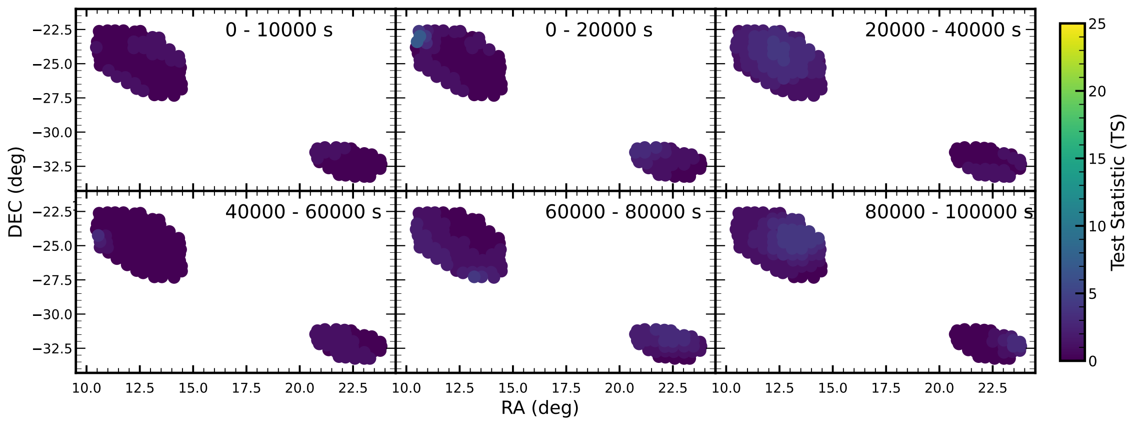

Figure 6.3: TS map for GW190814 (90% credible region) generated from *uniform* search up to 100 ks.

(typically in steradians) that the source of the gravitational wave is located at a specific point on the sky.

2. **Luminosity Calculation**: The luminosity for each pixel is computed using the relation:

$$L_{\mathrm{LAT},i} = 4\pi F_i (D_{L,i})^2$$

3. **Combined Upper Limit**: For the selected time interval, the combined upper limit over the entire GW localization region is calculated as a weighted average of the pixel-wise luminosities, with the probabilities (p_i) serving as weights. The weighted average ensures that pixels with higher probabilities contribute proportionally to the combined upper limit.

This approach provides a robust estimate of the gamma-ray luminosity upper limit for the extended GW localization region during the specified observation period. The luminosity evolution for the GW patch is shown in Figure 6.4.

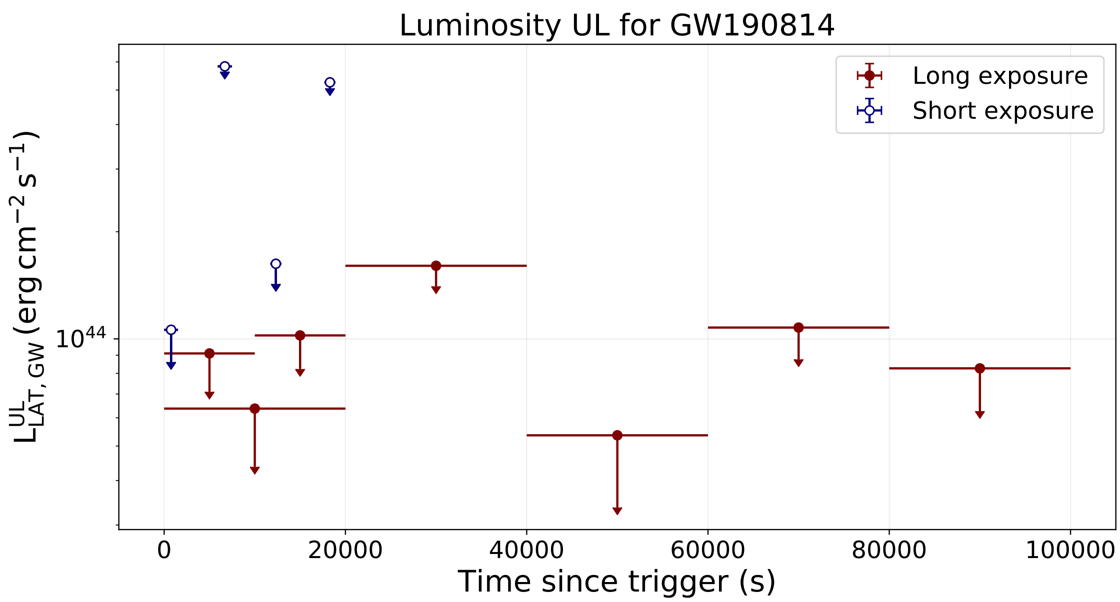

Figure 6.4: Averaged Luminosity upperlimit for GW190814 (100 MeV - 10 GeV)

6.3 Result and Discussion

The Fermi-LAT's unique all-sky scanning capability enables effective searches for gamma-ray counterparts associated with extended sky regions, such as those arising from multimessenger events. For the gravitational wave event GW190814, the standard Fermi-LAT point search analysis was extended to cover a broader sky region to identify potential EM counterparts.

The LAT intermittently achieved 70% coverage of the GW localization region, facilitating a focused short-time search within the initial 20 ks post-trigger. Additionally, an extended temporal window up to 100 ks was analyzed to investigate potential late-time gamma-ray emissions associated with the event. Despite these efforts, no LAT counterpart was detected (6.2). An upper limit was established on the GeV γ-ray luminosity within the LIGO localization region as discussed in § 6.2.2.

The tool holds significant potential for application in the upcoming LIGO O5 run, scheduled for 2027, to facilitate the search for EM counterparts. This capability can enhance multi-wavelength searches for potential sources identified in the gamma-ray band. The improved sensitivity anticipated during the O5 run is expected to yield smaller localization regions, enabling more efficient preliminary searches for GeV counterparts.

Furthermore, neutrino observatories such as IceCube and ANTARES, along with upcoming facilities like KM3NeT and IceCube-Gen2, offer promising opportunities for coordinated searches. These efforts could enhance the identification of EM counterparts to multimessenger events, further advancing the field of astrophysical transient studies.

Chapter 7

Summary and Outlook

7.1 Thesis Summary

The origin of variability in blazar emission, ranging from rapid (minute-scale) fluctuations to long-term (year-scale) changes, remains a central problem in the study of astrophysical jets. Key uncertainties include the physical processes driving these changes, the mechanisms responsible for accelerating high-energy particles over vast distances in relativistic jets, and the poorly understood composition of these jets—whether dominated by electrons, protons, or a combination of both. Resolving these questions is essential for understanding the dynamic nature of blazar jets and their role in high-energy astrophysical phenomena.

Blazars, due to their alignment with the observer's line of sight, provide unique insights into relativistic jets. Their Doppler-boosted emission dominates over other components, such as the host galaxy and accretion disk, making them valuable probes of jet dynamics. The observed spectral and temporal variability, spanning a wide range of timescales, highlights the need to understand the mechanisms and locations of particle acceleration within these jets. By investigating extreme variability in the high-energy band (X-ray to gamma-ray) and examining the influence of the jet environment, this thesis sheds light on the sites of energy dissipation and the processes driving these dynamic phenomena.

This work first delves into the variability and emission mechanisms in BL Lac, focusing on the interplay between high-energy processes and jet dynamics during its high-activity periods. The observed gamma-ray and X-ray variability—encompassing rapid minute-scale changes, shifts in the SED, and sub-hour flares—reveals the dynamic nature of particle acceleration and energy dissipation within the jet. The gamma-ray spectrum, well-described by a log-parabola model, demonstrates spectral hardening with flux increases, suggesting freshly accelerated or re-energized electrons. Notably, the stability of the curvature parameter over years of observation indicates a consistent influence of external UV photons, likely from the BLR, on jet emission. Detailed modeling places the emission region at distances of $\sim 10^3$ gravitational radii from the central engine, where synchrotron cooling and inverse Compton processes dominate during flares. These findings highlight localized dissipation zones beyond the BLR as critical sites for understanding the extreme variability and energetic processes in blazars.

The findings challenge conventional shock-in-jet models, as the extreme Doppler factors required to reconcile the observed rapid variability are difficult to justify. Instead, a jet-in-jet scenario involving magnetic reconnection provides a more plausible explanation [Giannios et al., 2009]. Reconnection-driven plasmoids, aligned with the observer's line of sight, offer a consistent framework to explain the observed rapid variability, spectral shifts, and high-energy flares. The growth and decay timescales of these plasmoids, coupled with Doppler-boosted emissions, account for the observed SED evolution and flaring patterns. This mechanism not only aligns with the observed variability but also explains the interplay between long-term envelope emission and fast flares, underscoring the role of magnetic reconnection as one of the dominant particle acceleration process in blazar jets. Building on these insights, the spectral shifts and fast variability observed in blazars hint at dominant gamma-ray emission originating near the edge of the BLR, driven by particle acceleration processes such as magnetic reconnection.

To refine this understanding, this thesis also examines the spectral breaks and absorption features in the high-energy γ-ray spectrum of FSRQ PKS 1424−418, focusing on how local conditions in the jet environment affect emission during high and low activity states. At energies above 10 GeV, significant absorption is observed during high states, caused by interactions between γ-ray photons and external photons from the BLR. In contrast, during low states, such absorption is minimal, suggesting that external photon fields, apart from the EBL, have a smaller influence. The emission region during high states is likely located near the outer edge of the BLR ($\sim$0.45 pc), where low-ionization lines such as Hα and Hβ dominate absorption. These findings point to flaring activity originating in inner jet regions close to soft photon sites like the BLR or accretion disk, offering a more detailed view of the interplay between jet dynamics and their surrounding environments.

Further analysis reveals that the accretion disk contributes minimally to gamma-ray absorption beyond the BLR, as its photons interact weakly with the jet's $\gamma-$ray emissions. During high states, the observed flux follows a lognormal distribution, indicative of stochastic processes such as magnetic reconnection near the BLR's edge. These findings underscore the dynamic role of the BLR and accretion disk in shaping the gamma-ray spectrum and suggest that the emission region is located just beyond the outer edge of the BLR. By connecting spectral variability to specific physical processes and jet environments, this work advances our understanding of the mechanisms driving blazar emissions and provides a foundation for future explorations of their extreme behaviors.

Temporal variability is often a key tool for localizing gamma-ray dissipation sites, but studying high-redshift blazars poses unique challenges due to significant EBL absorption and the limited sensitivity of current telescopes. Gravitationally lensed blazars, however, offer a unique opportunity to resolve gamma-ray production zones in these distant sources by providing a spatially resolved view of their jets. The time delays between lensed signals provide critical insights into the spatial distribution of emission sites relative to the lens's mass-weighted center. This study reveals that, during flaring periods, gamma-ray emission originates closer to the central engine, likely within the radio core, as indicated by consistent time delays across five flaring states. In contrast, larger time delays during quiescent periods suggest that radio emission arises farther along the jet. Gravitational lensing in gamma-ray bright blazars thus emerges as a powerful tool to probe the jet structure and localize gamma-ray dissipation regions during both quiescent and active states.

This thesis introduces a novel method to estimate time delays from long Fermi-LAT light curves, aiding in the identification of hidden lensed blazars, particularly those undetected at radio wavelengths. Future surveys, such as those conducted by the Square Kilometer Array, are expected to significantly expand the catalog of lensed quasars, enabling detailed multi-wavelength studies. These investigations will deepen our understanding of high-energy radiation origins and jet structures, providing insights into the extreme environments of blazars that are currently beyond the reach of existing telescopes.

Additionally, this thesis introduces a novel tool designed to search for point GeV sources across large sky patches, which is particularly valuable for multimessenger astronomy. This tool facilitates the identification of GeV counterparts to neutrino-associated events, which are potentially linked to hadronic processes in the relativistic jets of astrophysical sources. Moreover, it can be employed to search for GeV counterparts to gravitational wave events, offering the potential to detect relativistic jet emissions associated with compact object mergers. By enabling these advanced studies, this tool bridges the gap between gamma-ray observations and multimessenger phenomena, paving the way for future discoveries

7.2 Thesis Outlook

This thesis provides a significant contribution to understanding the gamma-ray emission mechanisms in blazars by elucidating the impact of the local jet environment, particularly the role of the BLR's soft seed photons. The identification of fast variability and consistent time lags across multiple flaring epochs, especially in the context of a lensed quasar, highlight a similar origin of gamma-ray emission during flaring events, likely near the edge of the BLR. In contrast, the emission during quiescent periods points to regions outside the BLR, aligning with moving VLBI radio knots along the jet.

The investigations conducted in this thesis primarily focus on the origin of gamma-ray emission in relativistic jets of blazars, providing critical insights into their variable nature. However, these studies represent only a partial glimpse into the complex behavior of such jets. There is ample opportunity for further research to expand upon these findings by conducting in-depth analysis of a sample a larger sample of AGNs, particularly examining jets both aligned and unaligned with the observer's line of sight.

Currently, our study on the imprint of the BLR on stacked flaring and quiescent epochs is limited to a single source, chosen based on its black hole mass. While this approach offered valuable insights, understanding the broader implications of the study requires similar investigations across a larger sample of sources with a wide range of black hole masses. This should include both flat-spectrum radio quasars (FSRQs) and BL Lacertae (BL Lac) objects, as their distinct emission characteristics may offer complementary perspectives on the interplay between black hole mass, jet local environment, and gamma-ray variability.

To further explicitly understand the origin of flares in blazar, and its contribution from factors other than the orientation of jet, a diverse study on observed variability from non-aligned AGNs with observed VHE detection needs to be conducted. The very high energy (VHE, > 0.1 TeV) extragalactic gamma-ray sky is dominated by radio-loud AGNs, particularly blazars, whose emissions are amplified by relativistic beaming as their jets point toward Earth. Of the 89 known extragalactic VHE emitters, 83 are blazars, four are radio galaxies (RGs), and two (IC 310 and PKS 0625$-$35) exhibit hybrid features of RGs and BL Lac objects [Rulten, 2022]. The origin of fast variability in unaligned jetted VHE sources, however, remains unclear, as such variability is often attributed to Doppler boosting effects observed in blazars. Addressing this uncertainty requires future studies to investigate the physical conditions in unaligned jetted sources, including detailed comparisons with their blazar counterparts. Currently, VHE AGN observations are largely conducted in pointing mode during flaring events, resulting in limited sky coverage and underrepresentation of low-luminosity AGNs (LLAGNs).

The GeV gamma-ray sky (100 MeV - 300 GeV), benefits from continuous all-sky monitoring by the Fermi Gamma-ray Space Telescope. The availability of 16 years of Fermi data presents a valuable opportunity to investigate emissions from unaligned jetted AGNs and to uncover key differences in emission mechanisms between aligned and misaligned sources.

Additionally, neutrino detection from radio galaxies has emerged as a complementary field of research alongside gamma-ray studies. Hadronic interactions in AGN jets are expected to yield gamma-ray emissions, yet some high-energy neutrino sources remain opaque to GeV–TeV gamma rays. The association of a high-energy neutrino event with the flaring blazar TXS 0506+056 underscores the potential of AGNs as neutrino sources. Furthermore, IceCube's 4.2σ detection of neutrinos (79^{+22}_{-20} TeV) from NGC 1068 suggests that even gamma-ray faint jet sources, such as Seyfert galaxies, may emit neutrinos. Linking radio-bright AGNs with strong parsec-scale cores to IceCube neutrino events presents a promising avenue for future research. By utilizing 16 years of Fermi archival data, researchers can explore TeV-unexplored regions of the sky and establish connections between gamma-ray emissions, neutrino production, and jet properties in AGNs.

The tools developed in this thesis for extended GeV point searches can also play a significant role in multi-messenger astronomy, particularly in the search for electromagnetic counterparts to gravitational wave events. While this thesis demonstrates their application to one compact merger event (GW190814), future work can extend these tools to poorly localized multi-messenger searches, including those over GW patches and neutrino localization regions. These tools could prove especially valuable during LIGO's upcoming O5 run, scheduled for 2027, when improved sensitivity is expected to reduce localization regions significantly.

References

Aartsen, M. G., Abraham, K., Ackermann, M., et al. 2017, The Contributon of FERMI-2LAC Blazars to Diffuse TeV–PeV Neutrino Flux, The Astrophysical Journal, 835, 45

Aartsen, M. G., Ackermann, M., Adams, J., et al. 2020, Time-Integrated Neutrino Source Searches with 10 Years of IceCube Data, Phys. Rev. Lett., 124, 051103

Abbasi, R., Ackermann, M., Adams, J., et al. 2021, Follow-up of Astrophysical Transients in Real Time with the IceCube Neutrino Observatory, The Astrophysical Journal, 910, 4

Abbasi, R., Ackermann, M., Adams, J., et al. 2024, IceCube Search for Neutrino Emission from X-ray Bright Seyfert Galaxies, arXiv e-prints, arXiv:2406.07601

Abbott, B. P., Abbott, R., Abbott, T. D., et al. 2017, Gravitational Waves and Gamma-Rays from a Binary Neutron Star Merger: GW170817 and GRB 170817A, The Astrophysical Journal Letters, 848, L13

Abbott, R., Abbott, T. D., Abraham, S., et al. 2020, GW190814: Gravitational Waves from the Coalescence of a 23 Solar Mass Black Hole with a 2.6 Solar Mass Compact Object, The Astrophysical Journal Letters, 896, L44

Abdo, A. A., Ackermann, M., Ajello, M., et al. 2009, Fermi/Large Area Telescope Bright Gamma-Ray Source List, The Astrophysical Journal Supplement, 183, 46

Abdo, A. A., Ackermann, M., Ajello, M., et al. 2010, Gamma-ray Light Curves and Variability of Bright Fermi-detected Blazars, The Astrophysical Journal, 722, 520

Abdo, A. A., Ackermann, M., Ajello, M., et al. 2011, The First Fermi Multifrequency Campaign on BL Lacertae: Characterizing the Low-activity State of the Eponymous Blazar, The Astrophysical Journal, 730, 101

Abdo, A. A., Ackermann, M., Ajello, M., et al. 2015, Gamma-Ray Flaring Activity from the Gravitationally Lensed Blazar PKS 1830-211 Observed by Fermi LAT, The Astrophysical Journal, 799, 143

Abdollahi, S., Acero, F., Baldini, L., Ballet, J., et al. 2022, Incremental Fermi Large Area Telescope Fourth Source Catalog, The Astrophysical Journal Supplement Series, 260, 53

Abeysekara, A. U., Archambault, S., Archer, A., et al. 2015, Gamma-Rays from the Quasar PKS 1441+25: Story of an Escape, The Astrophysical Journal Letter, 815, L22

Abeysekara, A. U., Benbow, W., Bird, R., et al. 2018, Multiwavelength Observations of the Blazar BL Lacertae: A New Fast TeV Gamma-Ray Flare, The Astrophysical Journal, 856, 95

Abhir, J., Joseph, J., Pgm, S. R., & Bose, D. 2021, Multi-frequency temporal and spectral variability study of blazar PKS 1424-418, Monthly Notices of the Royal Astronomical Society, 501, 2504

Abolmasov, P., & Poutanen, J. 2017, Gamma-ray opacity of the anisotropic stratified broad-line regions in blazars, Monthly Notices of the Royal Astronomical Society, 464, 152

Abraham, J., Abreu, P., Aglietta, M., et al. 2007, Correlation of the Highest-Energy Cosmic Rays with Nearby Extragalactic Objects, Science, 318, 938

Acciari, V. A., Ansoldi, S., Antonelli, L. A., et al. 2021, Multiwavelength variability and correlation studies of Mrk 421 during historically low X-ray and γ-ray activity in 2015-2016, Monthly Notices of the Royal Astronomical Society, 504, 1427

Ackermann, M., Ajello, M., Allafort, A., et al. 2011, The Second Catalog of Active Galactic Nuclei Detected by the Fermi Large Area Telescope, The Astrophysical Journal, 743, 171

Ackermann, M., Ajello, M., Allafort, A., et al. 2012, The Imprint of the Extragalactic Background Light in the Gamma-Ray Spectra of Blazars, Science, 338, 1190

Ackermann, M., Ajello, M., Allafort, A., et al. 2013, Detection of the Characteristic Pion-Decay Signature in Supernova Remnants, Science, 339, 807

Ackermann, M., Anantua, R., Asano, K., et al. 2016, Minute-timescale ¿100 MeV γ-Ray Variability during the Giant Outburst of Quasar 3C 279 Observed by Fermi-LAT in 2015 June, The Astrophysical Journal Letter, 824, L20

Ackley, K., Amati, L., Barbieri, C., et al. 2020, Observational constraints on the optical and near-infrared emission from the neutron star–black hole binary merger candidate S190814bv, Astronomy & Astrophysics, 643, A113

Adriani, O., Barbarino, G. C., Bazilevskaya, G. A., et al. 2011, PAMELA Measurements of Cosmic-Ray Proton and Helium Spectra, Science, 332, 69

Agarwal, S., Shukla, A., Mannheim, K., Vaidya, B., & Banerjee, B. 2024, Imprint of "Local Opacity" Effect in Gamma-Ray Spectrum of Blazar Jet, The Astrophysical Journal Letter, 968, L1

Agarwal, S., Shukla, A., & Sharma, P. 2025, Constraining gamma-ray dissipation site in gravitationally lensed quasar - PKS 1830211, Monthly Notices of the Royal Astronomical Society, staf021

Agarwal, S., Banerjee, B., Shukla, A., et al. 2023, Flaring activity from magnetic reconnection in BL Lacertae, Monthly Notices of the Royal Astronomical Society Letters, 521, L53

Ageron, M., Baret, B., Coleiro, A., et al. 2019, LIGO/Virgo S190814bv: no neutrino counterpart candidate in ANTARES search, GRB Coordinates Network, 25330, 1

Aharonian, F., & Bogovalov, S. 2003, Exploring physics of rotation powered pulsars with sub-10 GeV imaging atmospheric Cherenkov telescopes, New Astronomy, 8, 85

Aharonian, F., Akhperjanian, A. G., Bazer-Bachi, A. R., et al. 2007, An Exceptional Very High Energy Gamma-Ray Flare of PKS 2155–304, The Astrophysical Journal, 664, L71

Akaike, H. 1974, A new look at the statistical model identification, IEEE Transactions on Automatic Control, 19, 716

Albert, J., Aliu, E., Anderhub, H., et al. 2007, Variable Very High Energy -Ray Emission from Markarian 501, The Astrophysical Journal, 669, 862

Aleksić, J., Antonelli, L. A., Antoranz, P., et al. 2011a, MAGIC Discovery of Very High Energy Emission from the FSRQ PKS 1222+21, The Astrophysical Journal Letter, 730, L8

Aleksić, J., Antonelli, L. A., Antoranz, P., et al. 2011b, MAGIC Observations and multiwavelength properties of the quasar 3C 279 in 2007 and 2009, A&A, 530, A4

Aleksić, J., Ansoldi, S., Antonelli, L. A., et al. 2014, Black hole lightning due to particle acceleration at subhorizon scales, Science, 346, 1080

Alexander, K. D., Schroeder, G., Paterson, K., et al. 2021, A Late-time Galaxy-targeted Search for the Radio Counterpart of GW190814, The Astrophysical Journal, 923, 66

Álvarez-Muñiz, J., Alves Batista, R., Balagopal V., A., Bolmont, J., et al. 2019, The Giant Radio Array for Neutrino Detection (GRAND): Science and design, Science China Physics, Mechanics & Astronomy, 63, 219501

Andreoni, I., Goldstein, D. A., Kasliwal, M. M., et al. 2020, The Astrophysical Journal, 890, 131

Andrew, B. H., Macleod, J. M., Locke, J. L., Medd, W. J., & Purton, C. R. 1969, Rapid Radio Variations in BL Lac, Nature, 223, 598

Angel, J. R. P., & Stockman, H. S. 1980, Optical and infrared polarization of active extragalactic objects, ARA&A, 18, 321

Antier, S., Agayeva, S., Aivazyan, V., et al. 2020, The first six months of the Advanced LIGO's and Advanced Virgo's third observing run with GRANDMA, Monthly Notices of the Royal Astronomical Society, 492, 3904

Antonucci, R. 1993, Unified models for active galactic nuclei and quasars, Ann. Rev. Astron. Astrophys., 31, 473

Arlen, T., Aune, T., Beilicke, M., et al. 2012, Rapid TeV gamma-ray flaring of BL Lacertae, The Astrophysical Journal, 762, 92

Arnaud, K. A. 1996, in Astronomical Society of the Pacific Conference Series, Vol. 101, Astronomical Data Analysis Software and Systems V, ed. G. H. Jacoby & J. Barnes, 17

Arons, J. 1981, Pair creation above pulsar polar caps - Steady flow in the surface acceleration zone and polar CAP X-ray emission, The Astrophysical Journal, 248, 1099

Atwood. 2007, The Violent Universe, The Les Houches Winter School, Scineghe2014, 016

Atwood, W. B., Abdo, A. A., Ackermann, M., et al. 2009, The Large Area Telescope on the Fermi Gamma-Ray Space Telescope Mission, The Astrophysical Journal, 697, 1071

Ballet, J., Bruel, P., Burnett, T. H., Lott, B., & The Fermi-LAT collaboration. 2023, Fermi Large Area Telescope Fourth Source Catalog Data Release 4 (4FGL-DR4), arXiv e-prints, arXiv:2307.12546

Banasiński, P., Bednarek, W., & Sitarek, J. 2016, Orphan γ-ray flares from relativistic blobs encountering luminous stars, Monthly Notices of the Royal Astronomical Society, 463, L26

Baring, M. G., Böttcher, M., & Summerlin, E. J. 2016, Probing acceleration and turbulence at relativistic shocks in blazar jets, Monthly Notices of the Royal Astronomical Society, 464, 4875

Barnacka, A. 2013, Detection techniques for the H.E.S.S. II telescope, data modeling of gravitational lensing and emission of blazars in HE-VHE astronomy, arXiv e-prints, arXiv:1307.4050

Barnacka, A., Geller, M. J., Dell'Antonio, I. P., & Benbow, W. 2014, Strong Gravitational Lensing as a Tool to Investigate the Structure of Jets at High Energies, The Astrophysical Journal, 788, 139

Barnacka, A., Geller, M. J., Dell'Antonio, I. P., & Benbow, W. 2015, Resolving the High-energy Universe with Strong Gravitational Lensing: The Case of PKS 1830-211, The Astrophysical Journal, 809, 100

Barnacka, A., Glicenstein, J. F., & Moudden, Y. 2011, First evidence of a gravitational lensing-induced echo in gamma rays with Fermi LAT, A&A, 528, L3

Barthelmy, S. D., Barbier, L. M., Cummings, J. R., Fenimore, E. E., et al. 2005, The Burst Alert Telescope (BAT) on the SWIFT Midex Mission, Space Science Reviews, 120, 143

Becker, J. K., Meli, A., & Biermann, P. L. 2011, Neutrinos from photo-hadronic interactions in Pks2155-304, Nuclear Instruments and Methods in Physics Research A, 630, 269

Begelman, M. C., Fabian, A. C., & Rees, M. J. 2008, Implications of very rapid TeV variability in blazars, Monthly Notices of the Royal Astronomical Society, 384, 19

Berton, M., Foschini, L., Caccianiga, A., et al. 2017, An Orientation-Based Unification of Young Jetted AGN: The Case of 3C 286, Frontiers in Astronomy and Space Sciences, 4, doi:10.3389/fspas.2017.00008

Bhatta, G. 2021, Characterizing Long-term Optical Variability Properties of γ-Ray-bright Blazars, The Astrophysical Journal, 923, 7

Bignami, G. F., Boella, G., Burger, J. J., et al. 1975, The COS-B experiment for gamma-ray astronomy., Space Science Instrumentation, 1, 245

Biswas, B., Nandi, R., Char, P., Bose, S., & Stergioulas, N. 2021, GW190814: on the properties of the secondary component of the binary, Monthly Notices of the Royal Astronomical Society, 505, 1600

Biteau, J., & Giebels, B. 2012, The minijets-in-a-jet statistical model and the rms-flux correlation, A&A, 548, A123

Bland-Hawthorn, J., Maloney, P. R., Sutherland, R. S., & Madsen, G. J. 2013, Fossil Imprint of a Powerful Flare at the Galactic Center Along the Magellanic Stream, The Astrophysical Journal, 778, 58

Blandford, R., & Eichler, D. 1987, Particle acceleration at astrophysical shocks: A theory of cosmic ray origin, Physics Reports, 154, 1

Blandford, R., Rees, M., & Wolfe, A. 1978, Pittsburgh conference on BL Lac objects, AM Wolfe, Ed, 328

Blandford, R. D., & Levinson, A. 1995, Pair Cascades in Extragalactic Jets. I. Gamma Rays, The Astrophysical Journal, 441, 79

Blandford, R. D., & Narayan, R. 1992, Cosmological applications of gravitational lensing., ARA&A, 30, 311

Blandford, R. D., & Znajek, R. L. 1977, Electromagnetic extraction of energy from Kerr black holes., Monthly Notices of the Royal Astronomical Society, 179, 433

Blasi, P. 2013, The origin of galactic cosmic rays, A&ARv, 21, 70

Błażejowski, M., Sikora, M., Moderski, R., & Madejski, G. 2000, Comptonization of infrared radiation from hot dust by relativistic jets in quasars, The Astrophysical Journal, 545, 107

Bloom, S. D., & Marscher, A. P. 1996, An analysis of the synchrotron self-compton model for the multi–wave band spectra of blazars, Astrophysical Journal v. 461, p. 657, 461, 657

Boettcher, M., & Dermer, C. D. 2010, Timing signatures of the internal-shock model for blazars, The Astrophysical Journal, 711, 445

Bosch-Ramon, V., & Khangulyan, D. 2009, Understanding the Very-High Emission from Microquasars, International Journal of Modern Physics D, 18, 347

Böttcher, M. 2019, Progress in multi-wavelength and multi-messenger observations of blazars and theoretical challenges, Galaxies, 7, 20

Böttcher, M., Dermer, C. D., & Finke, J. D. 2008, The hard VHE γ-ray emission in high-redshift TeV blazars: Comptonization of cosmic microwave background radiation in an extended jet?, The Astrophysical Journal, 679, L9

Böttcher, M., Reimer, A., Sweeney, K., & Prakash, A. 2013, Leptonic and Hadronic Modeling of Fermi-detected Blazars, The Astrophysical Journal, 768, 54

Brault, J. W., & White, O. R. 1971, The Analysis and Restoration of Astronomical Data via the Fast Fourier Transform, A&A, 13, 169

Bromberg, O., & Levinson, A. 2009, Recollimation and Radiative Focusing of Relativistic Jets: Applications to Blazars and M87, The Astrophysical Journal, 699, 1274

Burrows, D. N., Hill, J. E., Nousek, J. A., Kennea, J. A., et al. 2005, The Swift X-Ray Telescope, Space Science Reviews, 120, 165

Buson, S., Longo, F., Larsson, S., et al. 2014, Unusual flaring activity in the blazar PKS 1424-418 during 2008-2011, A&A, 569, A40

Cardelli, J. A., Clayton, G. C., & Mathis, J. S. 1989, The Relationship between Infrared, Optical, and Ultraviolet Extinction, The Astrophysical Journal, 345, 245

Carswell, R. F. 1975, Redshifts of BL Lac objects, Nature, 253, 589

Casandjian, J. M., & Grenier, I. A. 2008, A revised catalogue of EGRET γ-ray sources, A&A, 489, 849

Celotti, A., & Ghisellini, G. 2008, The power of blazar jets, Monthly Notices of the Royal Astronomical Society, 385, 283

Cerruti, M. 2020, Neutrinos from blazars, Journal of Physics: Conference Series, 1468, 012094

Chatterjee, R., Das, S., Khasnovis, A., Ghosh, R., et al. 2021, Short-timescale variability of the blazar Mrk 421 from AstroSat and simultaneous multi-wavelength observations, Journal of Astrophysics and Astronomy, 42, 80

Cheng, K. S., Chernyshov, D. O., Dogiel, V. A., Ko, C. M., & Ip, W. H. 2011, Origin of the Fermi Bubble, The Astrophysical Journal Letter, 731, L17

Cheng, K. S., Ho, C., & Ruderman, M. 1986, Energetic Radiation from Rapidly Spinning Pulsars. I. Outer Magnetosphere Gaps, The Astrophysical Journal, 300, 500

Cheung, C. C., Larsson, S., Scargle, J. D., et al. 2014, Fermi Large Area Telescope Detection of Gravitational Lens Delayed γ-Ray Flares from Blazar B0218+357, The Astrophysical Journal Letter, 782, L14

Connolly, S. D. 2015, A Python Code for the Emmanoulopoulos et al. [arXiv:1305.0304] Light Curve Simulation Algorithm, arXiv e-prints, arXiv:1503.06676

Corbett, E. A., Robinson, A., Axon, D. J., et al. 1996, The appearance of broad Hα in BL Lacertae, Monthly Notices of the Royal Astronomical Society, 281, 737

Costamante, L., Cutini, S., Tosti, G., Antolini, E., & Tramacere, A. 2018, On the origin of gamma-rays in Fermi blazars: beyondthe broad-line region, Monthly Notices of the Royal Astronomical Society, 477, 4749

Crocker, R. M., & Aharonian, F. 2011, Fermi Bubbles: Giant, Multibillion-Year-Old Reservoirs of Galactic Center Cosmic Rays, Phys. Rev. Lett., 106, 101102

Dermer, C. D., & Schlickeiser, R. 1993, Model for the high-energy emission from blazars, Astrophysical Journal v. 416, p. 458, 416, 458

Dermer, C. D., Schlickeiser, R., & Mastichiadis, A. 1992, High-energy gamma radiation from extragalactic radio sources., A&A, 256, L27

Dobie, D., Stewart, A., Murphy, T., et al. 2019, An ASKAP search for a radio counterpart to the first high-significance neutron star–black hole merger LIGO/virgo s190814bv, The Astrophysical Journal Letters, 887, L13

Domínguez, A., Primack, J. R., Rosario, D. J., et al. 2011, Extragalactic background light inferred from AEGIS galaxy-SED-type fractions, Monthly Notices of the Royal Astronomical Society, 410, 2556

Drury, L. O., Aharonian, F. A., & Voelk, H. J. 1994, The gamma-ray visibility of supernova remnants. A test of cosmic ray origin, A&A, 287, 959

D'Ammando, F. 2021, NICER, NuSTAR, and Swift follow-up observations of the -ray flaring blazar BL Lacertae in 2020 August–October, MNRAS, 509, 52

Edelson, R. A., Krolik, J. H., & Pike, G. F. 1990, Broad-Band Properties of the CfA Seyfert Galaxies. III. Ultraviolet Variability, The Astrophysical Journal, 359, 86

Einstein, A. 1936, Lens-Like Action of a Star by the Deviation of Light in the Gravitational Field, Science, 84, 506

Eisenstein, D. J., & Hut, P. 1998, HOP: A New Group-Finding Algorithm for N-Body Simulations, The Astrophysical Journal, 498, 137

Emmanoulopoulos, D., McHardy, I. M., & Papadakis, I. E. 2013, Generating artificial light curves: revisited and updated, Monthly Notices of the Royal Astronomical Society, 433, 907

Ezhikode, S. H., Shukla, A., Dewangan, G. C., et al. 2022, Long-term Optical and γ-Ray Variability of the Blazar PKS 1222+216, The Astrophysical Journal, 939, 76

Fan, Z.-H., & Cao, X. 2004, Black Hole Masses and Doppler Factors of Gamma-Ray Active Galactic Nuclei, The Astrophysical Journal, 602, 103

Fender, R. 2001, in American Institute of Physics Conference Series, Vol. 558, High Energy Gamma-Ray Astronomy: International Symposium, ed. F. A. Aharonian & H. J. Völk (AIP), 221–233

Fichtel, C. E., Hartman, R. C., Kniffen, D. A., et al. 1975, High-energy gamma-ray results from the second Small Astronomy Satellite., The Astrophysical Journal, 198, 163

Finkbeiner, D. P. 2004, Microwave Interstellar Medium Emission Observed by the Wilkinson Microwave Anisotropy Probe, The Astrophysical Journal, 614, 186

Finke, J. D. 2016, External Compton Scattering in Blazar jets and the Location of the gamma-ray emitting region, The Astrophysical Journal, 830, 94

Finke, J. D., & Becker, P. A. 2014, Fourier Analysis of Blazar Variability, The Astrophysical Journal, 791, 21

Finke, J. D., Dermer, C. D., & Böttcher, M. 2008, Synchrotron Self-Compton Analysis of TeV X-Ray-Selected BL Lacertae Objects, The Astrophysical Journal, 686, 181

Finke, J. D., Razzaque, S., & Dermer, C. D. 2010, Modeling the Extragalactic Background Light from Stars and Dust, The Astrophysical Journal, 712, 238

Foschini, L., Ghisellini, G., Tavecchio, F., Bonnoli, G., & Stamerra, A. 2011, Search for the shortest variability at gamma rays in flat-spectrum radio quasars, A&A, 530, A77

Franceschini, A., Rodighiero, G., & Vaccari, M. 2008, Extragalactic optical-infrared background radiation, its time evolution and the cosmic photon-photon opacity, A&A, 487, 837

Fuentes, A., Gómez, J. L., Martí, J. M., et al. 2023, Filamentary structures as the origin of blazar jet radio variability, Nature Astronomy, 7, 1359

Ghirlanda, G., Ghisellini, G., Tavecchio, F., Foschini, L., & Bonnoli, G. 2011, The radio–-ray connection in Fermi blazars, Monthly Notices of the Royal Astronomical Society, 413, 852

Ghisellini, G. 2015, Swift for blazars, Journal of High Energy Astrophysics, 7, 163, swift 10 Years of Discovery, a novel approach to Time Domain Astronomy

Ghisellini, G., Righi, C., Costamante, L., & Tavecchio, F. 2017, The Fermi blazar sequence, Monthly Notices of the Royal Astronomical Society, 469, 255

Ghisellini, G., & Tavecchio, F. 2008, Rapid variability in TeV blazars: the case of PKS 2155—304, Monthly Notices of the Royal Astronomical Society: Letters, 386, L28

Ghisellini, G., & Tavecchio, F. 2009, Canonical high-power blazars, Monthly Notices of the Royal Astronomical Society, 397, 985

Ghisellini, G., Tavecchio, F., Maraschi, L., Celotti, A., & Sbarrato, T. 2014, The power of relativistic jets is larger than the luminosity of their accretion disks, Nature, 515, 376

Ghisellini, G., Tagliaferri, G., Foschini, L., et al. 2011, High-redshift Fermi blazars, Monthly Notices of the Royal Astronomical Society, 411, 901

Giannios, D. 2013, Reconnection-driven plasmoids in blazars: fast flares on a slow envelope, MNRAS, 431, 355

Giannios, D., Uzdensky, D. A., & Begelman, M. C. 2009, Fast TeV variability in blazars: jets in a jet, Monthly Notices of the Royal Astronomical Society: Letters, 395, L29

Gilmore, R. C., Somerville, R. S., Primack, J. R., & Domínguez, A. 2012, Semi-analytic modelling of the extragalactic background light and consequences for extragalactic gamma-ray spectra, Monthly Notices of the Royal Astronomical Society, 422, 3189

Giommi, P., & Padovani, P. 2021, Astrophysical neutrinos and blazars, Universe, 7, 492

Giuliani, A., Cardillo, M., Tavani, M., et al. 2011, Neutral Pion Emission from Accelerated Protons in the Supernova Remnant W44, The Astrophysical Journal Letter, 742, L30

Gomez, S., Hosseinzadeh, G., Cowperthwaite, P. S., et al. 2019, A Galaxy-targeted Search for the Optical Counterpart of the Candidate NS–BH Merger S190814bv with Magellan, The Astrophysical Journal Letters, 884, L55

Goswami, S. 2023, Search for high-energy neutrino emission from hard X-ray AGN with IceCube, arXiv e-prints, arXiv:2307.15349

Goyal, A., Soida, M., Stawarz, Ł., et al. 2022, Multiwavelength Variability Power Spectrum Analysis of the Blazars 3C 279 and PKS 1510-089 on Multiple Timescales, The Astrophysical Journal, 927, 214

Goyal, A., Stawarz, Ł., Ostrowski, M., et al. 2017, Multiwavelength Variability Study of the Classical BL Lac Object PKS 0735+178 on Timescales Ranging from Decades to Minutes, The Astrophysical Journal, 837, 127

Goyal, A., Soida, M., Łukasz Stawarz, et al. 2022, Multiwavelength Variability Power Spectrum Analysis of the Blazars 3C 279 and PKS 1510–089 on Multiple Timescales, The Astrophysical Journal, 927, 214

Greisen, K. 1966, End to the Cosmic-Ray Spectrum?, Phys. Rev. Lett., 16, 748

Guo, F., & Mathews, W. G. 2012, The Fermi Bubbles. I. Possible Evidence for Recent AGN Jet Activity In The Galaxy, The Astrophysical Journal, 756, 181

H. E. S. S. Collaboration, Abramowski, A., Acero, F., et al. 2013, H.E.S.S. discovery of VHE γ-rays from the quasar PKS 1510-089, A&A, 554, A107

Halzen, F. 2016, High-energy neutrino astrophysics, Nature Phys., 13, 232

Harris, D. E., & Krawczynski, H. 2006, X-Ray Emission from Extragalactic Jets, ARA&A, 44, 463

Harrison, C. 2014, PhD thesis, Durham University, UK

Hartman, R. C., Bertsch, D. L., Fichtel, C. E., et al. 1992, in NASA Conference Publication, Vol. 3137, NASA Conference Publication, ed. C. R. Shrader, N. Gehrels, & B. Dennis, 116–125

Hartman, R. C., Bertsch, D. L., Fichtel, C. E., et al. 1996, in American Astronomical Society Meeting Abstracts, Vol. 189, American Astronomical Society Meeting Abstracts, 101.07

Hartman, R. C., Bertsch, D. L., Bloom, S. D., et al. 1999, The Third EGRET Catalog of High-Energy Gamma-Ray Sources, The Astrophysical Journal Supplement, 123, 79

Heckman, T. M., & Best, P. N. 2014, The Coevolution of Galaxies and Supermassive Black Holes: Insights from Surveys of the Contemporary Universe, Annual Review of Astronomy and Astrophysics, 52, 589

Helgason, K., & Kashlinsky, A. 2012, Reconstructing the γ-Ray Photon Optical Depth of the Universe to z ~4 from Multiwavelength Galaxy Survey Data, The Astrophysical Journal Letter, 758, L13

Hess, V. 2018, On the Observations of the Penetrating Radiation during Seven Balloon Flights, arXiv e-prints, arXiv:1808.02927

Hill, J. E., Burrows, D. N., Nousek, J. A., et al. 2004, in X-Ray and Gamma-Ray Instrumentation for Astronomy XIII, ed. K. A. Flanagan & O. H. W. Siegmund, Vol. 5165, International Society for Optics and Photonics (SPIE), 217 – 231

Hirotani, K., & Shibata, S. 1999, One-dimensional electric field structure of an outer gap accelerator — II. -ray production resulting from inverse Compton scattering, Monthly Notices of the Royal Astronomical Society, 308, 67

Hoffmeister, C. 1929, 354 neue Veränderliche, Astronomische Nachrichten, 236, 233

Hooper, D., Linden, T., & Vieregg, A. 2019, Active galactic nuclei and the origin of IceCube's diffuse neutrino flux, Journal of Cosmology and Astroparticle Physics, 2019, 012

Hörandel, J. R. 2003, On the knee in the energy spectrum of cosmic rays, Astroparticle Physics, 19, 193

IceCube Collaboration, Aartsen, M. G., Ackermann, M., et al. 2018a, Multimessenger observations of a flaring blazar coincident with high-energy neutrino IceCube-170922A, Science, 361

IceCube Collaboration, Aartsen, M. G., Ackermann, M., et al. 2018b, Neutrino emission from the direction of the blazar TXS 0506+056 prior to the IceCube-170922A alert, Science, 361, 147

IceCube Collaboration, Abbasi, R., Ackermann, M., et al. 2022, Evidence for neutrino emission from the nearby active galaxy NGC 1068, Science, 378, 538

Inoue, Y., Inoue, S., Kobayashi, M. A. R., et al. 2013, Extragalactic Background Light from Hierarchical Galaxy Formation: Gamma-Ray Attenuation up to the Epoch of Cosmic Reionization and the First Stars, The Astrophysical Journal, 768, 197

Isler, J. C., Urry, C. M., Coppi, P., et al. 2013, A Time-resolved Study of the Broad-line Region in Blazar 3C 454.3, The Astrophysical Journal, 779, 100

Isobe, N., Sato, R., Ueda, Y., et al. 2015, MAXI Investigation into the Long-term X-Ray Variability from the Very-high-energy γ-Ray Blazar Mrk 421, The Astrophysical Journal, 798, 27

Jankowsky, F., Ait-Benkhali, F., Zacharias, M., & Wagner, S. J. 2022, Further optical brightening of the blazar PKS 1424-418, The Astronomer's Telegram, 15552, 1

Jauncey, D. L., Reynolds, J. E., Tzioumis, A. K., et al. 1991, An unusually strong Einstein ring in the radio source PKS1830–211, Nature, 352, 132

Jorstad, S. G., Marscher, A. P., Lister, M. L., Stirling, A. M., et al. 2005, Polarimetric Observations of 15 Active Galactic Nuclei at High Frequencies: Jet Kinematics from Bimonthly Monitoring with the Very Long Baseline Array, AJ, 130, 1418

Jorstad, S. G., Marscher, A. P., Mattox, J. R., et al. 2001, Multiepoch Very Long Baseline Array Observations of EGRET-detected Quasars and BL Lacertae Objects: Connection between Superluminal Ejections and Gamma-Ray Flares in Blazars, The Astrophysical Journal, 556, 738

Jorstad, S. G., Marscher, A. P., Raiteri, C. M., et al. 2022, Rapid quasi-periodic oscillations in the relativistic jet of BL Lacertae, Nature, 609, 265

Kadler, M., Stevens, J., Ojha, R., Edwards, P. G., & Roesch, F. 2022, ATCA finds a long-term radio outburst of PKS1424-418 coincident with optical/gamma-ray flaring activity, The Astronomer's Telegram, 15536, 1

Kadler, M., Krauß, F., Mannheim, K., et al. 2016, Coincidence of a high-fluence blazar outburst with a PeV-energy neutrino event, Nature Physics, 12, 807

Kalberla, P. M. W., Burton, W. B., Hartmann, D., et al. 2005, The Leiden/Argentine/Bonn (LAB) Survey of Galactic HI. Final data release of the combined LDS and IAR surveys with improved stray-radiation corrections, A&A, 440, 775

Kampert, K.-H., & Tinyakov, P. 2014, Cosmic rays from the ankle to the cutoff, Comptes Rendus Physique, 15, 318, ultra-high-energy cosmic rays: From the ankle to the tip of the spectrum

Kataoka, J., Mattox, J., Quinn, J., et al. 1999, High-energy emission from the TeV blazar Markarian 501 during multiwavelength observations in 1996, The Astrophysical Journal, 514, 138

Kharb, P., Blackman, E. G., Clausen-Brown, E., et al. 2024, Relativistic Jet Motion in the Radio-quiet LINER Galaxy KISSR 872, The Astrophysical Journal, 962, 180

Kneiske, T. M., Bretz, T., Mannheim, K., & Hartmann, D. H. 2004, Implications of cosmological gamma-ray absorption. II. Modification of gamma-ray spectra, A&A, 413, 807

Kneiske, T. M., & Dole, H. 2010, A lower-limit flux for the extragalactic background light, A&A, 515, A19

Komissarov, S. S., Vlahakis, N., Königl, A., & Barkov, M. V. 2009, Magnetic acceleration of ultrarelativistic jets in gamma-ray burst sources, Monthly Notices of the Royal Astronomical Society, 394, 1182

Koopmans, L. V. E., & de Bruyn, A. G. 2005, HI kinematics in a massive spiral galaxy at z= 0.89, Monthly Notices of the Royal Astronomical Society, 360, L6

Kraushaar, W. L., & Clark, G. W. 1962, Search for Primary Cosmic Gamma Rays with the Satellite Explorer XI, Phys. Rev. Lett., 8, 106

Kraushaar, W. L., Clark, G. W., Garmire, G. P., et al. 1972, High-Energy Cosmic Gamma-Ray Observations from the OSO-3 Satellite, The Astrophysical Journal, 177, 341

Kun, E., Bartos, I., Tjus, J. B., et al. 2024, Possible correlation between unabsorbed hard x rays and neutrinos in radio-loud and radio-quiet active galactic nuclei, Phys. Rev. D, 110, 123014

La Mura, G. 2022, Fermi-LAT detection of renewed gamma-ray activity from the FSRQ PKS 1424-41, The Astronomer's Telegram, 15807, 1

Law, C. J. 2010, A Multiwavelength View of a Mass Outflow from the Galactic Center, The Astrophysical Journal, 708, 474

Lei, M., & Wang, J. 2014, The effect of the broad-line region with geometrical structures on gamma-ray absorption in blazars, PASJ, 66, 7

León-Tavares, J., Chavushyan, V., Patiño-Álvarez, V., et al. 2013, Flare-like Variability of the Mg II λ2800 Emission Line in the Γ-Ray Blazar 3C 454.3, The Astrophysical Journal Letter, 763, L36

LHAASO Collaboration. 2024, Ultrahigh-Energy Gamma-ray Emission Associated with Black Hole-Jet Systems, arXiv e-prints, arXiv:2410.08988

Li, J., Torres, D. F., Liu, R.-Y., et al. 2020, Gamma-ray heartbeat powered by the microquasar SS 433, Nature Astronomy, 4, 1177

Linsley, J. 1963, in 8th International Cosmic Ray Conference

Lipunov, V., Gorbovskoy, E., Kornilov, V., et al. 2019, LIGO/Virgo S190814bv Global MASTER-Net observations report, GRB Coordinates Network, 25322, 1

Liu, B. F., & Mineshige, S. 2002, in 8th Asian-Pacific Regional Meeting, Volume II, ed. S. Ikeuchi, J. Hearnshaw, & T. Hanawa, 391–392

Liu, H. T., & Bai, J. M. 2006, Absorption of 10-200 GeV Gamma Rays by Radiation from Broad-Line Regions in Blazars, The Astrophysical Journal, 653, 1089

Lovell, J. E. J., Jauncey, D. L., Reynolds, J. E., et al. 1998, The Time Delay in the Gravitational Lens PKS 1830–211, The Astrophysical Journal, 508, L51

Lovell, J. E. J., Reynolds, J. E., Jauncey, D. L., et al. 1996, PKS 1830-211: A Possible Compound Gravitational Lens, The Astrophysical Journal Letter, 472, L5

Lyubarsky, Y. 2009, Asymptotic structure of Poynting-Dominated Jets, The Astrophysical Journal, 698, 1570

MAGIC Collaboration, Acciari, V. A., Ansoldi, S., et al. 2018, Detection of persistent VHE gamma-ray emission from PKS 1510-089 by the MAGIC telescopes during low states between 2012 and 2017, A&A, 619, A159

MAGIC Collaboration, Acciari, V. A., Ansoldi, S., et al. 2019, A fast, very-high-energy γ-ray flare from BL Lacertae during a period of multi-wavelength activity in June 2015, A&A, 623, A175

Malkov, M. A., & Drury, L. O. 2001, Nonlinear theory of diffusive acceleration of particles by shock waves, Reports on Progress in Physics, 64, 429

Manchanda, R. K. 2010, in Astronomical Society of India Conference Series, Vol. 1, Astronomical Society of India Conference Series, 177–191

Maraschi, L., & Tavecchio, F. 2003, The Jet-Disk Connection and Blazar Unification, ApJ, 593, 667

Marscher, A. P., & Gear, W. K. 1985, Models for high-frequency radio outbursts in extragalactic sources, with application to the early 1983 millimeter-to-infrared flare of 3C 273, Astrophysical Journal, Part 1 (ISSN 0004-637X), vol. 298, Nov. 1, 1985, p. 114-127., 298, 114

Marscher, A. P., Jorstad, S. G., D'Arcangelo, F. D., Smith, P. S., et al. 2008, The inner jet of an active galactic nucleus as revealed by a radio-to-γ-ray outburst, Nature, 452, 966

Matthews, J. H., Bell, A. R., & Blundell, K. M. 2020, Particle acceleration in astrophysical jets, New Astronomy Reviews, 89, 101543

Matthiae, G. 2019, Knee, ankle and GZK in historical perspective, Nuclear and Particle Physics Proceedings, 306-308, 98, cRIS 2018 "Entering the Era of Multi-Messenger Astronomy"

Max-Moerbeck, W., Richards, J. L., Hovatta, T., et al. 2014, A method for the estimation of the significance of cross-correlations in unevenly sampled red-noise time series, Monthly Notices of the Royal Astronomical Society, 445, 437

Max-Moerbeck, W., Richards, J. L., Hovatta, T., et al. 2014, A method for the estimation of the significance of cross-correlations in unevenly sampled red-noise time series, Monthly Notices of the Royal Astronomical Society, 445, 437

McKee, M. 2013, Cosmic rays originate from supernova shockwaves, Nature, doi:10.1038/nature.2013.12436

Melrose, D. B., & Rafat, M. Z. 2017, Pulsar radio emission mechanism: Why no consensus?, Journal of Physics: Conference Series, 932, 012011

Mertsch, P., & Sarkar, S. 2011, Fermi Gamma-Ray "Bubbles" from Stochastic Acceleration of Electrons, Phys. Rev. Lett., 107, 091101

Meyer, E. T., Georganopoulos, M., Sparks, W. B., et al. 2015, Ruling out IC/CMB X-rays in PKS 0637-752 and the Implications for TeV Emission from Large-scale Quasar Jets, The Astrophysical Journal, 805, 154

Meyer, M., Petropoulou, M., & Christie, I. M. 2021, The Observability of Plasmoid-powered γ-Ray Flares with the Fermi Large Area Telescope, The Astrophysical Journal, 912, 40

Meyer, M., Scargle, J. D., & Blandford, R. D. 2019, Characterizing the Gamma-Ray Variability of the Brightest Flat Spectrum Radio Quasars Observed with the Fermi LAT, ApJ, 877, 39

Middleton, M. J., Walton, D. J., Alston, W., et al. 2021, NuSTAR reveals the hidden nature of SS433, Monthly Notices of the Royal Astronomical Society, 506, 1045

Miller, J. S., French, H. B., & Hawley, S. A. 1978, The spectrum and magnitude of the galaxy associated with BL Lacertae., The Astrophysical Journal Letter, 219, L85

Millikan, R. A. 1925, High Frequency Rays of Cosmic Origin, Science, 62, 445

Mo, G., Jayaraman, R., Frostig, D., et al. 2024, Multi-messenger astrophysics in the gravitational-wave era, PoS, TAUP2023, 105

Morris, P. J., Potter, W. J., & Cotter, G. 2019, The feasibility of magnetic reconnection powered blazar flares from synchrotron self-Compton emission, Monthly Notices of the Royal Astronomical Society, 486, 1548

Morrison, P. 1957, On the Origins of Cosmic Rays, Rev. Mod. Phys., 29, 235

Morrison, P. 1958, On gamma-ray astronomy, Il Nuovo Cimento (1955-1965), 7, 858

Muller, S., Jaswanth, S., Horellou, C., & Martí-Vidal, I. 2020, All good things come in threes: the third image of the lensed quasar PKS 1830-211, A&A, 641, L2

Nair, S., Narasimha, D., & Rao, A. P. 1993, PKS 1830-211 as a Gravitationally Lensed System, The Astrophysical Journal, 407, 46

Nakagawa, K., & Mori, M. 2013, Time Series Analysis of Gamma-Ray Blazars and Implications for the Central Black-hole Mass, The Astrophysical Journal, 773, 177

Nalewajko, K., Begelman, M. C., Cerutti, B., Uzdensky, D. A., & Sikora, M. 2012, Energetic constraints on a rapid gamma-ray flare in PKS 1222+216, Monthly Notices of the Royal Astronomical Society, 425, 2519

Narayan, R., & Piran, T. 2012a, Variability in blazars: clues from PKS 2155304, Monthly Notices of the Royal Astronomical Society, 420, 604

Narayan, R., & Piran, T. 2012b, Variability in blazars: clues from PKS 2155304, Monthly Notices of the Royal Astronomical Society, 420, 604

NASA E/PO, S. S. U. S. 2014, Swift satellite image

Neronov, A., Savchenko, D., & Semikoz, D. V. 2024, Neutrino Signal from a Population of Seyfert Galaxies, Phys. Rev. Lett., 132, 101002

Nikolić, S., van de Ven, G., Heng, K., et al. 2013, An Integral View of Fast Shocks Around Supernova 1006, Science, 340, 45

Nilsson, K., Lindfors, E., Takalo, L. O., et al. 2018, Long-term optical monitoring of TeV emitting blazars. I. Data analysis, A&A, 620, A185

Oke, J. B., & Gunn, J. E. 1974, The Distance of BL Lacertae, The Astrophysical Journal Letter, 189, L5

Padovani, P. 2024, in 7th Heidelberg International Symposium on High-Energy Gamma-Ray Astronomy, 1

Padovani, P., Alexander, D. M., Assef, R. J., et al. 2017, Active galactic nuclei: what's in a name?, The Astronomy and Astrophysics Review, 25, 2

Padovani, P., Bonzini, M., Kellermann, K. I., et al. 2015, Radio-faint AGN: a tale of two populations, Monthly Notices of the Royal Astronomical Society, 452, 1263

Pandey, A., & Stalin, C. S. 2022, Detection of minute-timescale γ-ray variability in BL Lacertae by Fermi-LAT, A&A, 668, A152

Papadakis, I. E., & Lawrence, A. 1993, Improved Methods for Power Spectrum Modelling of Red Noise, Monthly Notices of the Royal Astronomical Society, 261, 612

Pedregosa, F., Varoquaux, G., Gramfort, A., et al. 2011, Scikit-learn: Machine Learning in Python, Journal of Machine Learning Research, 12, 2825

Peterson, B. 2006, The Broad-Line Region in Active Galactic Nuclei, ed. D. Alloin, R. Johnson, & P. Lira (Berlin, Heidelberg: Springer Berlin Heidelberg), 77–100

Petropoulou, M., & Mastichiadis, A. 2012, On proton synchrotron blazar models: the case of quasar 3C 279, Monthly Notices of the Royal Astronomical Society, 426, 462

Poole, T. S., Breeveld, A. A., Page, M. J., et al. 2008, Photometric calibration of the Swift ultraviolet/optical telescope, Monthly Notices of the Royal Astronomical Society, 383, 627

Poutanen, J., & Stern, B. 2010, GeV Breaks in Blazars as a Result of Gamma-ray Absorption Within the Broad-line Region, The Astrophysical Journal Letter, 717, L118

Poutanen, J., Zdziarski, A. A., & Ibragimov, A. 2008, Superorbital variability of X-ray and radio emission of Cyg X-1 – II. Dependence of the orbital modulation and spectral hardness on the superorbital phase, Monthly Notices of the Royal Astronomical Society, 389, 1427

Prince, R. 2021, Broad-band study of BL Lac during flare of 2020: spectral evolution and emergence of HBL component, MNRAS, 507, 5602

Raiteri, C. M., Villata, M., D'Ammando, F., et al. 2013, The awakening of BL

Lacertae: observations by Fermi, Swift and the GASP-WEBT, Monthly Notices of the Royal Astronomical Society, 436, 1530

Rasmussen, C. E. 2004, in Lecture Notes in Computer Science, Vol. 3176, Advanced Lectures on Machine Learning, ed. O. Bousquet, U. von Luxburg, & G. Rätsch (Berlin, Heidelberg: Springer)

Readhead, A. C. S. 1994, Equipartition Brightness Temperature and the Inverse Compton Catastrophe, The Astrophysical Journal, 426, 51

Refsdal, S. 1964, On the possibility of determining Hubble's parameter and the masses of galaxies from the gravitational lens effect, Monthly Notices of the Royal Astronomical Society, 128, 307

Reimer, A. 2012, On the Physics of Hadronic Blazar Emission Models, Journal of Physics: Conference Series, 355, 012011

Rieger, F. 2019, Gamma-Ray Astrophysics in the Time Domain, Galaxies, 7, 28

Rieger, F. M., & Duffy, P. 2004, Shear Acceleration in Relativistic Astrophysical Jets, The Astrophysical Journal, 617, 155

Rodríguez-Pascual, P. M., Alloin, D., Clavel, J., et al. 1997, Steps toward Determination of the Size and Structure of the Broad-Line Region in Active Galactic Nuclei. IX. Ultraviolet Observations of Fairall 9, The Astrophysical Journal Supplement, 110, 9

Romano, P., Campana, S., Chincarini, G., et al. 2006, Panchromatic study of GRB 060124: from precursor to afterglow, A&A, 456, 917

Roming, P. W. A., Kennedy, T. E., Mason, K. O., et al. 2005, The Swift Ultra-Violet/Optical Telescope, Space Sci. Rev., 120, 95

Roming, P. W. A., Koch, T. S., Oates, S. R., et al. 2008, The first Swift Ultraviolet/Optical telescope GRB Afterglow Catalog, The Astrophysical Journal, 690, 163

Romoli, C., Chakraborty, N., Dorner, D., Taylor, A. M., & Blank, M. 2018, Flux Distribution of Gamma-Ray Emission in Blazars: The Example of Mrk 501, Galaxies, 6, 135

Ruiz, J. R., Crenshaw, D. M., Kraemer, S. B., et al. 2005, Probing the Kinematics of the Narrow-Line Region in Seyfert Galaxies with Slitless Spectroscopy: Observational Results, AJ, 129, 73

Rulten, C. 2022, Radio Galaxies at TeV Energies, Galaxies, 10, 61

Rybicki, G. B., & Lightman, A. P. 1979, Radiative processes in astrophysics

Sahakyan, N., & Giommi, P. 2022, A 13-yr-long broad-band view of BL Lac, MNRAS, 513, 4645

Sanchez, D., Giebels, B., Fortin, P., et al. 2015, From radio to TeV: the surprising spectral energy distribution of AP Librae, Monthly Notices of the Royal Astronomical Society, 454, 3229

Sbarrato, T., Ghisellini, G., Maraschi, L., & Colpi, M. 2012, The relation between broad lines and -ray luminosities in Fermi blazars, Monthly Notices of the Royal Astronomical Society, 421, 1764

Scargle, J. D. 2020, Studies in Astronomical Time-series Analysis. VII. An Enquiry Concerning Nonlinearity, the rms-Mean Flux Relation, and Lognormal Flux Distributions, The Astrophysical Journal, 895, 90

Scargle, J. D., Norris, J. P., Jackson, B., & Chiang, J. 2013, Studies in astronomical time series analysis. VI. Bayesian Block Representations, The Astrophysical Journal, 764, 167

Schechter, P. L., Bailyn, C. D., Barr, R., et al. 1997, The Quadruple Gravitational Lens PG 1115+080: Time Delays and Models, The Astrophysical Journal Letter, 475, L85

Schlafly, E. F., & Finkbeiner, D. P. 2011, Measuring Reddening with Sloan Digital Sky Survey Stellar Spectra and Recalibrating SFD, The Astrophysical Journal, 737, 103

Scully, S. T., Malkan, M. A., & Stecker, F. W. 2014, An Empirical Determination of the Intergalactic Background Light Using Near-infrared Deep Galaxy Survey Data out to 5 μm and the Gamma-Ray Opacity of the Universe, The Astrophysical Journal, 784, 138

Shukla, A., & Mannheim, K. 2020a, Gamma-ray flares from relativistic magnetic reconnection in the jet of the quasar 3C 279, Nature Communications, 11, 4176

Shukla, A., & Mannheim, K. 2020b, Gamma-ray flares from relativistic magnetic reconnection in the jet of the quasar 3C 279, Nature Communications, 11, 4176

Shukla, A., Mannheim, K., Patel, S. R., et al. 2018, Short-timescale -Ray Variability in CTA 102, The Astrophysical Journal Letters, 854, L26

Sikora, M., Begelman, M. C., & Rees, M. J. 1994, Comptonization of Diffuse Ambient Radiation by a Relativistic Jet: The Source of Gamma Rays from Blazars?, The Astrophysical Journal, 421, 153

Sironi, L., Petropoulou, M., & Giannios, D. 2015, Relativistic jets shine through shocks or magnetic reconnection?, Monthly Notices of the Royal Astronomical Society, 450, 183

Smith, D., Hooper, D., & Vieregg, A. 2021, Revisiting AGN as the source of IceCube's diffuse neutrino flux, Journal of Cosmology and Astroparticle Physics, 2021, 031

Smith, D. A., Abdollahi, S., Ajello, M., et al. 2023, The Third Fermi Large Area Telescope Catalog of Gamma-Ray Pulsars, The Astrophysical Journal, 958, 191

Snowden, S. L., Egger, R., Freyberg, M. J., et al. 1997, ROSAT Survey Diffuse X-Ray Background Maps. II., The Astrophysical Journal, 485, 125

Sobolewska, M. A., Siemiginowska, A., Kelly, B. C., & Nalewajko, K. 2014, Stochastic Modeling of the Fermi/LAT γ-Ray Blazar Variability, The Astrophysical Journal, 786, 143

Sol, H., Zech, A., Boisson, C., et al. 2013, Active Galactic Nuclei under the scrutiny of CTA, Astroparticle Physics, 43, 215

Spada, M., Ghisellini, G., Lazzati, D., & Celotti, A. 2001, Internal shocks in the jets of radio-loud quasars, Monthly Notices of the Royal Astronomical Society, 325, 1559

Spada, M., Ghisellini, G., Lazzati, D., & Celotti, A. 2001, Internal shocks in the jets of radio-loud quasars, Monthly Notices of the Royal Astronomical Society, 325, 1559

Stecker, F. W., Malkan, M. A., & Scully, S. T. 2006, Intergalactic Photon Spectra from the Far-IR to the UV Lyman Limit for $0 < z < 6$ and the Optical Depth of the Universe to High-Energy Gamma Rays, The Astrophysical Journal, 648, 774

Stern, B. E., & Poutanen, J. 2014, The Mystery of Spectral Breaks: Lyman Continuum Absorption by Photon-Photon Pair Production in the Fermi GeV Spectra of Bright Blazars, The Astrophysical Journal, 794, 8

Strigari, L. E. 2013, Galactic searches for dark matter, Physics Reports, 531, 1, galactic searches for dark matter

Sturani, R. 2013, LIGO/Virgo/GEO/KAGRA Science, ASP Conf. Ser., 467, 59

Su, M., Slatyer, T. R., & Finkbeiner, D. P. 2010, Giant Gamma-Ray Bubbles from Fermi-LAT: Active Galactic Nucleus Activity or Bipolar Galactic Wind?, The Astrophysical Journal, 724, 1044

Subrahmanyan, R., Narasimha, D., Pramesh Rao, A., & Swarup, G. 1990, 1830-211 / gravitationally lensed images of a flat-spectrum radio core ?, Monthly Notices of the Royal Astronomical Society, 246, 263

Taboada, I., & Stein, R. 2019, IceCube-190730A an astrophysical neutrino candidate in spatial coincidence with FSRQ PKS 1502+106, The Astronomer's Telegram, 12967, 1

Takata, J. 2016, Gamma Ray Pulsars: From Radio to Gamma Rays, ed. A. W. Alsabti & P. Murdin (Cham: Springer International Publishing), 1–29

Tammi, J., & Duffy, P. 2009, Particle-acceleration time-scales in TeV blazar flares, Monthly Notices of the Royal Astronomical Society, 393, 1063

Tanaka, Y. T., Stawarz, Ł., Thompson, D. J., et al. 2011, Fermi Large Area Telescope Detection of Bright γ-Ray Outbursts from the Peculiar Quasar 4C +21.35, The Astrophysical Journal, 733, 19

Tavecchio, F., Becerra-Gonzalez, J., Ghisellini, G., et al. 2011, On the origin of the γ-ray emission from the flaring blazar PKS 1222+216, A&A, 534, A86

Tavecchio, F., & Ghisellini, G. 2012, “Flat” broad line region and gamma-ray absorption in blazars, arXiv e-prints, arXiv:1209.2291

Tavecchio, F., Maraschi, L., Wolter, A., et al. 2007, Chandra and Hubble Space Telescope Observations of Gamma-Ray Blazars: Comparing Jet Emission at Small and Large Scales, The Astrophysical Journal, 662, 900

Tchekhovskoy, A., McKinney, J. C., & Narayan, R. 2009, Efficiency of magnetic to Kinetic Energy Conversion in a monopole magnetosphere, The Astrophysical Journal, 699, 1789

Timmer, J., & König, M. 1995, On generating power law noise., A&A, 300, 707

Urry, C. M., & Padovani, P. 1995, Unified Schemes for Radio-Loud Active Galactic Nuclei, PASP, 107, 803

Usov, V. V., & Melrose, D. B. 1995, Pulsars with strong magnetic fields : polar gaps, bound pair creation and nonthermal luminosities., Australian Journal of Physics, 48, 571

Uttley, P., McHardy, I. M., & Papadakis, I. E. 2002, Measuring the broad-band power spectra of active galactic nuclei with RXTE, Monthly Notices of the Royal Astronomical Society, 332, 231

Uttley, P., McHardy, I. M., & Vaughan, S. 2005, Non-linear X-ray variability in X-ray binaries and active galaxies, Monthly Notices of the Royal Astronomical Society, 359, 345

Vaughan, S. 2005, A simple test for periodic signals in red noise, A&A, 431, 391

Vaughan, S., Edelson, R., Warwick, R. S., & Uttley, P. 2003, On characterizing the variability properties of X-ray light curves from active galaxies, Monthly Notices of the Royal Astronomical Society, 345, 1271

Verrecchia, F., Pittori, C., Piano, G., et al. 2022, AGILE detection of increasing gamma-ray activity of blazar PKS 1424-418, The Astronomer's Telegram, 15818, 1

Vieira, N., Ruan, J. J., Haggard, D., et al. 2020, A Deep CFHT Optical Search for a Counterpart to the Possible Neutron Star–Black Hole Merger GW190814, The Astrophysical Journal, 895, 96

Wagner, S. M., Burd, P., Dorner, D., et al. 2021, Statistical properties of flux variations in blazar light curves at GeV and TeV energies, PoS, ICRC2021, 868

Wang, F., Yang, J., Fan, X., et al. 2021, A Luminous Quasar at Redshift 7.642, The Astrophysical Journal Letters, 907, L1

Wang, J.-C. 2002, Stochastic Particle Acceleration in Blazar Jets, Chinese J. Astron. Astrophys., 2, 1

Watson, A. M., Butler, N. R., Lee, W. H., et al. 2020, Limits on the electromagnetic counterpart to S190814bv, Monthly Notices of the Royal Astronomical Society, 492, 5916

Weaver, Z. R., Williamson, K. E., Jorstad, S. G., et al. 2020, Multiwavelength Variability of BL Lacertae Measured with High Time Resolution, The Astrophysical Journal, 900, 137

Wiklind, T., & Combes, F. 1996, The redshift of the gravitational lens of PKS1830–211 determined from molecular absorption lines, Nature, 379, 139

Wiklind, T., & Combes, F. 2001, in Astronomical Society of the Pacific Conference Series, Vol. 237, Gravitational Lensing: Recent Progress and Future Go, ed. T. G. Brainerd & C. S. Kochanek, 155

Winn, J. N., Kochanek, C. S., McLeod, B. A., et al. 2002, PKS 1830-211: A Face-on Spiral Galaxy Lens, The Astrophysical Journal, 575, 103

Wood, M., Caputo, R., Charles, E., et al. 2017, Fermipy: An open-source Python package for analysis of Fermi-LAT Data, PoS, ICRC2017, 824

Yan, D., Zeng, H., & Zhang, L. 2012, Non-variable TeV emission from the extended jet of a blazar in the stochastic acceleration scenario: the case of the hard TeV emission of 1ES 1101–232, Monthly Notices of the Royal Astronomical Society, 424, 2173

Yang, H.-Y. K., Ruszkowski, M., Ricker, P. M., Zweibel, E., & Lee, D. 2012, The Fermi Bubbles: Supersonic Active Galactic Nucleus Jets with anisotropic cosmic-ray diffusion, The Astrophysical Journal, 761, 185

Zacharias, M., & Wagner, S. J. 2016, The extended jet of AP Librae: Origin of the very high-energy γ-ray emission?, Astronomy & Astrophysics, 588, A110

Zatsepin, G. T., & Kuz'min, V. A. 1966, Upper Limit of the Spectrum of Cosmic Rays, Soviet Journal of Experimental and Theoretical Physics Letters, 4, 78

Zhang, S., Chen, Y.-p., Collmar, W., et al. 2008, High-Energy Properties of PKS 1830-211, The Astrophysical Journal, 683, 400

Zubovas, K., King, A. R., & Nayakshin, S. 2011, The Milky Way's Fermi bubbles: echoes of the last quasar outburst?, Monthly Notices of the Royal Astronomical Society: Letters, 415, L21

Zwicky, F. 1937, On the Masses of Nebulae and of Clusters of Nebulae, The Astrophysical Journal, 86, 217